Novel concepts in near-field optics: from magnetic near-field to optical forces

by

Honghua Yang

B.S., Sichuan University, 2009

M.S., University of Colorado, 2011

A thesis submitted to the

Faculty of the Graduate School of the

University of Colorado in partial fulfillment

of the requirements for the degree of

Doctor of Philosophy

Department of Physics

2015

This thesis entitled:
Novel concepts in near-field optics:
from magnetic near-field to optical forces
written by Honghua Yang
has been approved for the Department of Physics

Markus B. Raschke

Andreas Becker

Date

The final copy of this thesis has been examined by the signatories, and we find that both the content and the form meet acceptable presentation standards of scholarly work in the above mentioned discipline.

Yang, Honghua (Ph.D., Physics)

Novel concepts in near-field optics:

from magnetic near-field to optical forces

Thesis directed by Prof. Markus B. Raschke

Driven by the progress in nanotechnology, imaging and spectroscopy tools with nanometer spatial resolution are needed for *in situ* material characterizations. Near-field optics provides a unique way to selectively excite and detect elementary electronic and vibrational interactions at the nanometer scale, through interactions of light with matter in the near-field region. This dissertation discusses the development and applications of near-field optical imaging techniques, including plasmonic material characterization, optical spectral nano-imaging and magnetic field detection using *scattering*-type scanning near-field optical microscopy (*s*-SNOM), and exploring new modalities of optical spectroscopy based on optical gradient force detection.

Firstly, the optical dielectric functions of one of the most common plasmonic materials – silver is measured with ellipsometry, and analyzed with the Drude model over a broad spectral range from visible to mid-infrared. This work was motivated by the conflicting results of previous measurements, and the need for accurate values for a wide range of applications of silver in plasmonics, optical antennas, and metamaterials. This measurement provides a reference for dielectric functions of silver used in metamaterials, plasmonics, and nanophotonics.

Secondly, I implemented an infrared *s*-SNOM instrument for spectroscopic nano-imaging at both room temperature and low temperature. As one of the first cryogenic *s*-SNOM instruments, the novel design concept and key specifications are discussed. Initial low-temperature and high-temperature performances of the instrument are examined by imaging of optical conductivity of vanadium oxides (VO_2 and V_2O_3) across their phase transitions. The spectroscopic imaging capability is demonstrated on chemical vibrational resonances of Poly(methyl methacrylate) (PMMA) and other samples.

The third part of this dissertation explores imaging of optical magnetic fields. As a proof-of-principle, the magnetic near-field response of a linear rod antenna is studied with Babinet's principle. Babinet's principle connects the magnetic field of a structure to the electric field of its complement structure. Using combined far- and near-field spectroscopy, imaging, and theory, I identify magnetic dipole and higher order bright and dark magnetic resonances at mid-infrared frequencies. From resonant length scaling and spatial field distributions, I confirm that the theoretical requirement of Babinet's principle for a structure to be infinitely thin and perfectly conducting is still fulfilled to a good approximation in the mid-infrared. Thus Babinet's principle provides access to spatial and spectral magnetic field properties, leading to targeted design and control of magnetic optical antennas.

Lastly, a novel form of nanoscale optical spectroscopy based on mechanical detection of optical gradient force is explored. It is to measure the optical gradient force between induced dipole moments of a sample and an atomic force microscope (AFM) tip. My study provides the theoretical basis in terms of spectral behavior, resonant enhancement, and distance dependence of the optical gradient force from numerical simulations for a coupled nanoparticle model geometry. I show that the optical gradient force is dispersive for local electronic and vibrational resonances, yet can be absorptive for collective polaronic excitations. This spectral behavior together with the distance dependence scaling provides the key characteristics for its measurement and distinction from competing processes such as thermal expansion. Furthermore, I provide a perspective for resonant enhancement and control of optical forces in general.

Dedication

To Anqi and my family.

Acknowledgements

I would not be here today without the support of many people. First I am most indebted to my advisor, Markus Raschke. His extensive knowledge and experience, his passion and creativity towards physics have tremendously benefited me over the years. His support during my working at Anasys is crucial to the accomplishment of my PhD work.

I also want to thank all members of the Raschke group: Rob Olmon, Sam Berweger, Andrew Jones, Joanna Atkin, Erik Hebestreit, Brian O'Callahan, Ben Pollard, Vasily Kravtsov, Eric Muller, Kyoung-Duck Park, Sven Dönges, Omar Khatib, Ronald Ulbricht, Will Lewis, Paul Sass, Xiaoji Xu, Ryan Murdick, Erik Josberger, Ian Craig, Sibel Yalcin, Justin Gerber, Molly May, Evan Anderson, Jonas Allerbeck, and many others. I have been enjoying working with them and sharing insightful ideas on physics.

I am grateful to Prof. Carsten Rockstuhl for the helps during my summer visit in Jena, when I learnt skills and tools of numerical simulations. I also thank many other collaborators I have worked with.

I would further express my appreciation to Prof. Andreas Becker for being in my committee and for his valuable feedbacks for my thesis.

Finally, I want to thank Craig Prater, Kevin Kjoller, Doug Gotthard, Roshan Shetty, and all my colleagues at Anasys. Without their support and encouragement I would not have made it through the PhD.

Contents

Chapter

Tables

Table

Figures

Figure

Chapter 1

Introduction

Nanotechnology has enabled new materials and devices through advanced bottom-up nanomaterial synthesis to top-down nano fabrication. The properties of these new materials and devices are characterized at the relevant length scales of nm to μm, determined by composition, structure, and chemical interactions. On the one hand the structural informations such as spatial inhomogeneities, atomic scale defects, and grain boundaries are typically provided by scanning probe microscopy and electron microscopies. On the other hand, electronic and chemical properties are typically probed by optical spectroscopies with ensemble average at the bulk level limited by diffraction. To effectively access the local electronic and vibrational responses and their couplings in various materials, a more generalized approach with combined spectroscopic specificity and nanometer spatial resolution is needed.

As the energy of light quanta matches the energy of electronic and vibrational excitations in matter, optical techniques provide an effective tool to probe these excitations. Optical techniques are adaptable in ambient environment for *in situ* studies, and are generally non-destructive. Optical methods based on the light-matter interaction are also less sensitive to perturbations by external electric and magnetic fields. In addition, by using ultrafast lasers, optical techniques provide a unique way to probe at the characteristic time scales of electronic and vibrational excitations on the order of fs to ps. However, due to diffraction traditional optical spectroscopy/microscopy has limited spatial resolution on the order of a few hundred nm in visible to a few μm in infrared. This diffraction limit was identified by Ernst Abbe in 1873 [1]. He found that a light beam focused by a

lens with a converging half-angle θ would result in concentric bright and dark rings with a central sphere of radius

$$r = \frac{1.22\lambda}{2n\sin(\theta)} = \frac{0.61\lambda}{\mathrm{NA}}, \tag{1.1}$$

with refractive index of the medium n, free space wavelength λ, and the numerical aperture (NA), $\mathrm{NA} = n\sin(\theta)$. The focal spot is known as Airy disk with a radial intensity profile of a first order Bessel function.

The criterion to distinguish two adjacent points, now known as the Rayleigh criterion, states that two points are barely resolved if the maximum of the Airy disk of the first point coincides with the first minimum of the Airy disk of the second point. Thus even using an oil immersion objective with $n \approx 1.3$, diffraction still practically limits the optical resolution to ~ 200 nm at visible wavelengths. Higher spatial resolution can be achieved by using ultraviolet (UV) or X-ray light. However, the lack of suitable focusing lenses, strong absorption in air, and sample damage due to photon ionization limit the practical use of this strategy. Alternatively, electron microscopy can be constructed by focusing electrons with a magnetic lens in order to achieve even sub-atomic resolution due to the small de Broglie wavelength of electrons. Despite being an indispensable tool for nanostructure analysis, electron microscopes generally lack the capability to probe vibrational resonances of materials. In addition, electron microscopes require high vacuum to operate.

Another class of techniques, called super-resolution fluorescence microscopy, has been developed to overcome the diffraction limit based on fluorescence imaging. Due to its success in biological imaging, the technique was awarded the Nobel Prize in Chemistry in 2014 [169]. Super-resolution fluorescence microscopy consists of two primary methods: stimulated emission depletion microscopy (STED) [122] based on nonlinear saturation, and photo-activated light microscopy (PALM) [22] based on point-spread function reconstruction of an emitter by turning the fluorescence of individual molecules on and off. These methods have been demonstrated to achieve 10 nm resolution in three dimensions, however, they have been limited to luminescence. Therefore, a more universal method is desired to extend the diverse range of optical techniques by overcoming the diffraction

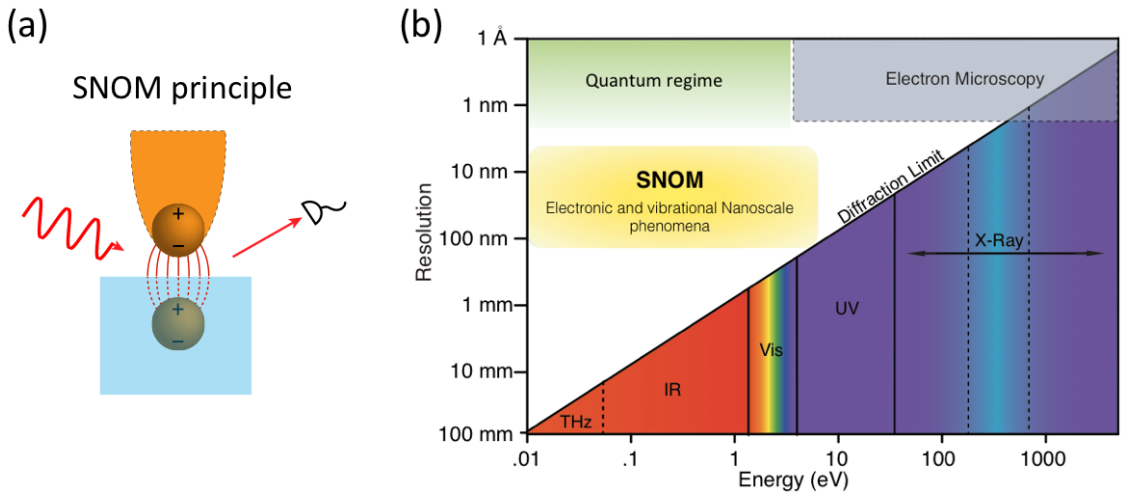

Figure 1.1: (a) Principle of scanning near-field optical microscopy (SNOM): the incident light induces a coupled polarization between the tip and sample, which then scatters light to the detector in the far-field. The localized light-matter interaction under the tip provides the high spatial resolution. (b) The spatial resolution of SNOM can reach 10 nm with spectral coverage from visible to THz. Thus SNOM enables the study of electronic and vibrational phenomena at the nanoscale. Figure after [20].

limit.

Near-field optics can overcome the diffraction limit through the spatial confinement of the evanescent field, and is generally compatible with all conventional optical techniques, including nonlinear and ultrafast techniques, ranging in spectral region from UV to THz. The experimental implementation of near-field optical imaging based on a scanning probe microscope is named scanning near-field optical microscopy (SNOM). Its principle is based on the localized mutual polarization of the tip and sample, which then scatters light to the detector in the far-field (Fig. 1.1a). As a consequence, SNOM makes it possible to extend all-optical spectroscopy to a spatial resolution down to tens of nm, practically limited by the tip radius [231, 195]. The spatial resolution and spectral accessibility of SNOM are illustrated in Fig. 1.1b.

This thesis explores different mechanisms responsible for light-matter interaction at the nanoscale, and their implications and potential applications for optical imaging and spectroscopy. The remainder of the chapter provides a conceptual background for the thesis.

1.1 Near-field optics and near-field optical microscopy

Near-field optics relies on the spatial confinement of evanescent waves, whose amplitude decays exponentially from the sources (such as currents or induced polarizations). Evanescent waves can be expanded in the form of $E_0 e^{i(\mathbf{k}\cdot\mathbf{r}-\omega t)}$, with at least one component of the wavevector $\mathbf{k}$ being imaginary. The highly confined evanescent waves are crucial for subwavelength spatial resolution and other novel properties in near-field optics.

The idea of near-field optical microscopy dates back to 1928. In a letter from E.H. Synge to Einstein [172, 173], he proposed to use light scattered from a tiny gold particle to illuminate the sample locally. By raster scanning the particle over a sample surface while recording the local emitted signal simultaneously, one could in principle obtain an optical image of the sample. The same idea for super resolution was reinvented several times, but the first experimental demonstration was not achieved until 1972 [12]. By using microwaves, Ash *et al.* were able to achieve a resolution of $\lambda/60$. The first experiment at optical frequencies was performed a year after the invention of scanning tunneling microscopy (STM), which enabled the stable position control of a local light source relative to the sample surface. Pohl *et al.* obtained a resolution of 25 nm at laser wavelength $\lambda = 488$ nm by squeezing light through a small aperture [189]. This technique later evolved into near-field scanning optical microscopy (NSOM), now typically implemented by using a subwavelength aperture at the end of a tapered fiber probe. However, NSOM is severely limited by the dispersion of the fiber, the complex contrast mechanism, and weak signal due to low throughput put from the small aperture. These drawbacks limit its generalization for spectroscopy.

To overcome the limitations of NSOM, a proposal was made to use a sharp tip to perturb in the near-field region and scatter the field into a propagating wave for far-field detection [230, 105, 211]. This technique, based on detecting the scattered light from perturbed near-field, is named *scattering*-type scanning near-field optical microscopy (*s*-SNOM). [1]

A typical experimental implementation of *s*-SNOM consists of an atomic force microscope

[1] *s*-SNOM is also called apertureless NSOM (ANSOM). NSOM or SNOM is frequently used interchangeably in literature.

(AFM), a light source, a detector, and focusing and collecting optics. Light is focused onto the AFM tip and the back-scattered light is collected. The principle of *s*-SNOM relies on the optical field localization at the nanoscale tip apex and its optical antenna properties. The tip (generally 5 - 30 nm radius of curvature) acts as a localized scattering source for the enhanced evanescent optical fields localized between the AFM tip and the sample surface. The scattered light from the tip-apex region then contains spectroscopic information about the sample from a region confined laterally by the dimensions of the tip apex radius. Scattered light is collected in the far-field, and both amplitude and phase can be detected interferometrically.

s-SNOM has been successfully used to map local dielectric contrast, and also the local electromagnetic field in nano-photonoic and plasmonic structures. The recent progress in *s*-SNOM, especially its advance in nanoscale infrared spectroscopy, has attracted significant interest for commercializing this technique.

1.2 Dissertation Outline

This thesis is organized as follows:

Chapter 2 provides a theoretical background of the optical properties of materials, particular the Drude free electron behavior of metals and the associated plasmonic responses. In addition, the principle of near-field light-matter interaction in *s*-SNOM is discussed.

Chapter 3 studies the dielectric function of two most widely used materials in plasmonics – silver and gold. This work was motivated by the need for accurate values for the wide range of applications of silver and gold for plasmonics, optical antenna, and metamaterials. Using broadband spectroscopic ellipsometry, we determine the complex valued dielectric function of evaporated and template stripped polycrystalline silver films from 0.05 eV ($\lambda = 25$ μm) to 4.14 eV ($\lambda = 300$ nm). Our Drude model analysis on silver provides a relaxation time of 17$\pm$3 fs, a significant correction to the commonly used relaxation time of 31$\pm$12 fs from Johnson and Christy (Phys. Rev. B 6, 4370 (1972)). Yet, it is in agreement with the suggestion that the Johnson and Christy value has been a large overestimate based from a large body of plasmonics work. For energies below the

interband transition, slight deviation from the Drude model is observed in our data and through which we determine a frequency dependence of the relaxation time consistent with predictions from Fermi-liquid theory. In addition, to explain the discrepancies in the previous measurements, we discuss the role of intrinsic electron scattering and extrinsic defect and grain boundary damping. This work has been published as H. Yang, J. Archangel, M. Sundheimer, E. Tucker, G. Boreman, and M.B. Raschke, "Optical dielectric function of silver", Physical Review B 91, 235137 (2015).

The experimental implement of *s*-SNOM is covered in chapters 4 and 5. Chapter 4 describes experimental implementations of an infrared *s*-SNOM instrument and several applications including chemical mapping through molecular vibrational resonances and imaging surface polaritonic waves on 2D materials. In chapter 5 a low temperature *s*-SNOM system is presented. As one of the first low temperature *s*-SNOM instrument, I mainly cover the novel design concept. This work has been published as H. Yang, E. Hebestreit, E. Josberger, and M.B. Raschke, "A cryogenic scattering-type scanning near-field optical microscope", Rev. Sci. Instruments 84, 023701 (2013).

Followed is the application of *s*-SNOM to map the optical magnetic field (chapter 6) and the extension for a novel optical gradient force spectroscopy (chapter 7).

In chapter 6, I exploit the possibility of using Babinet's principle to probe the magnetic field of a structure through the electric field of its complement structure. Generally, the optical magnetic field interaction is much weaker than the electric field interaction, and thus difficult to measure in experiment. This work demonstrates an elegant method to experimentally map the local optical magnetic field as an important step to understand the near-field interactions. The work has been published as H. Yang, R. Olmon, K. Deryckx, X. Xu, H. Bechtel, Y. Xu, B. Lail, and M.B. Raschke, "Accessing the optical magnetic near-field through Babinet's principle", ACS Photonics 1, 894 (2014).

Chapter 7 describes a novel nanoscale spectroscopic imaging method based on optical force detection. Under laser illumination, induced optical polarization would cause a gradient force between an AFM tip and the underneath sample. I provide a generalized description of the optical gradient force between a scanning tip and sample as an imaging contrast mechanism. The optical

gradient forces are numerically calculated with Maxwell's stress tensor. The spectroscopic response of the optical gradient force is found to be dispersive for single particle electronic or vibrational resonances. In contrast collective polariton resonances can give rise to absorptive spectral force profile. The effect is distinct from the accompanying thermal expansion due to optical absorption, which results in absorptive-like resonance spectra in all cases. While the optical gradient force is comparable to thermal noises in a room temperature AFM, the effect should be detectable under cryogenic conditions as demonstrated in cavity opto-mechanics. The work is submitted for publication as H. Yang, and M.B. Raschke, "Resonant optical gradient force for nano-imaging and -spectroscopy".

Chapter 8 gives a brief summary of the works in this thesis.

Chapter 2

Optical properties of materials

This chapter provides a theoretical background to near-field light-matter interaction for nanoscale imaging and spectroscopy. We begin with the optical properties of materials, then derive related near-field and plasmonic properties for this work.

2.1 Maxwell's equations

To study the interaction of light with matter in the near-field, we start with the Maxwell's equations that form the foundation of classical electrodynamics:

$$\nabla \cdot \mathbf{D} = \rho \tag{2.1}$$

$$\nabla \cdot \mathbf{B} = 0 \tag{2.2}$$

$$\nabla \times \mathbf{E} = -\frac{\partial \mathbf{B}}{\partial t} \tag{2.3}$$

$$\nabla \times \mathbf{H} = \mathbf{J} + \frac{\partial \mathbf{D}}{\partial t} \tag{2.4}$$

with ρ the free charge density, and $\mathbf{J}$ the current. The displacement field $\mathbf{D}$ and the magnetic field $\mathbf{H}$ are defined through:

$$\mathbf{D} = \epsilon_0 \mathbf{E} + \mathbf{P} = \epsilon_0 \epsilon_r \mathbf{E} \tag{2.5}$$

$$\mathbf{B} = \mu_0 \mathbf{H} + \mathbf{M} = \mu_0 \mu_r \mathbf{H}, \tag{2.6}$$

where ϵ_0 and μ_0 are the vacuum dielectric permittivity and the magnetic permeability; polarization $\mathbf{P}$ and magnetization $\mathbf{M}$ describe the additional field response due to the presence of the material.

Therefore the relative dielectric permittivity ϵ_r and permeability μ_r characterize the electromagnetic properties of the material. In the optical frequency, the magnetic permeability of ordinary material is very weak, thus $\mu_r \approx 1$.

In general, the dielectric permittivity (the dielectric function) of a medium as a response function to external electric fields is a tensor [59, 130]. It connects the displacement field and the applied electric field through

$$D_i(\mathbf{r}, t) = \int\int \epsilon_{ij}(\mathbf{r}, \mathbf{r}', t, t') E_j(\mathbf{r}', t') dt' d\mathbf{r}'. \tag{2.7}$$

Only within the local response approximation and in a homogeneous medium, Eq. 2.7 simplifies to

$$D_i(\mathbf{r}, t) = \int \epsilon_{ij}(t - t') E_j(\mathbf{r}, t') dt', \tag{2.8}$$

or in the frequency domain

$$D_i(\mathbf{r}, \omega) = \epsilon_{ij}(\omega) E_j(\mathbf{r}, \omega). \tag{2.9}$$

The dielectric function can be expressed by a scalar $\epsilon(\omega) = \epsilon_0 \epsilon_r(\omega)$ for the case of isotropic media, such as amorphous molecular materials, or metals with cubic crystal lattice (gold and silver). This is the case for all materials to be discussed in this thesis.

It is important to note that in general, due to temporal dispersions in a medium $\epsilon_r(\omega)$ is a complex quantity, i.e., $\epsilon_r(\omega) = \epsilon_1(\omega) + i\epsilon_2(\omega)$. The imaginary part $\epsilon_2(\omega)$ reflects the phase difference between polarization $\mathbf{P}$ and incident field $\mathbf{E}$. The real and imaginary part are not independent due to causality. The two parts are connected through Kramers-Kronig relations:

$$\epsilon_1(\omega) = 1 + \frac{2}{\pi} \mathrm{P} \int_0^\infty \frac{\epsilon_2(\omega')}{\omega'^2 - \omega^2} d\omega', \tag{2.10}$$

$$\epsilon_2(\omega) = -\frac{2\omega}{\pi} \mathrm{P} \int_0^\infty \frac{\epsilon_1(\omega') - 1}{\omega'^2 - \omega^2} d\omega'. \tag{2.11}$$

Hereafter to simplify notations, all the dielectric function mentioned is the relative dielectric function $\epsilon_r(\omega)$, and the subscript r in ϵ_r is dropped.

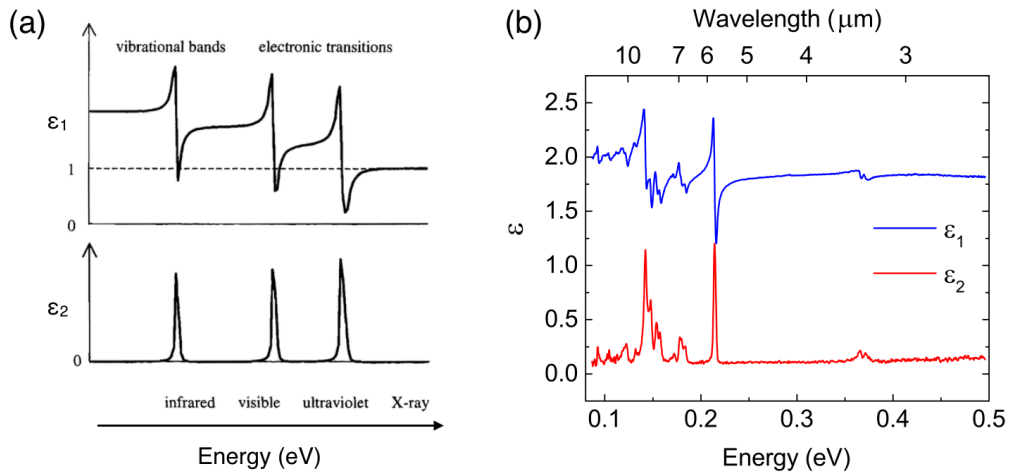

Figure 2.1: (a) The dielectric function of an artificial material from infrared to ultraviolet, featuring resonances due to electronic and vibrational resonances. (b) Dielectric function of PMMA. Figure in (a) after [71].

2.2 Optical properties of materials

Knowledge of the frequency dependent dielectric function gives insight into the underlying elementary excitations of materials, such as lattice vibrations, free carrier absorption, superconducting gaps, plasmon resonances, chemical bonding, excitons, or interband absorption [11, 59, 130]. Dielectric functions of materials are typically determined by ellipsometry, which will be discussed in chapter 3. Fig. 2.1a shows the schematics of a dielectric function characterizing different electronic and vibrational resonances. Across a resonance, $\epsilon_1(\omega)$ shows a dispersive line shape while $\epsilon_2(\omega)$ has an absorptive line shape. The resonances of a dielectric function can be well described by different oscillator models, such as Lorentz oscillators for local vibrational resonances. (b) shows the experimental dielectric function of a polymer (Poly(methyl methacrylate) (PMMA)) featuring different vibrational resonances measured by ellipsometry.

The dielectric function also directly relates to many optical properties, in particular transmission and reflection at the most fundamental level. The complex refractive index $N(\omega) = n(\omega) + i\kappa(\omega)$, characterizing the propagation of light in a medium of interest, relates to the dielectric function through $N(\omega) = \sqrt{\epsilon(\omega)}$, with the refractive index n and the extinction coefficient

κ. It is easy to work out the explicit form of $n(\omega)$ and $\kappa(\omega)$:

$$n = \frac{1}{\sqrt{2}}\left(\epsilon_1 + \sqrt{\epsilon_1^2 + \epsilon_2^2}\right)^{1/2}, \tag{2.12}$$

$$\kappa = \frac{1}{\sqrt{2}}\left(-\epsilon_1 + \sqrt{\epsilon_1^2 + \epsilon_2^2}\right)^{1/2}. \tag{2.13}$$

With a weak absorption $\epsilon_2 \ll \epsilon_1$, the formulae can be simplified to

$$n = \sqrt{\epsilon_1}, \tag{2.14}$$

$$\kappa = \frac{\epsilon_2}{\sqrt{2}n}. \tag{2.15}$$

2.2.1 Lorentz oscillators for molecular resonances

The resonance behaviors of molecular vibrational excitations in Fig. 2.1b can be described by Lorentz oscillators. The displacement of atomic dipoles under an applied electric field follows the equation of motion of

$$m\ddot{x} + m\Gamma\dot{x} + m\omega_0^2 x = -eE(t) \tag{2.16}$$

with the relaxation rate Γ, the electron mass m, and applied electric field $E(t)$. Considering a time harmonic field $E(t) = E(\omega)e^{-i\omega t}$, the displacement $x(t) = x(\omega)e^{-i\omega t}$ can be solved as

$$x(\omega) = \frac{-eE(\omega)/m}{\omega_0^2 - \omega^2 - i\Gamma\omega}. \tag{2.17}$$

The induced polarization from the displacement of atomic dipoles is

$$P(\omega) = -Nex(\omega) \tag{2.18}$$

$$= \frac{Ne^2}{m}\frac{1}{\omega_0^2 - \omega^2 - i\Gamma\omega}E(\omega) \tag{2.19}$$

where N is the electron density. Plugging the polarization $P(\omega)$ back to the expression for the displacement field in Eq. 2.5, we get

$$D(\omega) = \epsilon_0 E(\omega) + P(\omega) \tag{2.20}$$

$$= \epsilon_0 E(\omega) + \frac{Ne^2}{m}\frac{1}{\omega_0^2 - \omega^2 - i\Gamma\omega}E(\omega) \tag{2.21}$$

$$= \epsilon_0\epsilon(\omega)E(\omega). \tag{2.22}$$

Thus the dielectric function across a molecular vibrational resonance at frequency ω_0 can be derived as

$$\epsilon(\omega) = 1 + \frac{Ne^2}{m}\frac{1}{\omega_0^2 - \omega^2 - i\Gamma\omega}. \tag{2.23}$$

2.2.2 Drude model for quasi-free electrons

In the low energy region, the dielectric function of a metal can be described to a good approximation as a gas of noninteracting electrons by the *Drude-Sommerfeld* free electron model (denoted as Drude model below). The model describes the motion of electrons using classic kinetic theory:

$$m^*\ddot{\mathbf{x}} + m^*\Gamma\dot{\mathbf{x}} = -e\mathbf{E}(t) \tag{2.24}$$

where Γ is the relaxation rate, and m^* is the effective mass of electron, which is different from the rest electron mass due to electron correlation effects. It is easy to recognize that the Drude model is a harmonic oscillator without restoring force, or equivalently with the resonance frequency at zero.

The dielectric function can be derived in the same fashion as for the Lorentz oscillators, resulting in an expression of

$$\epsilon(\omega) = 1 - \frac{Ne^2}{m^*\epsilon_0}\frac{1}{\omega^2 + i\omega\Gamma} \tag{2.25}$$

$$\equiv 1 - \frac{\omega_p^2}{\omega^2 + i\omega\Gamma} \tag{2.26}$$

where the plasmon frequency ω_p is related to the effective mass of the electron m^* and the electron density N through

$$\omega_p^2 = \frac{Ne^2}{m^*\epsilon_0}. \tag{2.27}$$

The relaxation rate Γ describes the effective electron scattering rate, with a corresponding relaxation time $\tau = 1/\Gamma$.

To account for the net contribution from the positive ion cores, an effective parameter ϵ_∞ is introduced

$$\epsilon(\omega) = \epsilon_\infty - \frac{\omega_p^2}{\omega^2 + i\omega\Gamma}. \tag{2.28}$$

For the ideal free electron gas $\epsilon_\infty = 1$, and for typical metals $\epsilon_\infty = 1$ – 10 depending on spectral onset of the interband response [136, 37]. It is important to note that the real part of the dielectric function of metals is negative below the plasma frequency. This negative value of the dielectric function is essential for plasmonic resonances as discussed below.

2.2.3 Relationship between dielectric function and optical conductivity

The optical conductivity can be derived from the equation of motion in Eq. 2.24 as well. Under a time harmonic field

$$\mathbf{E}(t) = \mathbf{E}(\omega)e^{-i\omega t}, \tag{2.29}$$

the electron velocity $\mathbf{v} = \dot{\mathbf{x}}$ can be solved as

$$\mathbf{v} = -\frac{e}{m^*}\frac{1}{\Gamma - i\omega}\mathbf{E}(\omega) = -\frac{e\tau}{m^*}\frac{1}{1 - i\omega\tau}\mathbf{E}(\omega). \tag{2.30}$$

By relating the electron velocity $\mathbf{v}$ to the current $\mathbf{J}$, the optical conductivity $\sigma(\omega)$ can be derived as

$$\begin{aligned} \mathbf{J}(\omega) &= -Ne\mathbf{v} && (2.31)\\ &= \frac{Ne^2\tau}{m^*}\frac{1}{1 - i\omega\tau}\mathbf{E}(\omega) && (2.32)\\ &= \sigma(\omega)\mathbf{E}(\omega) && (2.33) \end{aligned}$$

with

$$\begin{aligned} \sigma(\omega) &= \frac{Ne^2\tau}{m^*}\frac{1}{1 - i\omega\tau} && (2.34)\\ &\equiv \frac{\sigma_0}{1 - i\omega\tau}. && (2.35) \end{aligned}$$

Here the DC conductivity σ_0 is defined as $\sigma_0 = \frac{Ne^2\tau}{m^*}$.

Based on the above derivations from the Drude model, we can connect $\epsilon(\omega)$ to $\sigma(\omega)$. [1] $\sigma(\omega)$ in Eq. 2.34 can be rewritten as

$$\frac{i}{\omega\epsilon_0}\sigma(\omega) = -\frac{Ne^2}{m^*\epsilon_0}\frac{1}{\omega^2 + i\omega/\tau}, \tag{2.36}$$

[1] The relation of dielectric function to optical conductivity is not uniquely defined, because under an AC field the free electron/current and induced electron/current are not easily distinguishable [13].

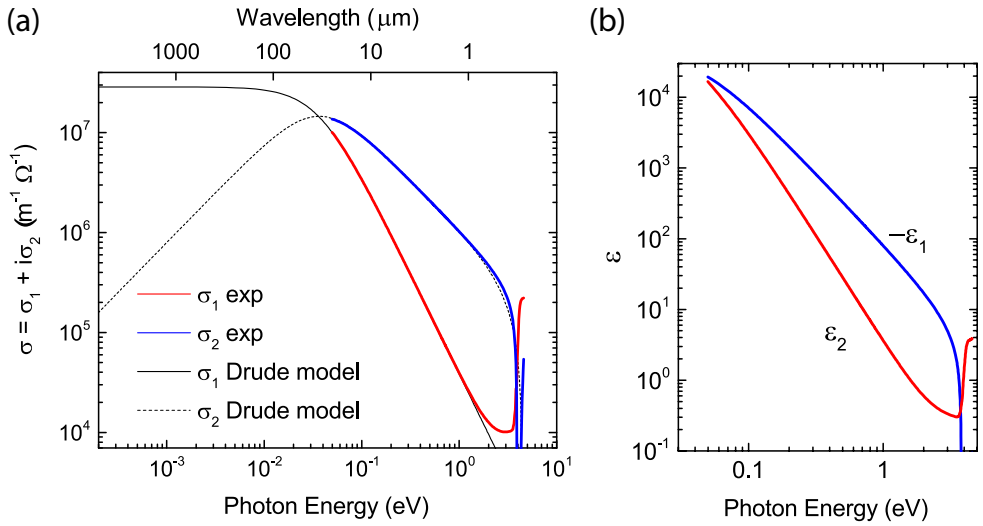

Figure 2.2: (a) Real and imaginary optical conductivity $\sigma(\omega) = \sigma_1(\omega) + i\sigma_2(\omega)$ of silver agrees well with Drude model predictions below the interband transition. (b) The corresponding dielectric function $\epsilon(\omega) = \epsilon_1(\omega) + i\epsilon_2(\omega)$ of silver.

Comparing Eq. 2.36 to Eq. 2.25, we get

$$\frac{i}{\omega\epsilon_0}\sigma(\omega) = -1 + \epsilon(\omega), \tag{2.37}$$

or

$$\epsilon(\omega) = 1 + \frac{i}{\epsilon_0\omega}\sigma(\omega). \tag{2.38}$$

More explicitly, the real and imaginary part of $\epsilon(\omega) = \epsilon_1(\omega) + i\epsilon_2(\omega)$ can be expressed as

$$\epsilon_1(\omega) = 1 - \frac{\sigma_2(\omega)}{\epsilon_0\omega}, \tag{2.39}$$

$$\epsilon_2(\omega) = \frac{\sigma_1(\omega)}{\epsilon_0\omega}, \tag{2.40}$$

where $\sigma_1(\omega)$ and $\sigma_2(\omega)$ are real and imaginary part of $\sigma(\omega)$.

The above derivation of optical conductivity and dielectric function $\epsilon(\omega)$ is based on the assumption of a Drude model for the free electron behavior, which is valid for noble metals below their interband transition. Fig. 2.2 shows $\sigma(\omega)$ and $\epsilon(\omega)$ of a commonly used metal for plasmonics – silver. In Fig. 2.2a, experimentally determined $\sigma_1(\omega)$ (red) and $\sigma_2(\omega)$ (blue) are shown together with the Drude model prediction (black) for frequency below 1 eV with good agreement. The

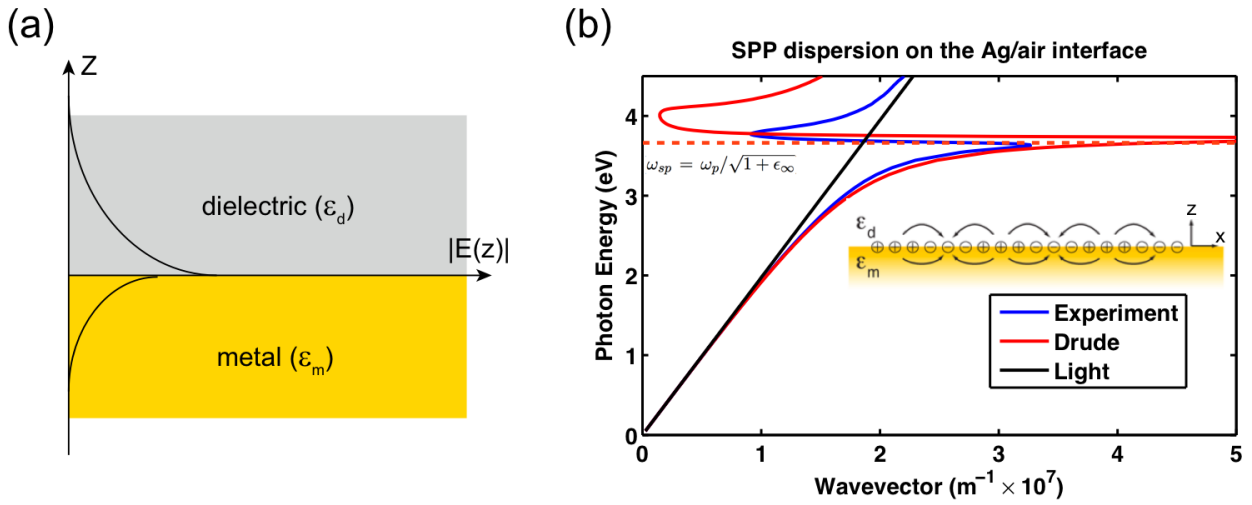

Figure 2.3: (a) Surface plasmon polariton (SPP) is spatially confined at the metal-dielectric interface, with the electric field exponentially decaying into the two surrounding media. (b) Dispersion relation of the SPP at the silver-air interface calculated from Eq. 2.41. The dispersion calculated using experimental dielectric function is shown in blue. In comparison, the result using the Drude model dielectric function is shown in red. The SPP dispersion relation deviates from that of light (black) at optical frequencies due to the spatial confinement of SPPs. Inset illustrates the coherent electron oscillation of SPPs.

corresponding dielectric function $\epsilon(\omega) = \epsilon_1(\omega) + i\epsilon_2(\omega)$ is shown in Fig. 2.2b, which will be discussed further in chapter 3.

2.3 Propagating surface plasmon polaritons

At the interface between a metal and a dielectric medium, optical excitation of free electrons can give rise to collective oscillation of surface charge density. This oscillation of surface charge density is coupled to the electromagnetic wave, and can propagate along the interface with evanescent confinement in the out-of-plane direction. This confined surface wave of collective oscillation of charge carrier and photon is called *surface plasmon polariton* (SPP).

These SPPs can be derived from Maxwell's equations as a special solution for propagating surface waves between a metallic and a dielectric interface with dielectric functions ϵ_m and ϵ_d, respectively [114, 194]. As illustrated in Fig. 2.3a, for a SPP propagating along x direction on the interface ($z = 0$) between a metal ϵ_m ($z < 0$) and a dielectric ϵ_d ($z > 0$), the resulting ω versus k_x

dispersion relation has a well defined expression of

$$k_x^2 = \frac{\omega^2}{c^2}\frac{\epsilon_m \epsilon_d}{\epsilon_m + \epsilon_d} \tag{2.41}$$

where k_x is the in-plane wavevector, ω the frequency of the light. For a special case of the dielectric being air ($\epsilon_d = 1$), the resonant condition is reached by setting zero for the denominator in Eq. 2.41, i.e., $\mathbf{Re}[\epsilon_m(\omega) + 1] = 0$. Fig. 2.3b shows the dispersion relation of SPP on an interface of silver and air. The dispersion relation is calculated both for the Drude model dielectric function (red) and for experimental silver dielectric function (blue). Compared to the wavevector of the light (black), the in-plane wavevector of the SPP is larger at optical frequencies. This large wavevector makes the SPPs decoupled to the free space plane waves, responsible for the long propagating distance along the surface. The dispersion relation calculated using Drude model dielectric function suggests that the in-plane wavevector of the SPP diverges at the surface plasmon frequency ($\omega_{sp} = \omega_p/\sqrt{1+\epsilon_\infty}$) and then transitions to a region with its value less than the wavevector of the light (i.e., no longer surface confined). The same behavior is seen with the dispersion relation calculated from experimental silver dielectric function, with difference at higher energy (> 3 eV) due to the interband effects.

2.4 Particle plasmon resonance: localized SPPs

Localized SPPs (LSPPs) are plasmon resonances on metal nanoparticles, and can be viewed as standing waves of SPPs along the surface of a particle [96]. Due to LSPPs, metal nanoparticles can efficiently couple to far-field electromagnetic waves, resulting in a large absorption and scattering cross-section, and manifesting as distinct colors depending on the size and geometry. The optical response of a nanoparticle can be understood through the frequency dependent polarizability $\alpha(\omega)$. For a spherical particle much smaller than the illuminating wavelength, the polarizability $\alpha(\omega)$ under electrostatic approximation is given by the Clausius - Mossotti relationship [106]

$$\alpha(\omega) = 4\pi r^3 \epsilon_0 \frac{\epsilon_m - \epsilon_d}{\epsilon_m + 2\epsilon_d} \tag{2.42}$$

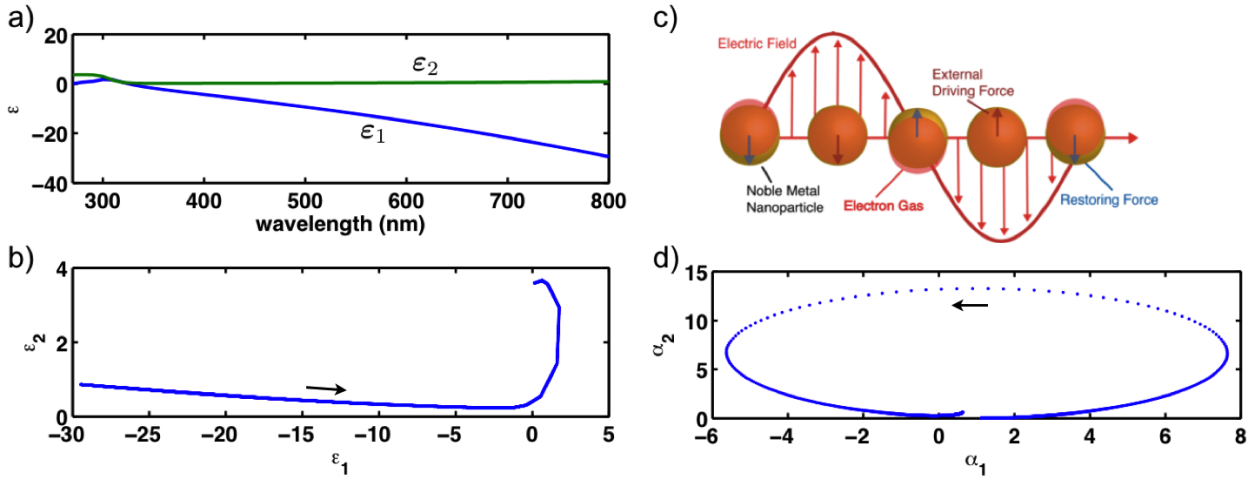

Figure 2.4: Particle plasmon resonance of a silver sphere. The dielectric function of silver ϵ_m is shown in (a), with its parametric plot for varying wavelength shown in (b). The arrow indicates the direction for increasing frequency or decreasing wavelength. (c) Illustration of the particle plasmon resonance under an applied electric field. A restoring force is applied to the electron motion from the boundary of the sphere. (d) The real and imaginary part of polarizability $\alpha(\omega) = \alpha_1 + i\alpha_2$ in a parametric plot when the frequency increases (counter clockwise) across the plasmon resonance.

with the radius of the particle r, the dielectric function of the metal $\epsilon_m(\omega)$ and the surrounding medium ϵ_d. Apparently, the polarizability $\alpha(\omega)$ has a resonance at $\mathbf{Re}[\epsilon_m + 2\epsilon_d] = 0$. With air $\epsilon_d = 1$ the resonance condition happens at $\mathbf{Re}[\epsilon_m(\omega)] = -2$, which for metal is in the visible spectral range.

The response of a silver particle to an applied electric field is illustrated in Fig. 2.4c. The plasmon resonance is a result of coherent motion of electrons under geometric constraints by the boundary of the particle. The polarizability $\alpha(\omega)$ across its resonance at $\lambda = 355$ nm for a silver particle is shown in (d) as a parametric plot. As the frequency increases (counter clock wise), the real part of the polarization α_1 starts close to 1 and increases till reaching near the resonance wavelength at $\lambda = 355$ nm. It then dramatically decreases and changes the sign on resonance, finally completes the circle back to 1 off resonance. The dielectric function of silver with a negative real part and a small imaginary part is the reason for this plasmonic resonance behavior (Fig. 2.4(a,b)).

To further illustrate the geometric dependence of the particle plasmon resonance, we can extend the analysis of a sphere to a spheroid particle ($a \neq b = c$). When the external field is

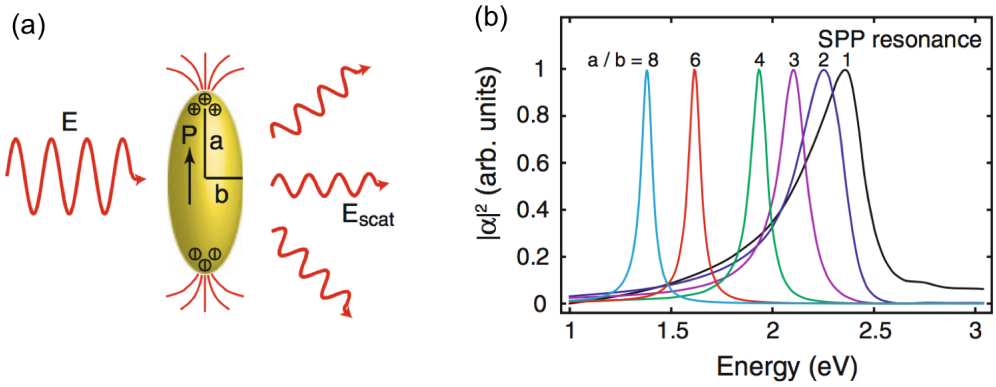

Figure 2.5: (a) Illustration of localized SPP of a gold spheroid particle with incoming field polarized along the semi-major axis. (b) shows the spectra for particles of different aspect ratio ($r = a/b$). The plasmon resonance red-shifts with increasing aspect ratio. Figure after [194].

polarized longitudinally along a prolate spheroid with dielectric function $\epsilon_m(\omega)$, the polarizability can be expressed analytically [164]:

$$\alpha(\omega) = 4\pi\epsilon_0 \cdot ab^2 \cdot \frac{\epsilon_m - \epsilon_d}{3[A(\epsilon_m - \epsilon_d) + \epsilon_d]} \tag{2.43}$$

$$= \frac{4\pi\epsilon_0}{3} \cdot ab^2 \cdot \frac{\epsilon_m - \epsilon_d}{\epsilon_d + A(\epsilon_m - \epsilon_d)} \tag{2.44}$$

with semi-major axes a, semi-minor axes b, and the depolarization factor A. The depolarization factor A depending on the aspect ratio $r = a/b$ is given by

$$A(r) = \frac{1}{2r^2} \int_0^\infty \frac{1}{(s+1)^{3/2}(s+r^{-2})} ds \tag{2.45}$$

$$= \frac{1}{1-r^2} - \frac{r \arcsin(\sqrt{1-r^2})}{(1-r^2)^{3/2}}. \tag{2.46}$$

The values of A for three special cases of $r \to 0$, $r = 1$, and $r \to \infty$ are listed:

$$\begin{cases} A = 1, & r \to 0, \quad \text{pancake-like, oblate ellipsoid} \\ A = \dfrac{1}{3}, & r = 1, \quad \text{sphere} \\ A = 0, & r \to \infty, \quad \text{cigar-like, prolate ellipsoid} \end{cases} \tag{2.47}$$

The spectral response of gold spheroids with different aspect ratio is shown in Fig. 2.5. As the aspect ratio increases from $r = 1$ with fixed semi-minor axis length, the SPP resonance red-shifts associated with a narrower line width.

Closely related to A is the field enhancement factor $\mathbf{E}_{\text{local}} = \xi\mathbf{E}(\omega)$ at the end of the semi-major axis of the spheroid particle, given by [149, 164, 217]:

$$\xi = |\frac{\epsilon_m}{1 + |\epsilon_m - 1|A}|, \tag{2.48}$$

assuming the surrounding is air with $\epsilon_d = 1$.

2.5 Optical antenna

As discussed above, a metallic nanoparticle can strongly couple to the incident field at resonance, resulting in an enhanced electric field confined to its surface. In addition, the resonance and coupling efficiency can be controlled with parameters such as geometry and material. These properties make optically resonant metallic structures in good analogy to radiofrequency (RF) antennas. Thus optically resonant metallic structures are also called *optical antennas*. Despite these similarities, the rules working for RF antennas cannot be readily applied to optical antennas, because the resonances of optical antennas are expressed in terms of bound surface waves with locally enhanced field. However, a connection between the RF antennas and optical antennas can be established by replacing the wavelength in free space λ by the resonance wavelength of propagating SPP λ_p, as explained by a Fabry-Pérot model [171, 96, 209, 56, 31]. The resonance occurs when propagating SPP mode forms a standing wave around an optical antenna.

The tip in *s*-SNOM also acts as an optical antenna, and it plays three key roles in the near-field interaction with the sample [179]. Firstly the tip receives and concentrates the light; secondly it mediates the local field coupling and energy transfer; lastly it serves as a local scattering source for far field detection. In this picture, an enhanced light-matter interaction can be achieved due to the increase in electromagnetic local density of states (EM-LDOS) in the near-field.

2.6 Principle of *s*-SNOM

After discussing the macroscopic behavior of optical properties of materials and the plasmonic properties associated with nanostructures, the *s*-SNOM technique to study the corresponding mi-

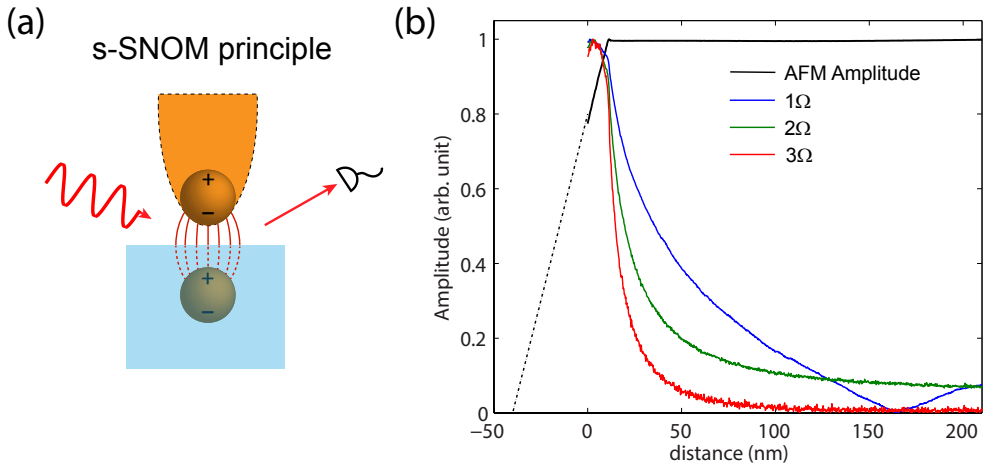

Figure 2.6: Distance dependence of the cantilever oscillation amplitude and the demodulated scattered light at different harmonics of the cantilever oscillating frequency. Here 2Ω stands for the second harmonics. As the tip gets close to the sample, the cantilever oscillation amplitude decreases due to the damping from the sample surface. In contrast, the 2Ω and 3Ω signals show exponential increase towards smaller tip-sample separation, with a decay length of about 20 - 30 nm. This is a result of evanescent character for near-field signal, which is responsible for high spatial resolution.

croscopic properties and the local field distributions is presented in this section. As shown in Fig. 2.6a, in a *s*-SNOM instrument the incident light is focused onto the AFM tip apex region and the scattered light carrying the optical properties of the sample is collected. The high spatial resolution of *s*-SNOM is provided by the localized light-matter interaction under the AFM tip. By raster scanning across the sample while detecting the elastically scattered light, the optical response of the sample is mapped with nanometer spatial resolution.

As the near-field region underneath the tip (10s nm) is much smaller than the area of the optical focus (10s μm), the scattered light contains both the near-field signal (E_s) and unspecific far-field background (E_b) scattered from both the tip shaft and the sample. In experiments, to extract the near-field signal the tip-sample distance is modulated by oscillating the AFM tip in non-contact mode, with a typical oscillation amplitude of 30 - 100 nm. The scattered light after collection is demodulated at the AFM oscillation frequency Ω and its higher harmonics $n\Omega$. The unspecific far-field background E_b dominates the DC and first harmonic demodulated signal (1Ω) at the detector, while the near-field signal E_s dominates in the higher harmonics due to the nonlinear tip-sample

coupling. The tip-sample distance dependence of the first three harmonics of the scattered light is shown in Fig. 2.6b. As the tip approaches the sample, the AFM cantilever oscillation amplitude (black) decreases linearly with distance due to additional forces and damping from interactions with the sample. At the same time, the higher harmonics of the scattered light (at 2nd and 3rd harmonics, i.e., 2Ω in green and 3Ω in red) increase exponentially in the short tip-sample separation, with a decay length of $\Delta z = 20 - 30$ nm. Due to this evanescent character, these signals at the higher harmonics represent the *near-field signal*. The in-plane spatial resolution of these near-field signal can be estimated from the evanescent wave formula, which can be represented as $E = E_0 \exp(ik_x + ik_y - \gamma_z z)$, with $1/\gamma_z = \Delta z$ the exponential decay length. From the conservation of momentum, we have

$$k_x^2 + k_y^2 = \gamma_z^2 + k_0^2 \approx \gamma_z^2. \tag{2.49}$$

The approximation is valid because the k-vector in z-direction γ_z is much bigger than the free space wavevector k_0. Thus the spatial resolution in-plane can be estimated as $\Delta x = 1/\max(k_x) \approx 1/\gamma_z = \Delta z = 20 - 30$ nm.

2.6.1 Modeling of tip-sample interaction in *s*-SNOM

To specifically address the role of the tip in *s*-SNOM, a model calculation can be employed. Here I only take the simplest model to illustrate the principle, because the quantitative interpretation of optical contrast of *s*-SNOM signal can be complicated due to the multiple interactions of tip, sample, and light [173]. As shown in Fig. 2.7, the tip considered as a small polarizable sphere of radius R is placed at height of h above a semi-infinite sample surface. The dielectric function of tip and sample are ϵ_t, and ϵ_s respectively. The induced dipole moment p of the tip under an vertically applied external field E_0 is [124, 195]

$$p = \alpha E_0, \tag{2.50}$$

where $\alpha = 4\pi\epsilon_0 R^3(\epsilon_\mathrm{t} - 1)/(\epsilon_\mathrm{t} + 2)$ is the dipole polarizability. The mirror image of the tip dipole formed at the sample is $p_\mathrm{imag} = \beta p$, with the reflection coefficient $\beta = (\epsilon_\mathrm{s} - 1)/(\epsilon_\mathrm{s} + 1)$ describing

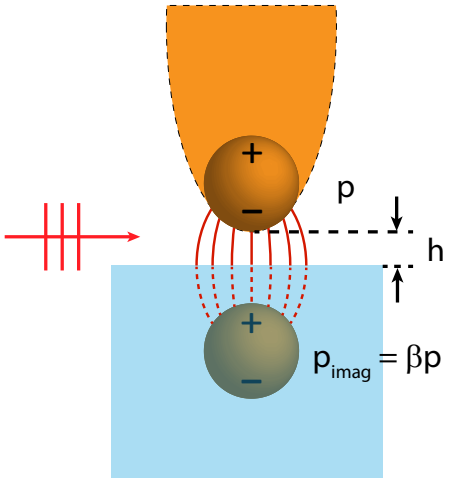

Figure 2.7: Illustration of the dipole model of *s*-SNOM. Incident field induces a dipole p at the tip with its image dipole on the sample $p_{\text{imag}} = \beta p$. The mutual interaction of the two dipoles forms a coupled polarization, responsible for the near-field signal in *s*-SNOM.

the effective surface charge response of the sample. The electric field produced by the image dipole p_{imag} at the center of tip is

$$E_i(R+d) = \frac{p_{\text{imag}}}{2\pi\epsilon_0\left[2(R+d)\right]^3}. \tag{2.51}$$

Thus the tip dipole p and its image p_{imag} on the sample mutually interact with each other, resulting in a recursive relation:

$$\begin{aligned} p &= \alpha\left[E_0 + E_i(R+d)\right] \\ &= \alpha\left[E_0 + \frac{\beta p}{2\pi\epsilon_0[2(R+d)]^3}\right] \\ &\equiv \alpha_{\text{eff}} E_0 \end{aligned} \tag{2.52}$$

where α_{eff} is the effective polarizability due to the mutual tip-sample interaction. Solving the recursive relation in Eq. 2.52, we get

$$\alpha_{\text{eff}} = \alpha\left[1 - \frac{\alpha\beta}{16\pi\epsilon_0(R+d)^3}\right]^{-1}. \tag{2.53}$$

According to the Mie theory [26], the scattered light off the tip is related to the effective polarizability through $I_s \propto |\alpha_{\text{eff}}|^2$. Thus by detecting the scattered light, information about the local dielectric function of the sample material can be obtained.

This simple point dipole model provides an intuitive picture to understand the mechanism of optical contrast. However, to quantitatively compare or to predict experimental results more theoretical efforts have been undertaken [234, 3, 97, 42, 16, 152]. These works include modeling the tip shape as a spheroid [42] or as a hyperboloid [16], and a more recent electromagnetic model taking field retardation and real probe geometry into account [152]. With the development of near-field optical spectroscopy both experimentally and theoretically, quantitative near-field modeling is expected to be able to directly convert experimental *s*-SNOM data to the optical properties of samples.

Chapter 3

The optical dielectric function of silver

An accurate dielectric function of silver is needed for a wide range of applications including plasmonics, optical antennas, and metamaterials. Both applied and fundamental properties such as surface plasmon propagation length, plasmon lifetime, non-radiative loss, and even the Casimir force, are sensitive to small variations of the dielectric function. As a result, the silver dielectric functions available in literature from decades ago no longer meet the needed accuracy. The measurement on silver is experimentally challenging with the values of dielectric function spanning over four orders of magnitude from nearly 2×10^4 at 0.05 eV to about 4 at 3 eV.

In this chapter, we determine the complex valued dielectric function of evaporated and template stripped polycrystalline silver films using broadband spectroscopic ellipsometry. The measurement covers from 0.05 eV ($\lambda = 25$ μm) to 4.14 eV ($\lambda = 300$ nm) with a statistical uncertainty of less than 1%. From Drude analysis of the 0.1 – 3 eV range, values of the plasma frequency $\hbar\omega_p = 8.9 \pm 0.2$ eV, dielectric function at infinite frequency $\epsilon_\infty = 5 \pm 2$, and relaxation time $\tau = 1/\Gamma = 17 \pm 3$ fs are obtained, with the absolute uncertainties estimated from systematic errors and experimental repeatability. Further analysis based on the extended Drude model reveals an increase in τ with decreasing frequency in agreement with Fermi liquid theory, and extrapolates to $\tau = 22 \pm 5$ fs at zero frequency. A deviation from simple Fermi liquid behavior is noticed at energies below 0.1 eV ($\lambda = 12$ μm) with the onset of a further increase in τ connecting to the DC value from

Work in this chapter is published in Physical Review B 91, 235137 (2015)

transport measurements of $\sim$ 40 fs. The results are consistent with a wide range of optical and plasmonic experiments throughout the infrared and visible/ultraviolet spectral range [161, 101, 25]. The influence of grain boundaries, defect scattering, and surface oxidation is discussed. The results are compared with our previous measurements of the dielectric function of gold [Olmon *et al.*, Phys. Rev. B **86**, 235147 (2012)].

3.1 Introduction

The dielectric function of silver together with that of other noble metals has played an important historical role in the understanding of the electronic structure of metals [48, 49, 214, 61, 136]. This role continues for understanding the ultrafast electron dynamics of metals [6, 146, 33, 41, 159, 92, 90]. Silver in particular has a special status due to its high optical conductivity and wide range of applications from mirrors to plasmonics and optical metamaterials.

However, similarly to the case of gold [180], large variations exist among historical measurements of the dielectric function of silver, especially for the imaginary part near the interband transition in the visible/ultraviolet (Vis/UV) region [145]. Most of these measurements only cover a narrow energy range, making a direct comparison between the different experiments difficult. In addition, discrepancies between theoretical and experimental values of different optical and plasmonic properties of silver have raised concerns over the accuracy of some of the most widely used data of the dielectric function of silver [190, 163, 210, 161, 101, 162, 95, 25, 226, 109]. Accurate values for the dielectric function of silver are needed in the visible and infrared (IR) spectral ranges, because many important parameters, such as surface plasmon propagation length, plasmon lifetime, non-radiative loss, and even the Casimir force, are sensitively linked to small variations of the dielectric function [180].

In this work, we provide a comprehensive measurement of the optical dielectric function $\epsilon(\omega)$ of evaporated and template-stripped polycrystalline silver using spectroscopic ellipsometry, covering a broad spectral range throughout the mid-IR to Vis/UV of two orders of magnitude, from 0.05 eV to 4.14 eV (25 μm to 300 nm). We analyze the free electron behavior below the interband

transition using the Drude model with plasma frequency ω_p, dielectric function at infinite frequency ϵ_∞, and relaxation time $\tau = 1/\Gamma$. While there is a good agreement of ω_p and ϵ_∞ with many past measurements, our value of $\tau = 17 \pm 3$ fs is significantly smaller than the commonly used literature value from Johnson and Christy of 31 ± 12 fs [112] and the value derived from DC conductivity of ~ 40 fs [60, 151], yet consistent with most optical and plasmonic experiments, such as typical surface plasmon propagation length and particle plasmon resonance lifetimes [184, 235, 162, 161, 25]. The difference in τ between the DC and the optical frequency measurements is due to the frequency dependence of the scattering rate $1/\tau(\omega)$ [75, 208]. An analysis with extended Drude model extracts this frequency dependence, which is found to be consistent with Fermi liquid theory beyond 0.1 eV [185, 75, 229]. However, at energies below 0.1 eV $\tau(\omega)$ rises more rapidly than suggested by the Fermi liquid theory possibly connecting to the Drude DC value of 40 fs. We discuss effects of impurity and grain boundary scattering, and note that even for samples prepared under nominally identical conditions, sample-to-sample variations can be as large as 30% for the imaginary part ϵ_2 near the interband transition.

3.1.1 Past measurements of dielectric function

Many previous experiments have measured the dielectric function of silver, based on different methods, and with partially inconsistent values. Fig. 3.1a shows selected examples of studies representative of the different experimental methods and measurement ranges, with the spectral range and the year of publication. For comparison, the range of our measurements is shown in red.

Various measurement techniques and deposition methods have been employed in previous measurements [145, 223, 181, 69]. Drude's polarimetric methods were used in early studies of evaporated metallic thin films. For example, reflectance measurements with different polarizations were carried out by Dold and Mecke on evaporated silver on polished glass to determine n and k in the range of 0.13 – 1 eV [55]. The same measurement method was applied to polycrystalline silver by Winsemius *et al.* in vacuum covering 0.5 – 5.4 eV [225]. An interferometric method was developed by Schulz to determine the extinction coefficient κ from the phase change of reflection at

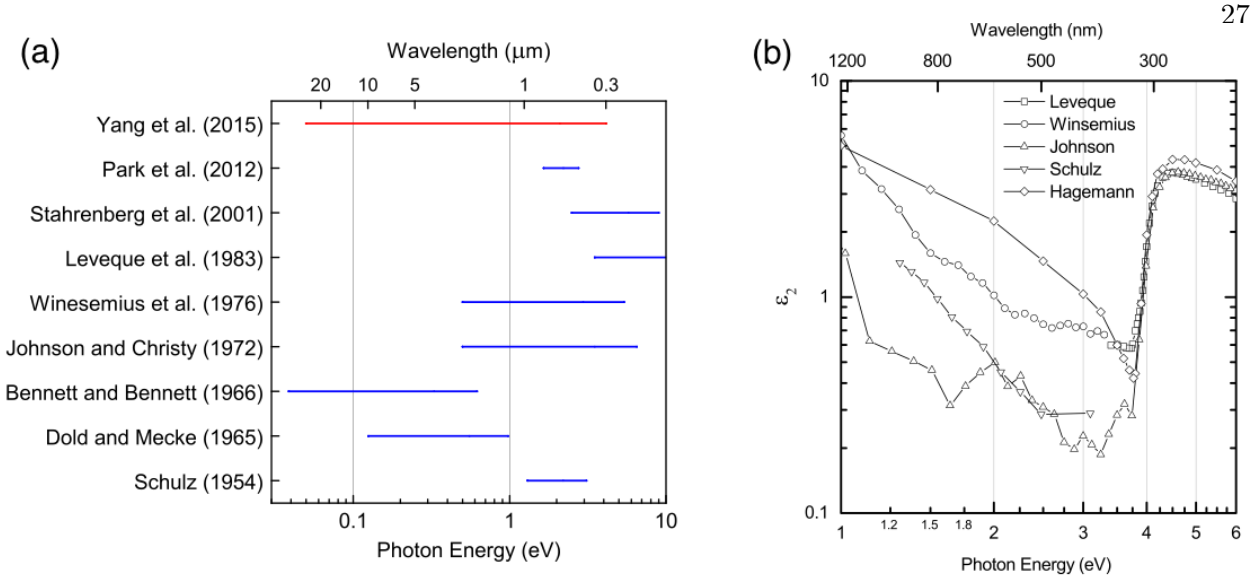

Figure 3.1: (a) Six decades of dielectric function measurements of Ag covering different spectral regions. Our measurement broadly covering the mid-IR to Vis/UV range is shown in red. (b) The existing literature values are in part inconsistent, mostly notably in the Vis/UV spectral range. Data from Leveque *et al.* [135], Winsemius *et al.* [225], Johnson and Christy (Johnson) [112], Schulz [205, 206], and Hagemann *et al.* [93].

normal incidence from 1.3 to 3.1 eV [204, 205]. More specifically, Ag-x-Ag multilayers were used in his experiment with x being mica or other dielectric material. In a separate study Schulz calculated index of refraction n from measured reflectivities at an incidence angle of 45° with a predetermined extinction coefficient κ from the above multilayer measurement [206]. The most common method to obtain the dielectric function is to apply Kramers-Kronig analysis on reflectance or transmission spectra of silver films. Hagemann *et al.* performed transmission measurements on evaporated silver thin films on collodion substrates in the range of 13 – 150 eV [93]. The resulting spectrum was complemented with other data in literature to yield a broad spectral range for proper Kramers-Kronig analysis. Similar measurements of silver films were carried out by Leveque *et al.* in vacuum after sample evaporation in the same chamber without exposing to air [135]. The reflectance spectrum from 3.5 to 30 eV was again extended with other data from literature for a Kramers-Kronig analysis. Similarly, Quinten developed a method for determining the dielectric function of metallic clusters from Kramers-Kronig analysis of optical extinction spectra [190]. Combined

reflectance and transmittance measurements of semitransparent thin films prepared by evaporation on fused quartz were done by Johnson and Christy in the range of 0.5 – 6.5 eV [112]. In their work, contour plots of the reflectance and transmittance were used to determine the complex index of refraction $N(\omega) = n(\omega) + i\kappa(\omega)$. In the visible spectral range from 1.38 to 2.76 eV, angle dependent surface plasmon-polaritons resonances on a silver-covered silica grating were used by Nash and Sambles to calculate the dielectric function [163]. More recently, spectroscopic ellipsometry was used to obtain the dielectric function with improved acquisition speed and accuracy over a broad spectral range limited only by light sources and detectors [218]. Stahrenberg *et al.* prepared clean surfaces of single crystal Ag *in situ* by ion sputtering and annealing [212]. Subsequent ellipsometry measurements were taken in the same ultrahigh vacuum environment in the spectral range of 2.5 – 9.0 eV using a synchrotron light source. Park *et al.* measured template stripped silver with reduced roughness by ellipsometry in the visible spectral range of 1.65 – 2.75 eV [184, 183].

Only one previous measurement has yet addressed the low energy range below 0.2 eV ($> 6\mu$m) [18]. In that study, reflectance at normal incidence was measured in the 3 – 30 μm wavelength range by Bennett and Bennett. The experimental reflectivity was compared to the calculated reflectivity from Drude model with good agreement. However, since reflectivity itself is not sufficient to constrain the three parameters in the Drude model, a value of $\tau = 36$ fs based on DC conductivity was assumed for data modeling.

3.1.2 Drude model and extended Drude model

Silver, being a face-centered cubic (FCC) crystal lattice, is optically isotropic [13, 29]. Its relative dielectric function $\epsilon(\omega) = \epsilon_1(\omega) + i\epsilon_2(\omega)$ can describe the full electromagnetic response of the medium in the absence of magnetic effects. Derived in Eq. 2.38, the dielectric function $\epsilon(\omega)$ connects to the frequency dependent complex conductivity $\sigma(\omega) = \sigma_1(\omega) + i\sigma_2(\omega) = -i\epsilon_0\omega(\epsilon(\omega) - 1)$, where the real part $\sigma_1(\omega)$ describes the Ohmic loss and the imaginary part $\sigma_2(\omega)$ defines the phase lag between the applied electric field and the electric current.

In the low energy region, considering only electronic intraband transitions within the conduc-

tion band, the dielectric function of silver can be described to a good approximation by the Drude model. The Drude model dielectric function is derived in Eq. 2.28 and has the expression of

$$\epsilon(\omega) = \epsilon_\infty - \frac{\omega_p^2}{\omega^2 + i\omega\Gamma}, \tag{3.1}$$

where the volume plasma frequency ω_p is related to the effective mass of the electron m^* and the electron density N through $\omega_p = (Ne^2/\epsilon_0 m^*)^{1/2}$. The relaxation rate Γ describes the effective electron scattering rate, with a corresponding relaxation time $\tau = 1/\Gamma$. The parameter ϵ_∞ accounts for the net contribution from the positive ion cores. For the ideal free electron gas $\epsilon_\infty = 1$, and for typical metals $\epsilon_\infty = 1$ – 10 depending on the interband response [136, 37]. The contribution to the dielectric function from the interband transition of *d*-band to *sp*-band can empirically be accounted for by functions of damped harmonic oscillators [194, 75].

The real $\epsilon_1(\omega)$ and imaginary part $\epsilon_2(\omega)$ of the dielectric function in Eq. 3.1 have the form

$$\epsilon_1(\omega) = \epsilon_\infty - \frac{\omega_p^2}{\omega^2 + \Gamma^2} \approx \epsilon_\infty - \frac{\omega_p^2}{\omega^2}, \quad \text{and} \tag{3.2}$$

$$\epsilon_2(\omega) = \frac{\omega_p^2\,\Gamma}{\omega(\omega^2 + \Gamma^2)} \approx \frac{\omega_p^2\,\Gamma}{\omega^3}, \tag{3.3}$$

with the approximations valid for $\omega \gg \Gamma$. Eqs. 3.2 and 3.3 allow for the direct calculations of ω_p, ϵ_∞, and Γ from $\epsilon_1(\omega)$ and $\epsilon_2(\omega)$ for large frequencies.

The Drude model provides an effective description of the free carrier response in metals. The neglected Coulomb interactions between electrons can be described by *Fermi liquid theory* [33, 147, 146, 83]. In the Fermi liquid theory, a free quasiparticle picture is used to explain the macroscopic response of the interacting electron system with frequency dependent renormalized effective electron mass m^* and relaxation time τ [185, 83]. Drude model can be modified accordingly to capture the Coulomb interactions by introducing a frequency dependence to the Drude parameters [229, 129], which becomes the extended Drude model. With frequency dependent Drude parameters, Eq. 3.1 becomes

$$\epsilon(\omega) = \epsilon_\infty - \frac{\omega_p(\omega)^2}{\omega^2 + i\omega/\tau(\omega)^2}, \tag{3.4}$$

with real and imaginary parts given by

$$\epsilon_1(\omega) = \epsilon_\infty - \frac{\omega_p(\omega)^2}{\omega^2 + 1/\tau(\omega)^2}, \qquad \text{and} \tag{3.5}$$

$$\epsilon_2(\omega) = \frac{\omega_p(\omega)^2}{\omega^2 + 1/\tau(\omega)^2} \cdot \frac{1}{\omega\tau(\omega)}. \tag{3.6}$$

Equating the common factor in the real and imaginary part, the relaxation time $\tau(\omega)$ can be expressed as

$$1/\tau(\omega) = \frac{\omega\epsilon_2(\omega)}{\epsilon_\infty - \epsilon_1(\omega)}. \tag{3.7}$$

Deviations from the Drude model have been noticed in recent experiments due to both intrinsic and extrinsic effects, including band structure, impurity, and surface effects [216, 140, 88]. In the study of DC conductivity of metals, intrinsic effects can be determined after consideration of extrinsic effects from systematic studies under controlled temperature and impurity levels [215, 131, 151]. In contrast, the determination of the spectroscopic behavior of the dielectric function at optical frequencies is more involved. However, with an accurate measurement of the dielectric function of silver over a broad spectral range, we can quantitatively compare the experimental dielectric function with different models and literature, thus posing constraints on intrinsic and extrinsic effects.

3.2 Experiment

Template stripped (TS) silver films deposited on Si substrates were chosen for spectroscopic ellipsometry measurement over the range of 0.05 – 4.14 eV. The experimental procedure is generally similar to our previous measurements on gold [180]. The deposition of the metal on a flat substrate (template) leads to a smooth and more homogeneous metal surface at the metal-substrate interface compared to the vacuum side of the film. The metal film can then be stripped off the substrate to reveal the desired surface. For template stripping we use a silicon wafer with a native oxide layer (Si/SiO_2) (University Wafer) as substrate, ultrasonically cleaned in isopropyl alcohol and dried with nitrogen. Silver pellets of 99.99% pure element (Kurt J. Lesker) are evaporated in a cryopumped

evaporator (E360A, Edwards) from a molybdenum boat at a pressure of $< 10^{-6}$ mbar. A silver film of thickness 150 nm (optically opaque and thick enough to resemble the bulk properties of silver through most of the spectral region studied) is deposited at a rate of 0.1 – 0.2 nm/s. The substrate is not heated during evaporation. In order to transfer and expose the desired metal surface after evaporation, the sample is glued with the vacuum silver side (fiber optic grade epoxy, EpoTek 377, EpoTek) to another cleaned piece of Si wafer, and the epoxy cured at 150°C for 30 min. To minimize the effect of surface oxidation [17], samples are then stripped to expose the Ag film but only shortly before the measurement. Fig. 3.2 shows the sample preparation procedure before and after stripping.

Template stripping is preferred over other methods for sample preparation, because of the reduced surface roughness and larger grain size [224]. In addition, the final metal surface remains protected from oxidation and contaminations from atmosphere prior to measurement. The TS silver films are carefully characterized for surface defects. Dark field optical microscopy is used for inspection over the whole sample surface, noting no visible defects. For local area characterization, the samples are analysed by non-contact atomic force microscopy (AFM, Innova, Bruker) shown in Fig. 3.3. Root mean square (rms) surface roughness of 1.2 nm was obtained for TS silver with estimated average grain size of 100 nm, comparable to the best literature values [224, 184, 162]. For comparison, the evaporated Ag side before template stripping exhibits rms roughness of 2.4 nm and grain size of 50 nm. For direct comparison and to test consistency with our earlier work [180], we also measured the dielectric function of gold. TS gold samples were prepared in the same

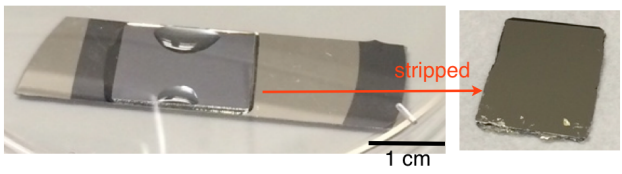

Figure 3.2: After evaporating a silver film on a silicon substrate, another silicon wafer is glued on top with a low viscosity epoxy. The silver film will stick to the epoxy and thus to the top silicon wafer after drying. The top silicon wafer can be easily peeled off with the silver film as shown in the right picture.

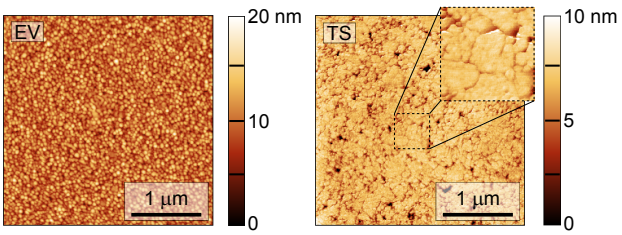

Figure 3.3: AFM topography of evaporated (EV) and template-stripped (TS) silver surface, with root mean square (rms) surface roughness of 2.4 nm, and 1.2 nm, respectively. The average grain size for EV is about 50 nm and that for TS is about 100 nm as derived from the Fourier transform analysis of the topography image.

way as the silver samples.

In contrast to standard reflectivity methods which only record the intensity, spectroscopic ellipsometry provides direct access to the complex dielectric function from two independent parameters [174]. Fig. 3.4 shows the configuration of an ellipsometer. Ellipsometry relies on the measurement of the ratio of complex reflectance $\rho(\omega)$, given by the ratio of reflection coefficients for p- and s-polarization

$$\rho(\omega) = r_p(\omega)/r_s(\omega) = (\tan\Psi)e^{i\Delta}, \tag{3.8}$$

with amplitude ratio $\tan\Psi$ and phase difference $\Delta = \phi_p - \phi_s$. By measuring only the relative reflectivities of different polarizations, ellipsometry does not require a reference sample or Kramers-Kronig analysis [218, 174]. The nature of measuring relative values also makes the method robust to intensity fluctuations of the source.

The relation connecting the ellipsometry measurements to the dielectric function ϵ can be derived from Fresnel's equation

$$r_p = \frac{\epsilon\cos\theta - \sqrt{\epsilon - \sin^2\theta}}{\epsilon\cos\theta + \sqrt{\epsilon - \sin^2\theta}}, \tag{3.9}$$

$$r_s = \frac{\cos\theta - \sqrt{\epsilon - \sin^2\theta}}{\cos\theta + \sqrt{\epsilon - \sin^2\theta}}, \tag{3.10}$$

where θ is the angle of incidence with respect to the surface normal of the sample. The ratio of the reflection coefficients ρ is [218, 174]

$$\rho = \frac{r_p}{r_s} = \left(\frac{\epsilon\cos\theta - \sqrt{\epsilon - \sin^2\theta}}{\epsilon\cos\theta + \sqrt{\epsilon - \sin^2\theta}}\right) \Big/ \left(\frac{\cos\theta - \sqrt{\epsilon - \sin^2\theta}}{\cos\theta + \sqrt{\epsilon - \sin^2\theta}}\right). \tag{3.11}$$

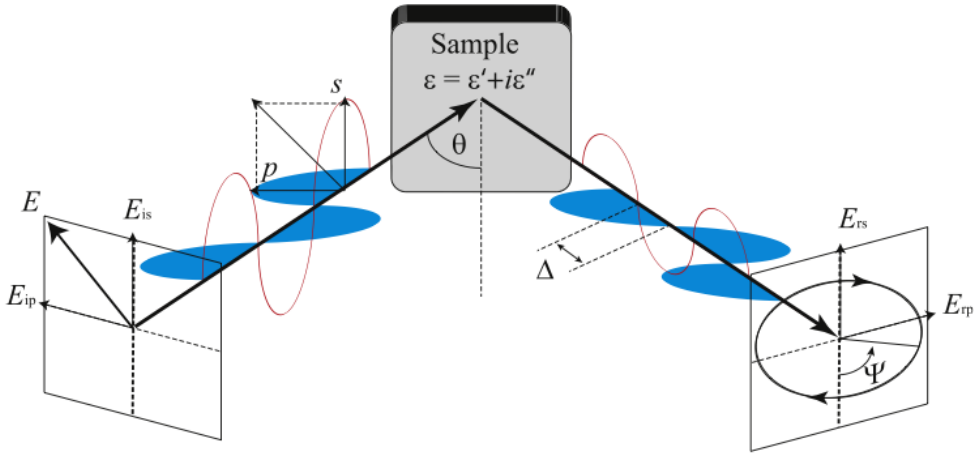

Figure 3.4: Configuration of an ellipsometer. An incident beam containing both s- and p-polarized light after reflected from the sample surface will cause a phase delay of one polarization with respect to the other by amount of Δ. In addition the amplitudes of the reflected beam get attenuated differently with a ratio $|r_p/r_s| = \tan\Psi$. For an isotropic bulk-like sample, the two unknowns of the dielectric function ϵ_1 and ϵ_2 can be determined from the two parameters of Δ and Ψ at each wavelength. Figure after [174].

For a uniform, isotropic, and optically opaque material with a smooth surface the relative dielectric function $\epsilon(\omega)$ is directly related to $\rho(\omega)$ through

$$\epsilon(\omega) = \sin\theta^2 \left(1 + \tan\theta^2 \left(\frac{1-\rho(\omega)}{1+\rho(\omega)}\right)^2\right). \tag{3.12}$$

We used two variable angle spectroscopic ellipsometers (VASE and IR-VASE, J. A. Woollam). VASE (variable angle spectroscopic ellipsometer) for the spectral range from 0.62 eV to 4.14 eV (2 μm – 300 nm) consists of a Xenon lamp with a monochromator. IR-VASE, covering 0.05 – 0.73 eV (25 – 1.7 μm), uses a glow bar as light source and is based on a Fourier-transform spectrometer.

According to the manufacturer calibration, the accuracy of both instruments tested in transmission without a sample loaded is better than $\delta\Psi = \pm 0.14°$ and $\delta\Delta = \pm 0.8°$ for IR-VASE, and $\delta\Psi = \pm 0.03°$and $\delta\Delta = \pm 0.2°$ for VASE. Factory calibration for both of the instruments has been performed using a Si/SiO_2 calibration sample. In addition, ellipsometers in two different labs have been cross-checked to eliminate the possibility of systematic errors as discussed previously [180].

Measurements are taken and averaged at three angles of incidence of 65°, 70° and 75°. The angles are chosen to have a high sensitivity to the differentiation between p- and s- polarized light

upon reflection. To further reduce noise, long measurement times of 5 hours for IR and 3 hours for Vis/UV lead to a statistical uncertainty $< 1\%$ over the full spectral range.

An in-plane isotropic optical response is assumed for silver with negligible depolarization upon reflection at the surface. The dielectric function is therefore directly determined from the measurement of Δ and Ψ using Eqs. 3.8 and 3.12. The data from this direct inversion retains the uncertainty due to instrumental errors, which we use later to characterize the error in our measurement. Due to residual instrumental errors the data are not perfectly Kramers-Kronig consistent. We therefore fit a combination of a Drude response and three Gaussian functions to the data with good agreement over the full spectral range. A similar fitting procedure was applied in our previous work on gold [180]. We provide the raw data of both silver and our previous gold measurements in the appendix.

3.3 Results

Negative real $-\epsilon_1$ and imaginary part ϵ_2 of the dielectric function in the Vis/UV spectral range of 1 – 6 eV are shown in Fig. 3.5 and Fig. 3.6, respectively. Results from three measured TS silver samples are plotted in red (A), green (B), and blue (C). The inset in Fig. 3.5 shows $-\epsilon_1(\omega)$ near the interband transition in a linear plot, where $-\epsilon_1(\omega)$ undergoes a sign change due to the interband transition from the occupied d band to the partially filled sp band. Correspondingly, $-\epsilon_1$ and ϵ_2 of the IR spectral range 0.05 – 1 eV are shown in Fig. 3.7 and Fig. 3.8, respectively.

In the spectral range of 1 – 6 eV, data for $\epsilon_1(\omega)$ and $\epsilon_2(\omega)$ from Leveque *et al.* [135] (squares), Winsemius *et al.* [225] (circles), Johnson and Christy [112] (triangle), Schulz [205, 206] (inverted triangle), and Hagemann *et al.* [93] (diamond) are shown for comparison in Fig. 3.5 and Fig. 3.6. In the IR spectral range of 0.03 – 1 eV, Fig. 3.7 and Fig. 3.8 show data from Winsemius *et al.* [225] (circles), Johnson and Christy [112] (triangle), Dold and Mecke [55] (inverted triangle), and Bennett and Bennett [18] (diamond).

For ϵ_1 the relative variations among literature values increase towards the visible spectral range, with the largest differences near the interband transition edge at ~ 3.8 eV. In particular, the

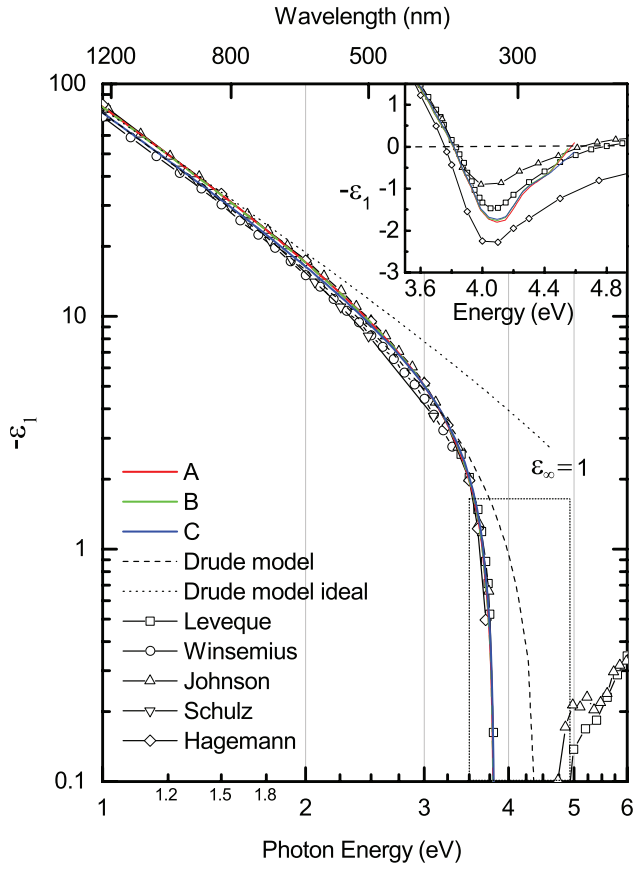

Figure 3.5: Negative real part of the dielectric function of silver $-\epsilon_1$ in the visible/ultraviolet spectral range for three different samples A(red), B(green), and C(blue). Data from Leveque *et al.* [135] (squares), Winsemius *et al.* [225] (circles), Johnson and Christy [112] (triangle), Schulz [205, 206] (inverted triangle), and Hagemann *et al.* [93] (diamond) are shown for comparison. Drude fit for sample C with $\hbar\omega_p = 8.9$ eV, $\tau = 18$ fs, and $\epsilon_\infty = 5$ (dashed) or $\epsilon_\infty = 1$ (dotted line). Inset: data near 3.8 eV shown in linear scale, where $-\epsilon_1(\omega)$ transitions from positive to negative values due to the interband transition.

values for ϵ_2 scatter widely below 3.8 eV as seen in Fig. 3.6. Our data in general fall in between the results from Johnson and Christy [112], and Winsemius *et al.* [225]. Compared to [112], we have good agreement of $-\epsilon_1$, but find a considerably larger ϵ_2 in the near-IR. This implies a considerably smaller value of τ compared to the results from Johnson and Christy as discussed below. Note that a careful inspection of the original data of ref. [112] shows a large uncertainty of over 40% in n in the energy range of 0.6 – 3 eV. As a result, with $\epsilon_2 = 2nk$, values of ϵ_2 from Johnson and Christy scatter strongly due to the large uncertainty in n.

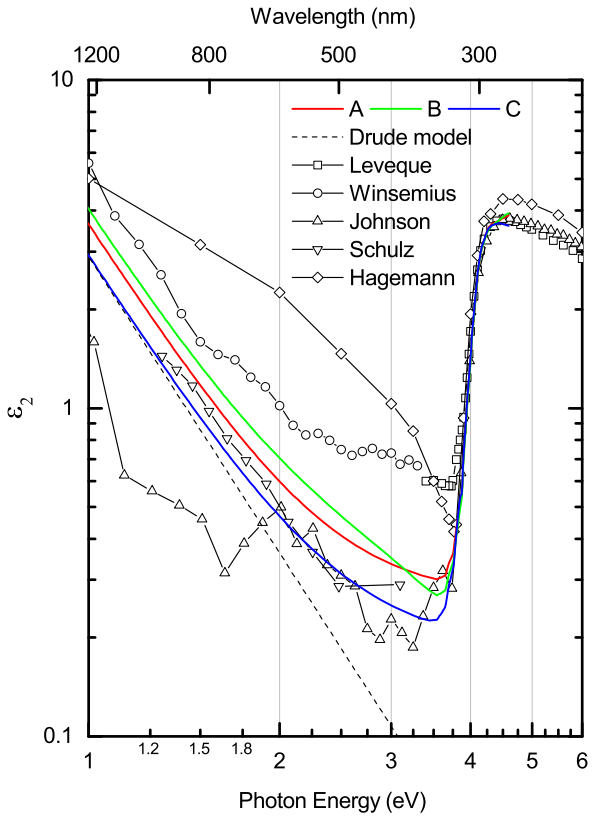

Figure 3.6: Imaginary part of dielectric function of silver ϵ_2 in the visible/ultraviolet spectral range for samples A(red), B(green), and C(blue). Data from Leveque *et al.* [135], Winsemius *et al.* [225], Johnson and Christy (Johnson) [112], Schulz [205, 206], and Hagemann *et al.* [93] are shown, as well as the result for the Drude model fit to sample C with parameters $\hbar\omega_p = 8.9$ eV, $\epsilon_\infty = 5$, $\tau = 18$ fs.

3.3.1 Drude Analysis

To obtain the Drude parameters ω_p, ϵ_∞, and τ, we fit our data to Eq. 3.1 in the range of 0.1 – 3 eV with simulated annealing algorithm by minimizing the least error for $\epsilon_1(\omega)$ and $\epsilon_2(\omega)$ simultaneously [180, 121]. We limit the energy range to 0.1 – 3 eV for the fit to minimize the effect of a frequency dependence of τ at low frequency. Above 3 eV, ϵ_∞ can no longer effectively account for the interband effects.

The fit results for samples A, B, and C are listed in Table. 3.1, with τ ranging from 15 to 18 fs for the different samples. The mean values for the three samples are $\hbar\omega_p = 8.9 \pm 0.2$ eV, $\epsilon_\infty = 5 \pm 2$, and $\tau = 17 \pm 3$ fs. The errors are calculated based on variations of the fit between the raw data

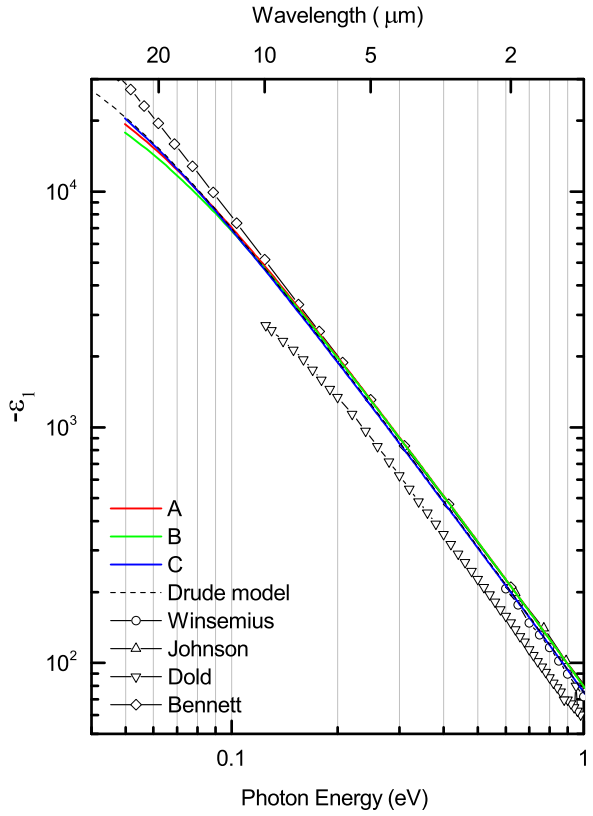

Figure 3.7: Negative real part of silver dielectric function -ϵ_1 in the infrared spectral range for samples A – C (red, green, and blue). Data from [225, 55, 112, 18] are shown together with the Drude model fit to sample C (see text).

and the Kramers-Kronig corrected data. The source of errors mainly comes from instrumental uncertainties as discussed in appendix. The dashed line in Figs. 3.5 – 3.8 is the dielectric function calculated for Drude model using Eq. 3.1 with parameters $\hbar\omega_p = 8.9$ eV, $\epsilon_\infty = 5$, and $\tau = 18$ fs for sample C. The Drude fit has perfect agreement at low energies as expected. ϵ_∞ effectively describes the cumulative response of the bound electrons to the first order. With $\epsilon_\infty = 5$ we can describe the onset of the interband transition.

An alternative way to extract the Drude parameters is based on the approximation in Eqs. 3.2 and 3.3. In the frequency range with $\omega \gg \Gamma$ but still below the interband transition, the slope of $-\epsilon_1(\omega)$ vs $1/\omega^2$ directly provides ω_p^2, the ratio of $\epsilon_2(\omega)$ vs $1/\omega^3$ gives $\omega_p^2 \times \Gamma$, and the offset of $\epsilon_1(\omega)$ extrapolated at $1/\omega^2 = 0$ provides ϵ_∞. Using this approach from 0.4 – 2 eV (3.1 μm – 620 nm)

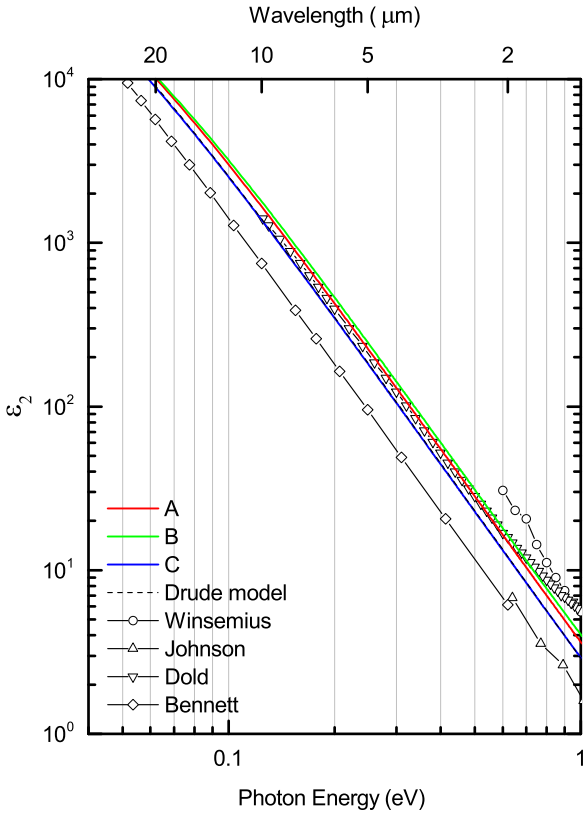

Figure 3.8: Imaginary part of silver dielectric function ϵ_2 in the infrared spectral range for samples A – C (red, green, and blue) in comparison with literature from [225, 55, 112, 18] and the Drude model fit to sample C (see text).

Table 3.1: Derived $\omega_p, \epsilon_\infty, \tau$ from Drude fit in the energy range of 0.1 – 3 eV for the three samples. The comparison to literature values are discussed in section 3.4.1.

	$\hbar\omega_p$ (eV)	τ (fs)	ϵ_∞
A	8.9 ± 0.2	17 ± 2	5 ± 2
B	8.9 ± 0.2	15 ± 2	4 ± 2
C	8.9 ± 0.2	18 ± 1	5 ± 2

values for $\hbar\omega_p$ of 8.7 eV, 8.9 eV, and 9.0 eV, ϵ_∞ of 6, 4, 5, and τ of 17 fs, 16 fs, and 18 fs, are obtained for sample A, B and C, respectively. The results from the two methods are consistent.

Despite an overall good agreement to the Drude model, a deviation of the Drude fit from the direct inverted dielectric data of ϵ_2 at energies below 0.1 eV and at high energies above 3 eV are noted (see appendix). The deviations at high energies are due to the interband transition. The

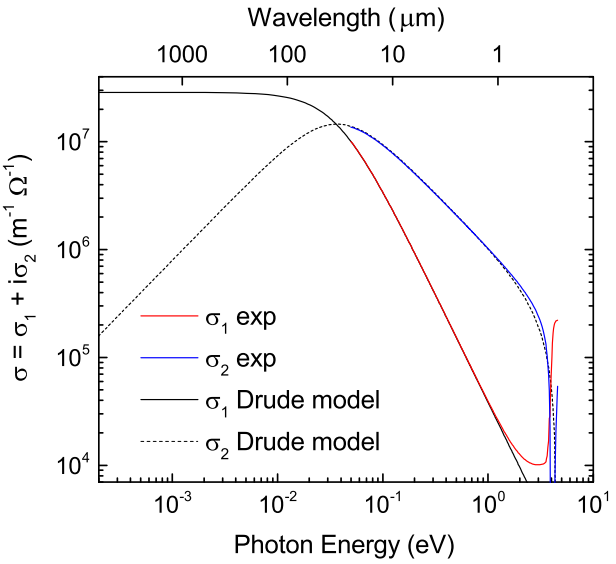

Figure 3.9: Optical conductivity $\sigma(\omega) = \sigma_1(\omega) + i\sigma_2(\omega)$ of sample C (red, blue). Drude model fit for the real part (solid black) and the imaginary (dashed black) with $\hbar\omega_p = 8.9$ eV, $\epsilon_\infty = 5$, $\tau = 18$ fs.

deviations of low energy ϵ_2 from Drude model is possibly due to an energy dependence of τ as predicted by Fermi liquid theory.

3.3.2 Optical conductivity and skin depth

The derived complex optical conductivities $\sigma_1(\omega)$ (red) and $\sigma_2(\omega)$ (blue) from the dielectric function of sample C are shown in Fig. 3.9. The solid and dashed black lines are Drude fits to the real and imaginary part of the conductivity, with parameter $\hbar\omega_p = 8.9$ eV, $\epsilon_\infty = 5$, and $\tau = 18$ fs.

In the low frequency region with $\omega\tau \ll 1$, the optical properties are mainly determined by the DC conductivity with $\sigma_{\mathrm{DC}} \approx \sigma_1 \gg \sigma_2$. Extrapolated $\sigma_{\mathrm{DC}} = 2.9 \times 10^7$ m$^{-1}\Omega^{-1}$ is smaller compared to experimental DC conductivity of silver of $\sigma_{\mathrm{DC}} = 6.3 \times 10^7$ m$^{-1}\Omega^{-1}$ [151]. The difference will be discussed in section 3.4.3. As the frequency increases, the imaginary conductivity $\sigma_2(\omega)$ increases while the real part $\sigma_1(\omega)$ decreases and they eventually cross over near the frequency corresponding to the relaxation rate at $\omega = 1/\tau$. At even higher frequency, both $\sigma_1(\omega)$ and $\sigma_2(\omega)$ start to decrease with $\sigma_2(\omega) > \sigma_1(\omega)$ [59].

The penetration depth of an electromagnetic wave into the sample is described by the *skin*

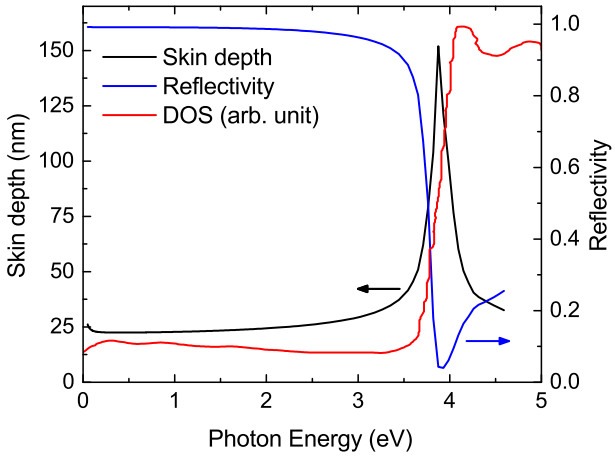

Figure 3.10: Skin depth $\delta_0(\omega)$ remains nearly constant at 25 ± 5 nm throughout the IR to visible range, then peaks at ~ 3.8 eV due to the interband transition. Derived reflectivity (blue). Density of state (DOS) from photoemission (red) [182].

depth δ_0, which is defined as the distance at which the electric field amplitude decays to $1/e$ of the incoming field amplitude. The skin depth relates to $\kappa(\omega)$ as $\delta_0(\omega) = c/\omega\kappa(\omega)$. Fig. 3.10 shows the derived frequency dependence of $\delta_0(\omega)$. The skin depth remains nearly constant at 25 ± 5 nm in the IR, which is due to $\kappa \propto 1/\omega$ in this spectral range. The skin depth peaks at the interband transition near 3.8 eV, where our assumption of bulklike film may fail. The peak of skin depth corresponds to a sharp minimum in κ, which results from a particular way the dielectric function associated with the interband transitions adds to the dielectric function of the Drude free electrons (conduction electrons) in the vicinity of interband transition [214].

3.3.3 Extended Drude model analysis

While the Drude model provides a good description of the dielectric function data across the mid-IR spectral range, a noticeable deviation between the direct inverted dielectric function ϵ_2 and the Drude model prediction is seen for energies below 0.1 eV. The smaller experimental values for ϵ_2 would suggest an increase in τ with decreasing frequency.

Using the extended Drude model, the frequency dependence of $\tau^{-1}(\omega)$ can readily be calculated from Eq. 3.7 with an input of $\epsilon_\infty = 5$ for silver. At low frequency $\epsilon_1 \gg \epsilon_\infty$, so the exact value

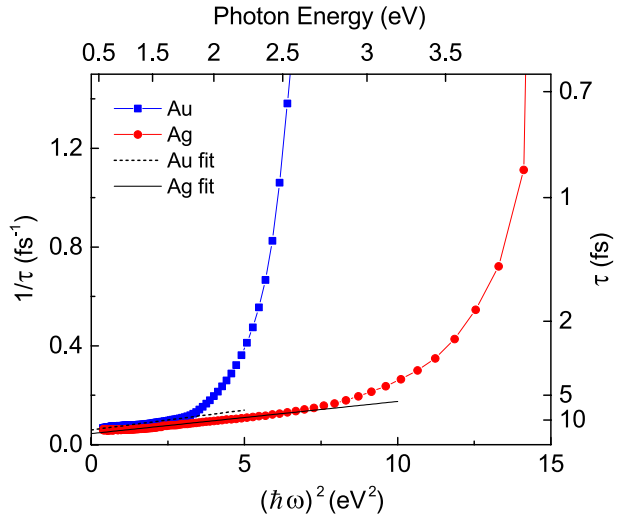

Figure 3.11: Frequency dependence of $\tau^{-1}(\omega)$ from extended Drude analysis. The linear relation below the interband transition agrees with Fermi liquid theory, $1/\tau = a + b(\hbar\omega)^2$, with $a = 0.045$ fs^{-1}, $b = 0.065$ eV^{-2}fs^{-1} for silver, and $a = 0.06$ fs^{-1}, $b = 0.08$ eV^{-2}fs^{-1} for gold, respectively. Extrapolating to zero frequency with $\tau = 22$ fs for silver and $\tau = 16$ fs for gold.

of ϵ_∞ does not significantly affect the resulting $\tau^{-1}(\omega)$. The frequency dependence of $\omega_p(\omega)$ can also be derived [4, 229], but we do not analyse it here.

Due to electron-electron interactions, a quadratic frequency dependence of $1/\tau$ is predicted by the Fermi liquid theory with $1/\tau = a + b(\hbar\omega)^2$ [185, 229]. Fig. 3.11 shows the frequency dependent $\tau^{-1}(\omega)$ from extended Drude analysis plotted against $(\hbar\omega)^2$. The observed linear relation below the interband transition seems to support the predicted quadratic frequency dependence of $1/\tau(\omega)$. Based on a fit with $a = 0.045$ fs^{-1} and $b = 0.065$ eV^{-2}fs^{-1} (solid line), an extrapolation to zero frequency implies a DC value of $\tau = 22$ fs for silver. Similarly, an extended Drude analysis for gold shows a quadratic frequency dependence of $1/\tau$ below the interband transition. A linear fit in Fig. 3.11 gives $a = 0.06$ fs^{-1}, $b = 0.08$ eV^{-2}fs^{-1}, with extrapolated $\tau = 16$ fs at zero frequency. This value can be compared with $\tau = 13 \pm 3$ fs from the Drude analysis [180].

With closer inspection of low frequency range of 0.05 – 0.1 eV, a frequency dependent trend of τ^{-1} different than quadratic is observed. Fig. 3.12 shows the frequency dependence of τ applying the extended Drude analysis in the range of 0.05 – 0.6 eV. τ for silver from this work is shown in red, and τ for gold from our previous work in blue [180]. The dashed and dot-dashed line is a fit to

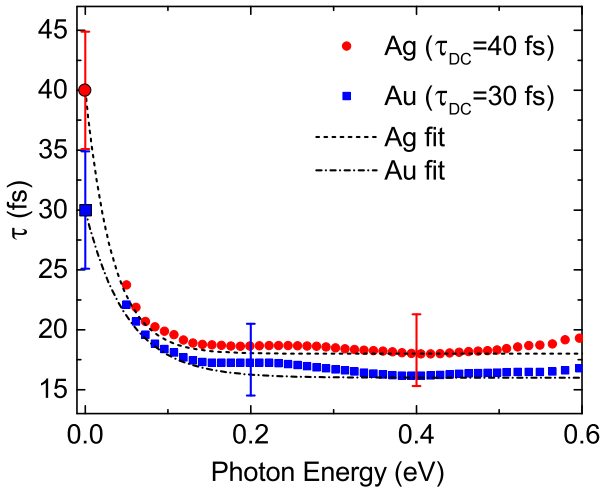

Figure 3.12: Frequency dependence of $\tau(\omega)$ in the low energy IR range for silver (red dot) and gold (blue dot). The fits are a simple exponential connecting to the zero-frequency value of τ calculated from DC conductivity (squares) [151]. Note, however, that increase in $\tau(\omega)$ below 0.1 eV is within our instrumental error.

a simple empirical exponential function with connection to the DC value (electrical relaxation time deduced from DC conductivity), for silver and gold respectively [60, 61, 151]. In this plot, both τ of silver and gold indicate an exponential increase towards DC frequency, different and more rapid than the quadratic frequency dependence of $1/\tau$ from Fermi liquid theory.

3.4 Discussion

3.4.1 Comparison of Drude parameters with literature values

Our derived Drude parameters are $\hbar\omega_p = 8.9 \pm 0.2$ eV, $\epsilon_\infty = 5 \pm 2$, and $\tau = 17 \pm 3$ fs. For comparison, the range of literature values are $\hbar\omega_p = 7 - 9$ eV, $\epsilon_\infty = 1 - 10$, and $\tau = 5 - 40$ fs. The differences can be due to both instrumental errors and/or sample types and preparation procedures [180, 219].

For the two previous experiments with longer τ than our measurement [112, 18], some issues have already been noted above. Data from Johnson and Christy have an uncertainty of $\sim 40\%$ for n in the 0.6 – 3 eV spectral range when n is small [112]. The resulting relaxation time has a

large uncertainty with $\tau = 31 \pm 12$ fs. In addition, the data directly extracted from reflection and transmission is not necessarily Kramers-Kronig consistent. Bennett and Bennett simply assumed $\tau = 36$ fs to complement their normal reflectance measurement for calculating the dielectric function in the 3 – 30 μm wavelength range [18]. Of the other previous measurements, data from Dold and Mecke [55] was pointed out by Lynch and Hunter [145] to have erroneously low values for k resulting in too large values of ϵ_1. The good agreement in ϵ_2 and the difference in ϵ_1 between their data and ours further imply the data from Dold and Mecke are not Kramers-Kronig consistent.

In previous experiments as well as in our measurements on three different samples, larger relative variations in Vis/UV are observed in comparison to the IR region. Our derived reflectivity from the dielectric function agrees well with the behavior expected from density of state (DOS) measurements from photoemission [182], as shown in Fig. 3.10. The reflectivity derived from our data inversely correlates to the DOS, with good agreement on the position and slope near the interband transition.

It is in principle possible to compare the Drude parameters with results from surface plasmon resonance (SPR) lifetime measurement. τ relates to the non-radiative damping of a localized SPR, and the surface plasmon propagating length. However, SPR lifetime can be influenced by radiative damping and surface scattering, and in most nano-particles studies, the SPR resonances spectrally overlap with interband transitions [161, 101, 25, 28]. It is worth noting, however, that our measured $\tau = 17 \pm 3$ fs is consistent with the longest value of $\tau = 13$ fs based on plasmonic resonance line width of a silver nano-particle at room temperature [161, 101, 25].

3.4.2 Interband effects

As mentioned in section 3.3.1, the experimental dielectric function deviates from the Drude behavior in the Vis/UV region due to the direct interband transition from d to sp band. The electronic band structure of silver for the related d to sp band transition is shown in Fig. 3.13c. The eleven unfilled electrons of silver ($[\mathrm{Kr}]4d^{10}5d^{1}$) forms six bands, which are hybridized into two groups. Five of them lie in a narrow range of energies from 2 eV to 5 eV below the Fermi energy

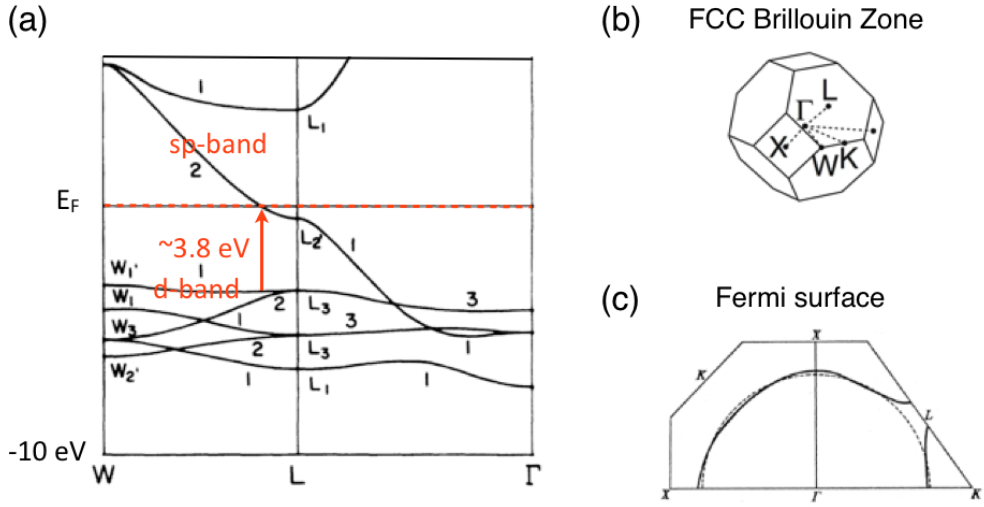

Figure 3.13: (a)Band structure of silver and interband transition from d band to sp band with onset energy of about 3.8 eV. (b) The first Brillouin zone of a FCC crystal. (c) The Fermi surface of silver resembles the free electron Fermi sphere. Figure after [196, 73].

and are referred as the d-band, while the sixth one spans a wide energy range for different k-vectors and are referred as the sp-band. The reciprocal space of the FCC crystal structure of silver is shown in (a) labelled with symmetric points. The Fermi surface for silver is shown in (b). It is similar to the free electron Fermi sphere of a single electron FCC crystal, except at the $\langle 111 \rangle$ direction where the L-neck connects across the zone faces [13].

For energies below the onset of the interband transition, ϵ_∞ can be adjusted to partially account for the interband effect. To better describe the interband influence on the dielectric function, empirically parametrized Gaussian or Lorentzian resonances can be added into the Drude model with $\epsilon(\omega) = \epsilon_{\text{Drude}} + \epsilon_{\text{d}}(\omega)$ [193, 194]. The interband contribution $\epsilon_{\text{d}}(\omega)$ can be well described by damped harmonic oscillators to parametrize the response of the d-electrons [193]. However, this approach does not add any additional physical insight, thus such analysis is not performed here.

3.4.3 Deviation from Drude behavior

As shown in section 3.3.3, despite the general agreement between experimental results and the extended Drude model, the observed rapid rise of τ at energies below 0.1 eV cannot fully

be described by the Fermi-liquid theory. The relaxation time is related to the DC conductivity in the Drude model through $\sigma(0) = \epsilon_0\omega_p^2/\Gamma$. This would imply a DC conductivity of 3.6×10^7 $\mathrm{m}^{-1}\Omega^{-1}$ for $\tau = 22$ fs and $\omega_p = 9$ eV — a factor of 2 smaller than the electrically measured DC conductivity of 6.3×10^7 $\mathrm{m}^{-1}\Omega^{-1}$ [215, 186, 151]. Similar discrepancies between τ from optical measurements and DC resistivity measurements have been noted previously but not yet reconciled [61, 216, 60, 185, 91]. While our results suggest a connection between the IR and DC due to a rapid increase of τ below 0.1 eV, we would like to emphasis that the variation in τ below 0.1 eV is within the systematic uncertainty of our instrument when operating at the low frequency limit.

The relaxation time τ is determined by electron damping. For an ideal silver sample free from defects and impurities at a temperature of $T = 0$ K the damping goes to zero, thus $\tau \to \infty$ [185, 140]. However, for a real sample at room temperature various intrinsic and extrinsic effects result in a finite τ. The relaxation rate τ^{-1}, as the summed contribution from intrinsic electron-electron and electron-phonon, and extrinsic electron-surface/grain boundary scattering, can be expressed as [140, 185]

$$\tau^{-1} = \tau_{\mathrm{e-ph}}^{-1} + \tau_{\mathrm{e-e}}^{-1} + \tau_{\mathrm{S}}^{-1}. \tag{3.13}$$

$\tau_{\mathrm{e-ph}}^{-1}$ is the dominating factor at room temperature and is a result of scattering an electron by simultaneously absorbing and emitting a phonon [100, 30, 115, 185]. At frequencies much higher than the Debye frequency (~ 0.01 eV), the interaction averages over all the phonon modes resulting in a constant effective collision time with negligible frequency dependence [200, 5]. The contribution from electron-electron scattering has been derived as [132, 185]

$$\tau_{\mathrm{e-e}}^{-1} = \frac{\pi^3 \Sigma \Delta}{12\hbar E_F}\left[(k_B T)^2 + \left(\frac{\hbar\omega}{2\pi}\right)^2\right], \tag{3.14}$$

with Fermi energy E_F, averaged scattering probability over the Fermi-sphere Σ, and the fractional umklapp scattering Δ. $\tau_{\mathrm{e-e}}^{-1}$ has a quadratic frequency dependent term. $\tau_{\mathrm{e-e}}^{-1}$ is also quadratically temperature dependent, but the temperature dependence of electron-electron scattering is negligible compared to electron-phonon scattering at room temperature [185, 132]. The interface scattering rate τ_{S}^{-1} is related to grain boundaries and surface roughness, and is assumed to be directly propor-

tional to the surface area for nano-particles. One therefore expects an overall quadratic frequency dependent $\tau^{-1}(\omega)$. However, the quadratic frequency dependence of $\tau^{-1}(\omega)$ can easily be obscured at finite temperature. Measurements as a function of temperature and purity, and with controlled sample morphology are needed to discriminate the various mechanisms responsible for damping [140, 219].

A reduction of relaxation rate at low temperature has been observed measuring the surface plasmon lifetimes of gold nano-particles in agreement with theory [140]. However, the frequency dependence was not studied.

3.4.4 Grain size and other finite size effects

Recently, effects of sample morphology have been studied systematically with spectroscopic ellipsometry on gold in the IR spectral range [219]. By estimating the grain size from AFM measurements, the authors established a linear relation of increasing τ with larger grain size. Their measured relaxation rate $\Gamma = 261$ cm^{-1} on the sample with largest gain size of 170 nm (300 nm thick gold film on mica) corresponds to $\tau = 20$ fs. By linearly extrapolating their measurements on different samples to infinite grain size, the authors suggest $\tau = 26$ fs for gold at room temperature. This value would be close to the corresponding τ from DC conductivity of $\sim$ 30 fs as shown in Fig. 3.12, yet neglects the effects of electron-electron, and electron-phonon scattering at finite temperature. At grain size of 170 nm and beyond, the relaxation time should no longer be grain size limited as the mean free path of electron for gold at room temperature is about 30 nm. Thus simple linear extrapolation of the relaxation time with grain size may not be valid. Variation of τ with grain size in ref. [219] for sizes above 60 nm could also be due to differences in impurity/defect scattering due to different preparation procedures for their commercial and self-prepared samples.

We note that ref. [219] seems to underestimate the instrumental errors. As the authors used the same type of instruments as ours, we can assign an instrumental error of 3 fs to the relaxation time τ based on our calibration. The 3 fs can be comparable to the differences between samples. Nevertheless the generally large values of 16 – 20 fs in ref. [219] compared to our $\tau = 14 \pm 4$ fs

measured for single crystal gold and $\tau = 13 \pm 3$ fs for TS gold with average grain size of 120 ± 30 nm [180], would indicate higher impurity/defect scattering for our samples.

To assess sample morphology influence on silver, we compare TS silver to TS gold with similar grain size. A re-measurement on four TS gold samples on Si substrate shows good agreement with our previous TS gold measurements [180], as well as with measurements of a 200 nm thick gold film on a polished silicon $\langle 100 \rangle$ surface in ref. [219]. However, larger sample-to-sample variations of dielectric function ϵ_2 are observed for silver. In addition, by measuring at different times of an interval of from one day up to a week after stripping, we observe the dielectric function of TS gold varies within the uncertainty of the instruments, while similar measurements on silver show significant variations with a trend of decreasing τ over time. This suggests that the dielectric function of silver is more sensitive to variations in morphology than gold. Morphology influences on silver have also been observed with increased τ on smoother silver surface [184, 183]. Measurements on single crystal result in a larger τ than on polycrystalline sample [183]. As our measurements have been performed under ambient conditions, surface oxidation is unavoidable despite great care on handling the sample. Despite numerous studies, a quantitative correlation between sample extrinsic effects and τ has not yet been performed.

3.4.5 Conclusion

In summary, we measured dielectric function of optically thick silver film over a broad spectral range from 0.05 to 4.14 eV. Data show an overall good agreement of measured dielectric function to the Drude model. Deviation at low energies below 0.1 eV is partially explained by Fermi-liquid theory with frequency dependent Drude parameters. Sample-to-sample variations suggest the dielectric function of silver is sensitive to environmental conditions and influenced by extrinsic effects. We have improved accuracy and provided a broader spectral range compared to historical measurements, and believe our measured dielectric function is representative of pure bulk silver used in typical experimental thin film applications. Further verification of the improvement for practical use can be tested for silver photonics applications with models based on our values. However, given

the undetermined extrinsic effects more investigation is needed especially for energy range between DC to 0.1 eV. To exclude unquantified contribution from grain boundaries, other possible surface morphology effects, and surface impurity scattering, future experiments with samples of single crystal surfaces under ultrahigh vacuum and at variable temperature condition are highly desirable to arrive at a more microscopic understanding of the frequency dependence of the relaxation process in metals. The possibility of different relaxation time over the Fermi surface needs to be explored by studying different surface orientations $\langle 111 \rangle$ and $\langle 110 \rangle$ and $\langle 100 \rangle$. Finally, there may be a need for more direct methods, such as energy and momentum resolved photoemission, in combination with ellipsometry to probe the underlying electronic interactions of silver.

Chapter 4

Experimental implementation of infrared *s*-SNOM

By combining optical spectroscopy with atomic force microscopy (AFM), *scattering*-type scanning near-field optical microscopy (*s*-SNOM) enables the optical spectroscopy to achieve nanometer optical spatial resolution. This is especially desirable for infrared with its spatial resolution of a few μm limited by diffraction. Infrared spectroscopy is very powerful because its photon energy corresponds to the energy range of vibrational resonance of molecules, which is specific to different chemical bonds in the so called "fingerprint" region. Infrared can also probe the Drude free electron response of metals, which is instrumental for studying metal-insulator transitions in correlated electron materials.

In this chapter, I cover the fundamentals of the *s*-SNOM technique and address how the amplitude and phase of the measured near-field signal connects to the local material properties. Measured near-field spectrum on organics are compared to conventional far-field Fourier transform infrared spectroscopy (FTIR) spectrum, and the difference in spectrum due to spectral-phase approximation and near-field coupling effects are discussed. In addition as a demonstration of general applicability of our *s*-SNOM approach, I also measured surface plasmon polariton on graphene, surface phonon polariton on hBN, and chemical mapping of membrane protein of bacteriorhodopsin.

4.1 Setup of *s*-SNOM

A typical experimental implementation of a *s*-SNOM setup is illustrated in Fig. 4.1a, with the schematics of the interferometric detection shown in (b). Due to the similarity in the optical

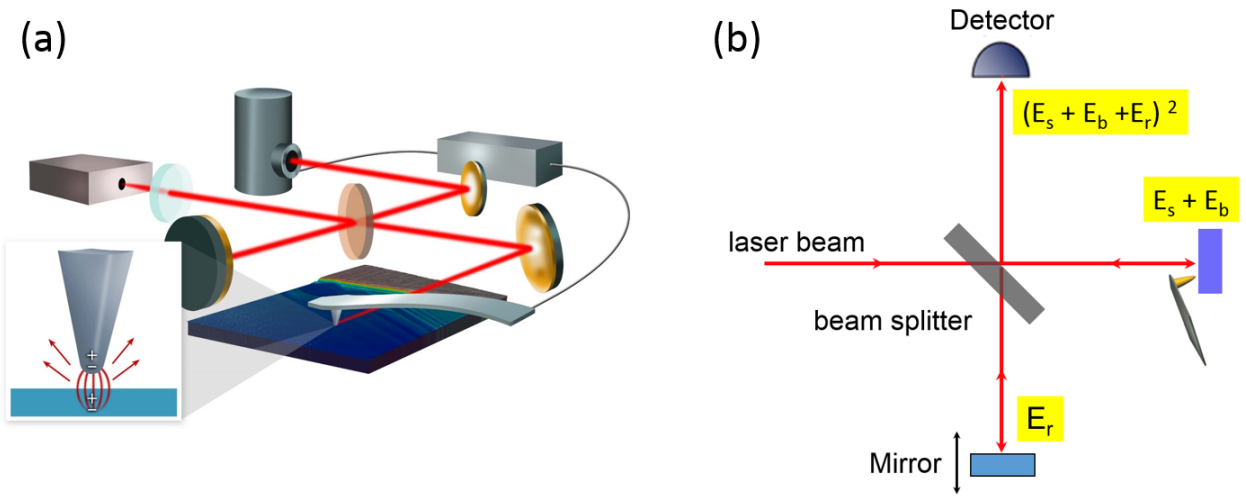

Figure 4.1: (a) Schematics of a typical *s*-SNOM setup, with an atomic force microscope (AFM) for mediating near-field interaction and a Michelson interferometer for interferometric detection. Light propagating in free space is focused to the tip apex of AFM by a parabolic mirror. Scattered light from the tip is collected by the same parabolic mirror. Inset shows the tip-sample interaction. (b) Principle of interferometric detections in *s*-SNOM. The scattered light from the tip is collected by the same optics, and recombined with the reflected reference beam in the beamsplitter for coherent amplification and phase-resolved interferometric detection.

detection scheme, *s*-SNOM can been seen as a natural extension of FTIR, thus inheriting the full spectroscopic capability. The setup of *s*-SNOM consists of two parts, a Michelson interferometer and an AFM. The interferometer arm with the AFM and the sample focuses the incoming light to the tip and collect the scattered light; the other arm, called the reference arm, consists of a reflective mirror to coherently amplify the weak scattered light from the tip and for interferometric detection to resolve the phase.

As already explained in chapter 2.6, the tip scattered light contains both the near-field signal E_s and unspecific far-field background from the tip shaft and the sample E_b. In order to suppress the background, the scattered light is modulated by the AFM tip oscillation at its mechanical resonance frequency Ω. Despite the modulation, the coherent nature of the incidence laser light makes the photons emitting from the localized tip-sample region interference with the far-field background. Thus, the light on the detector is a time averaged intensity of $I \sim |E_s + E_b|^2 = |E_s|^2 + |E_b|^2 + 2|E_s E_b| \cos(\phi_s - \phi_b)$, with the term $|E_s E_b| \cos(\phi_s - \phi_b)$ due to the multiplicative

far-field background, and ϕ_s and ϕ_b the phase of the near-field signal and background, respectively. As the far-field background E_b is randomly scattered from the whole illuminated area, the phase ϕ_b is generally uncontrolled. To fully characterize the near-field signal and suppress the multiplicative far-field background, interferometric detection with a known reference beam is needed to determine both the amplitude and phase of the near-field signal. By adding the reference term E_r as shown in Fig. 4.1b, the intensity at the detector becomes

$$\begin{aligned} I &\sim |E_s + E_b + E_r|^2 \\ &= |E_s|^2 + |E_b|^2 + |E_r|^2 \\ &+ 2|E_s E_b| \cos(\phi_s - \phi_b) + 2|E_s E_r| \cos(\phi_s - \phi_r) + 2|E_b E_r| \cos(\phi_b - \phi_r) \end{aligned} \tag{4.1}$$

with ϕ_r the phase of the reference arm.

After demodulating the detected signal at higher harmonics of the AFM tip oscillation frequency (i.e., 2Ω and 3Ω), only the terms being modulated at 2Ω or 3Ω remain, namely $2|E_s E_b| \cos(\phi_s - \phi_b)$ and $2|E_s E_r| \cos(\phi_s - \phi_r)$ in Eq. 4.1. Typically, the third harmonic signal after demodulation $I_{3\Omega}$ is chosen to represent the near-field signal, with $I_{3\Omega}$ being

$$I_{3\Omega} = 2|E_s E_b| \cos(\phi_s - \phi_b) + 2|E_s E_r| \cos(\phi_s - \phi_r). \tag{4.2}$$

The near-field amplitude $|E_s|$ and phase ϕ_s can be obtained from the second term $2|E_s E_r| \cos(\phi_s - \phi_r)$ by controlling the reference phase ϕ_r. The first term $2|E_s E_b| \cos(\phi_s - \phi_b)$ is due to the multiplicative far-field background. Various phase modulation methods have been developed to suppress the background term and to extract the amplitude and phase [202, 54, 175].

4.2 Near-field spectroscopy

In Eq. 4.2, the $I_{3\Omega}$ is a sinusoidal function (*interferogram*) with respect to the reference phase ϕ_r. Fig. 4.2a shows two such interferograms taken on locations of two different materials by linearly moving the reference mirror (linearly increasing the reference phase). The blue curve is an interferogram taken on a material of interest at position A, while the red curve is taken at

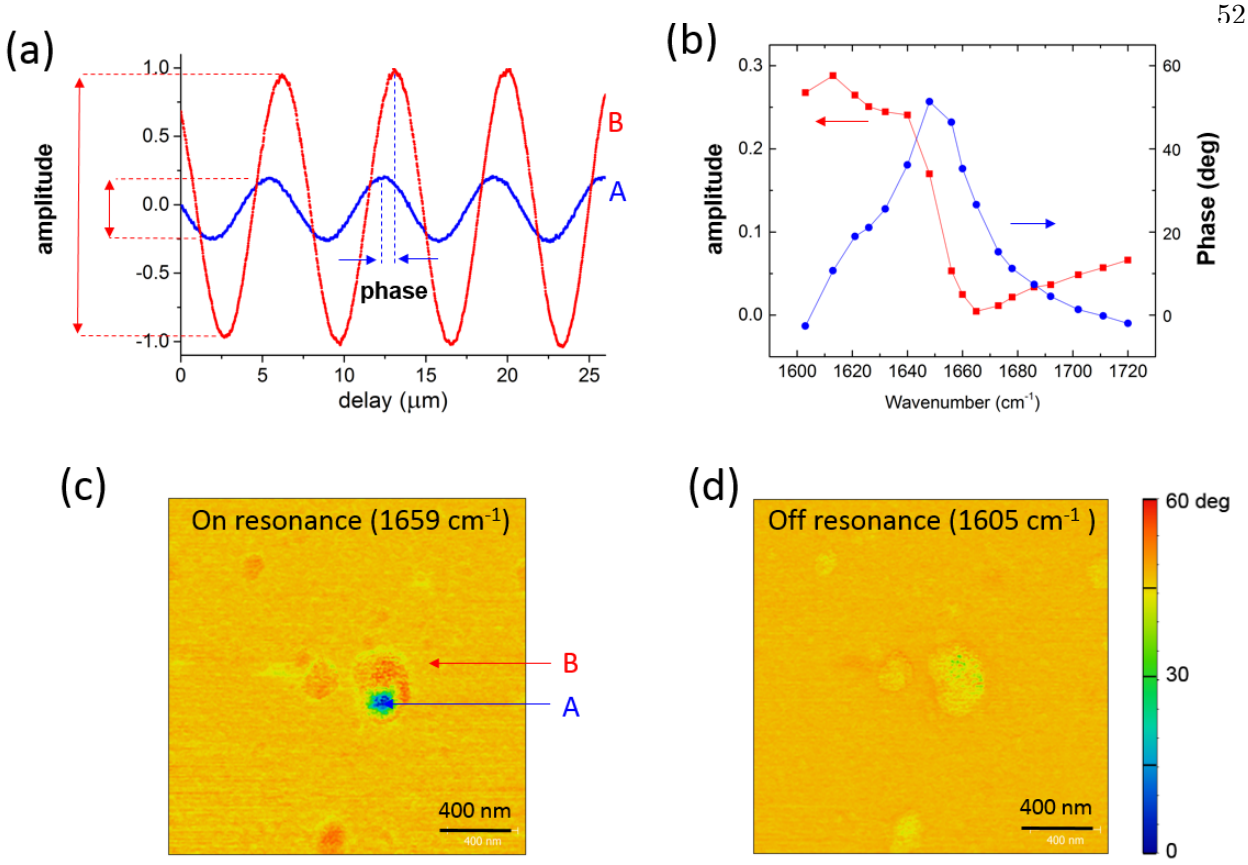

Figure 4.2: (a) Interferometric detected near-field signal forms a sinusoidal wave as the reference mirror linearly translated in the Michelson interferometer in Fig. 4.1. The amplitude and phase delay of the interferogram carries spectroscopic information of the local sample material and changes with the local material. To extract the spectroscopic information, the signal on a point of interest needs to be normalized to a reference signal obtained on a known substrate with flat spectroscopic response (typically gold or silicon). The blue and red curves are taken at two locations on and off the feature of interest in (c), which are labeled as point A and point B respectively. The amplitude ratio and the phase difference of the two sinusoidal wave contains the spectroscopic information of the sample, and varies with wavelength. As the wavelength changes, the amplitude ratio and the phase difference varies. (b) Resulting spectrum of amplitude and phase across an amide I band resonance of the organic defect sample. The amplitude corresponds to the real part of dielectric function ϵ_1, while the phase corresponds to the imaginary part of dielectric function ϵ_2. The exact relation of the amplitude and phase spectrum to the dielectric function of the underlying material are still under research. Near-field phase image for the organic defect on gold substrate on resonance at 1659 cm^{-1} (c) and off resonance at 1605 cm^{-1} (d).

a gold substrate at position B as a reference. Although being constant, in general the absolute amplitude $|E_r|$ and phase ϕ_r of the reference beam in Eq. 4.2 is undetermined. As a result, to determine the scattered light from a point of interest (A), a reference interferogram from a known

material (B) need to be collected and subtracted from the interferogram A. The amplitude ratio of the interferograms A and B represents the relative amplitude of the scattered light $|E_s|$, while the phase difference of interferograms A and B represents the relative phase of the scattered light ϕ_s.

With a tunable continuous-wave (CW) laser, the amplitude and phase of a sample at one wavelength can be extracted from interferograms as mentioned above. By stepping the laser wavelength across resonances, a spectrum of both amplitude and phase can be obtained. Fig. 4.2b shows the amplitude (red) and phase (blue) spectrum of an organic defect on gold film with its resonance at around 1660 cm^{-1}. The phase spectrum shows an absorptive line shape resembling the conventional FTIR spectrum. It corresponds to the extinction coefficient (κ) or the imaginary part of the dielectric function (ϵ_2). The amplitude spectrum shows a dispersive line shape which corresponds to the refractive index (n) or the real part of the dielectric function (ϵ_1). The amplitude and phase spectrum can thus be used as approximation to complex dielectric function of $\epsilon(\omega) = \epsilon_1(\omega) + i\epsilon_2(\omega)$. This approximation is typically valid for weak resonances such as molecular vibrational resonances, however it can fail for collective resonances such as surface phonon or surface plasmon polaritons resonances [160].

The quantitative correspondence of the amplitude and phase spectra to the frequency dependence of the dielectric function $\epsilon(\omega) = \epsilon_1(\omega) + i\epsilon_2(\omega)$ is still under investigation, with current experimental and theoretical results indicating a unsystematic variation of the amplitude and phase spectra due to sample thickness and tip geometry [160, 150, 85]. The amplitude and phase can also be transformed to real and imaginary part as in a coordinate transformation. Recent studies show the imaginary part of the s-SNOM signal corresponds better to the dielectric function of the sample than the phase. More systematic studies are needed to quantitatively determine the spectral correspondence of the near-field signal and the dielectric function of the sample material.

4.3 Understanding the near-field spectrum

As derived in chapter 2.6.1, the dipole model predicts that the near-field signal E_s is proportional to the effective polarizability α_{eff}, i.e., $E_s = \alpha_{\text{eff}} E_0$, with

$$\alpha_{\text{eff}} = \alpha \left[1 - \frac{\alpha\beta}{16\pi\epsilon_0 (R+h)^3} \right]^{-1}. \tag{4.3}$$

Here α is the polarizability of the tip itself, R is the tip radius, h the tip and sample separation, and β the reflection coefficient. Only $\beta = (\epsilon_s - 1)/(\epsilon_s + 1)$ contains the information of sample dielectric function $\epsilon_s = \epsilon_1 + i\epsilon_2$. With some algebra, β can be rewritten to separate its real and imaginary part as

$$\begin{aligned} \beta &= \frac{\epsilon_1 + i\epsilon_2 - 1}{\epsilon_1 + i\epsilon_2 + 1} \\ &= \frac{(\epsilon_1 - 1 + i\epsilon_2)(\epsilon_1 + 1 - i\epsilon_2)}{(\epsilon_1 + 1 + i\epsilon_2)(\epsilon_1 + 1 - i\epsilon_2)} \\ &= \frac{|\epsilon_s|^2 - 1 + i2\epsilon_2}{|\epsilon_s + 1|^2}. \end{aligned} \tag{4.4}$$

So the imaginary part of β is proportional to the imaginary part of the sample dielectric function ϵ_2, or explicitly

$$\text{Im}(\beta) = \frac{2\epsilon_2}{|\epsilon_s + 1|^2}. \tag{4.5}$$

Under typical experimental condition for weak resonance material, the denominator in Eq. 4.3 is close to 1 and can be approximated to the first term of the Tylor expansion series [85, 103]

$$\begin{aligned} \alpha_{\text{eff}} &= \alpha \left[1 - \frac{\alpha\beta}{16\pi\epsilon_0 (R+d)^3} \right]^{-1} \\ &\approx \alpha \left[1 + \frac{\alpha\beta}{16\pi\epsilon_0 (R+d)^3} \right]. \end{aligned} \tag{4.6}$$

With Eq. 4.6, we can derive the material dependence of the near-field signal E_s. The complex valued near-field signal E_s is $E_s = \mathbf{Re}(E_s) + \mathbf{Im}(E_s) = |E_s| \exp(i\phi_s)$. Combining Eq. 4.5 and 4.6, we get $\mathbf{Im}(E_s) \propto \mathbf{Im}(\beta) \propto \mathbf{Im}(\epsilon_s)$, i.e., the imaginary part of the near-field signal corresponds to the imaginary part of the sample dielectric function.

Typical *s*-SNOM experiments are implemented in such a way that the near-field amplitude $|E_s|$ and phase ϕ_s are measured instead of the real $\mathbf{Re}(E_s)$ and imaginary part $\mathbf{Im}(E_s)$. If $\mathbf{Im}(E_s) \ll \mathbf{Re}(E_s)$, then $\phi_s \propto \mathbf{Im}(E_s)$. This is the *spectral phase approximation*, which says the phase ϕ_s is proportional to the imaginary part of the dielectric function $\mathbf{Im}(\epsilon_s)$. The validity of this approximation is discussed below.

To study the relation between the near-field spectra and the dielectric function of the sample material, I start with a model material with a single Lorentzian resonance. The dielectric function of the sample material can be modelled as a harmonic oscillator with resonance frequency ω_0, line width γ, and coupling strength A, with

$$\epsilon(\omega) = 1 + \frac{A}{(\omega_0^2 - \omega^2) - i\omega\gamma} \tag{4.7}$$

By introducing a detuning frequency $\delta = \omega - \omega_0$, we can simplify Eq. 4.7 under the assumption of near resonance $\delta \ll \omega_0$ and low damping $\gamma \ll \omega_0$. Under these two approximations we have $\omega_0^2 - \omega^2 \approx -2\omega_0\delta$, and $\omega\gamma \approx \omega_0\gamma$, and Eq. 4.7 simplifies to

$$\epsilon(\delta) = 1 + \frac{A}{-2\omega_0\delta - i\omega_0\gamma} \tag{4.8}$$

$$= 1 - \frac{A}{2\omega_0}\frac{1}{\delta + i\gamma/2} \tag{4.9}$$

$$= 1 - \frac{A}{2\omega_0}\frac{\delta - i\gamma/2}{\delta^2 + (\gamma/2)^2}. \tag{4.10}$$

I further introduce a coupling coefficient

$$g \equiv \frac{A}{2\omega_0\gamma}, \tag{4.11}$$

with which Eq. 4.10 can be rewritten as

$$\epsilon(\delta) = 1 - g\gamma\frac{\delta - i\gamma/2}{\delta^2 + (\gamma/2)^2}. \tag{4.12}$$

Now the complex dielectric function becomes a Lorentzian function and traces an circle counter clockwise in the complex plane as the detuning frequency δ goes from $-\infty$ to $+\infty$ as shown in Fig. 4.3. The circle has a radius of g, and an offset of $(\epsilon_1, \epsilon_2) = (1, g)$ from the origin. Under this

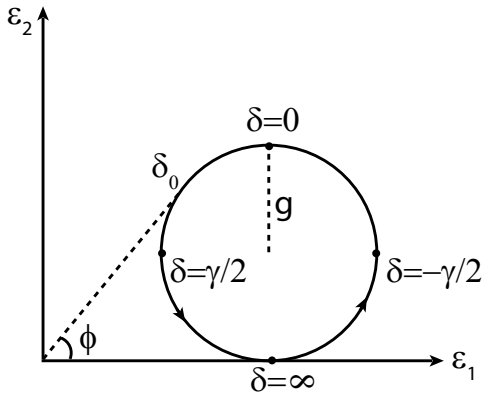

Figure 4.3: The dielectric function of a material across a resonance can be modeled as $\epsilon(\delta) = \epsilon_1 + i\epsilon_2 = 1 - g\gamma\frac{\delta - i\gamma/2}{\delta^2 + (\gamma/2)^2}$, where $\delta = \omega - \omega_0$ is the detuning frequency, γ the damping factor, and g is coupling coefficient. The dielectric function can be represented as a sphere in complex plane.

picture, the dielectric function can either be represented in Cartesian coordinate as $\epsilon = \epsilon_1 + i\epsilon_2$ or in polar coordinate as $\epsilon = A\exp(i\phi)$, with the phase ϕ defined as $\tan\phi = \epsilon_2/\epsilon_1$ as shown in Fig. 4.3. For $g < 1$, the circle stays in the right side of the complex plane with $\epsilon_1 > 0$. This region can be defined as the weak coupling region. In the strong coupling region with $g \geq 1$, ϵ_1 can be negative. Intuitively, as δ goes from negative to positive along the circle ϵ_2 goes across a resonance with its maximum at $\delta = 0$, i.e., the resonance of the material. The maximum and minimum ϵ_1 happens at $\delta = -\gamma/2$ and $\delta = \gamma/2$, respectively. For $g \ll 1$ the phase ϕ is proportional to ϵ_2, and can be used to approximate ϵ_2.

As δ increases from negative, ϕ gradually increases and reaches a maximum. The maximum point can be found by drawing a tangent line passing through the origin. This maximum point defined as δ_0 is located in between $\delta = 0$ and $\delta = \gamma/2$. Thus the resonance (maximum) of ϕ is not at the same resonance frequency of ϵ_2, but blue shifted. The amount of blue shift can be easily calculated from the graph with a resulting value $\delta_0 = g\gamma/2$. The blue shift δ_0 increases with g, with maximum shift of $\delta_0 = \gamma/2$ when $g = 1$. Since γ is the FWHM of the resonance, the maximum resonance frequency shift of ϕ relative to ϵ_2 is half the line width of the resonance.

Fig. 4.4 shows an example of blue shifts for different coupling coefficients $g = 0.5$ (a) and $g = 1$ (b), with fixed $\gamma = 20$ cm^{-1}. The imaginary part of dielectric function $\epsilon_2 = \mathrm{Im}(\epsilon)$ and phase

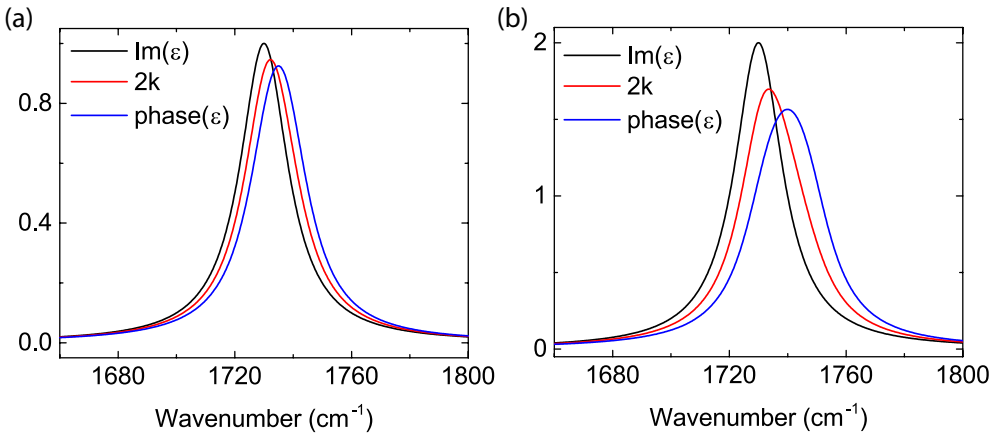

Figure 4.4: Comparing $\epsilon_2 = \mathrm{Im}(\epsilon)$, refractive index k, and phase of ϵ (ϕ), assuming a Lorentzian oscillator with resonance at 1730 cm^{-1}, $\gamma = 20$ cm^{-1}, and coupling coefficient g of different values. The resonance frequency of ϕ is blue shifted to $2k$, which is also blue shifted to $\mathrm{Im}(\epsilon)$. (a) For coupling strength $g = 0.5$, ϕ is blue shifted by 5 cm^{-1} with respect to ϵ_2. (b) For $g = 1$, the phase is blue shifted by 10 cm^{-1} with respect to ϵ_2.

$\phi = \arctan(\epsilon_2/\epsilon_1)$ are shown in black and blue, respectively. In addition, the extinction coefficient $\kappa = \mathrm{Im}(\sqrt{\epsilon})$ after multiply by a factor of two is plotted together in red. With $\gamma = 0.5$, ϕ is blue shifted 3 cm^{-1} relative to 2κ, and 5 cm^{-1} relative to ϵ_2; $\gamma = 1$ gives a shift of 10 cm^{-1} relative to ϵ_2, and 6 cm^{-1} relative to 2κ.

To get a sense of coupling coefficient for a real material, let us take a look at two common organic materials – Poly(methyl methacrylate) (PMMA) and Polytetrafluoroethylene (PTFE). Fig. 4.5 shows the dielectric function of PMMA (a) and PTFE (b) across their prominent resonances. PMMA has a carbonyl resonance at around 1729 cm^{-1}, and the real and imaginary part of the dielectric function from ellipsometry measurements are shown in black and blue dotted lines, respectively. The solid lines are Lorentzian oscillator fit to the experimental dielectric function with a resulting coupling coefficient of $g = 0.6$. For PTFE, its characteristic C-F stretch vibration mode has two resonances at $\omega = 1160$ cm^{-1} (symmetric stretch) and $\omega = 1220$ cm^{-1} (antisymmetric stretch), respectively. The imaginary part of the dielectric function of PTFE at the range of interest is shown as dotted blue line in Fig. 4.5. The two resonances can be simulated as two

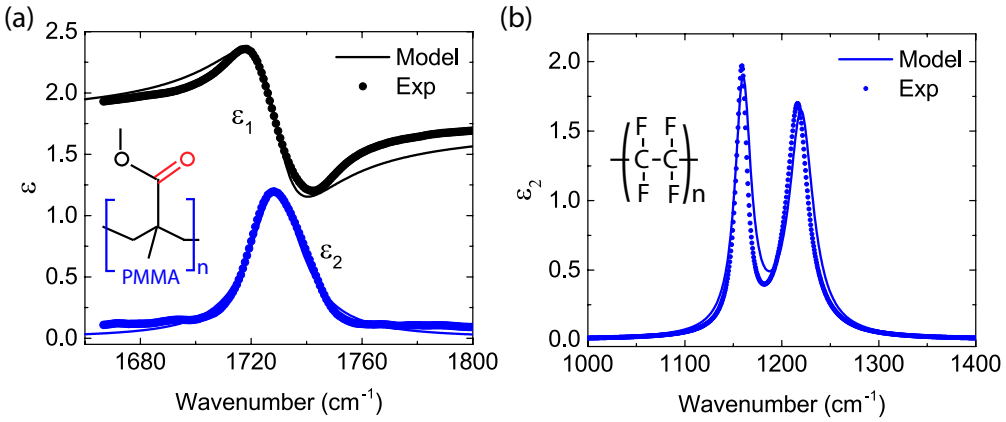

Figure 4.5: Dielectric function of PMMA and PTFE. (a) The dielectric function of PMMA across the carbonyl resonance with experimental value in dotted line and Lorentzian model in solid line. The coupling coefficient $g = 0.6$ is obtained from the Lorentzian fit to the experimental value. (b) Imaginary part of the dielectric function of PTFE with experimental value and Lorentzian model in dotted and solid line, respectively. The two peaks are symmetric and antisymmetric C-F stretch modes of PTFE, which can be simulated as two Lorentzian oscillators, with $\omega_1 = 1160$ cm^{-1}, $\gamma_1 = 20$ cm^{-1}, $g_1 = 0.9$, and $\omega_2 = 1220$ cm^{-1}, $\gamma_2 = 30$ cm^{-1}, $g_2 = 0.8$.

Lorentzian oscillators

$$\epsilon(\omega) = 1 + g_1 \frac{2\gamma_1\omega_1}{\omega_1^2 - \omega^2 - i\omega\gamma_1} + g_2 \frac{2\gamma_2\omega_2}{\omega_2^2 - \omega^2 - i\omega\gamma_2}, \tag{4.13}$$

with $\omega_1 = 1160$ cm^{-1}, $\gamma_1 = 20$ cm^{-1}, $g_1 = 0.9$, and $\omega_2 = 1220$ cm^{-1}, $\gamma_2 = 30$ cm^{-1}, $g_2 = 0.8$. So the symmetric stretch and antisymmetric stretch have coupling coefficients of $g_1 = 0.9$ and $g_2 = 0.8$, respectively. C-F in PTFE and carbonyl in PMMA are very strong resonances in organics, but the coupling coefficients are still smaller than 1. We can conclude that vibrational resonances of most organic materials belong to weak coupling under which the spectral phase approximation can be used.

To confirm the modeling, we compare experimental *s*-SNOM spectra to sample dielectric functions measured by ellipsometry. 300 nm thick mircotomed film of 3 μm diameter PMMA beads embedded in epoxy on ZnS substrate is measured by *s*-SNOM to extract the complex optical dielectric function of PMMA across the carbonyl resonance at $\omega = 1729$ cm^{-1}. A large disk of thick PMMA is chosen here to represent a bulk-like PMMA. Continuous-wave infrared light tunable from $\omega = 1660$ cm^{-1} to 1800 cm^{-1} with a line width < 1 cm^{-1} is emitted from a quantum cascade laser

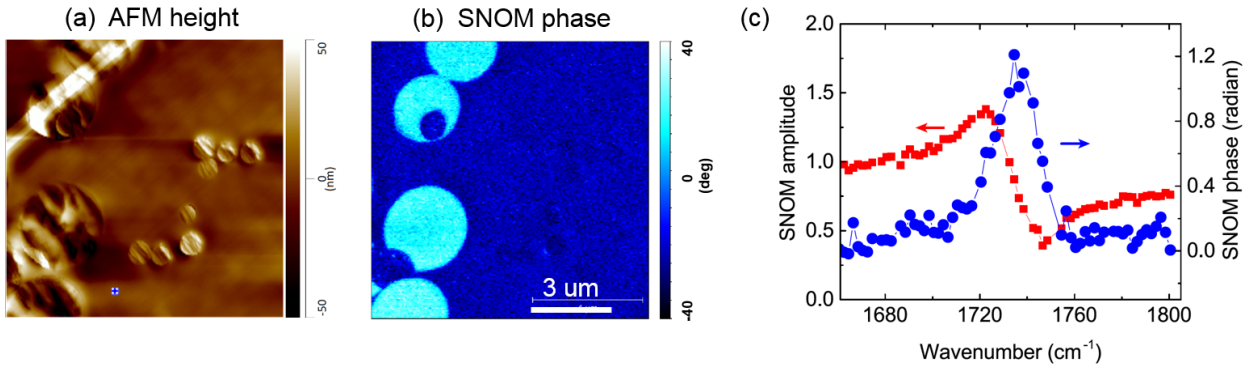

Figure 4.6: *s*-SNOM spectrum of PMMA taken on PMMA disk embedded in epoxy. (a) AFM height image on PMMA/epoxy sample; (b) *s*-SNOM phase image on resonance at 1729 cm^{-1}. The bright disk is PMMA, while other topographic features in the height image in (a) do not show phase contrast. (c) *s*-SNOM amplitude (red) and phase (blue) spectrum taken on PMMA disk. *s*-SNOM amplitude spectrum is dispersive and phase spectrum is absorptive.

(QCL, Daylight solutions). Fig. 4.6 (a) shows the topography of a sample region with a PMMA bead together with other topographic features. The PMMA bead can be clearly identified with a big phase shift relative to the epoxy matrix from the *s*-SNOM phase image taken on resonance at $\omega = 1729$ cm^{-1} (b). The other topographic features are polystyrene beads, showing no phase shift due to the lack of carbonyl resonance. Fig. 4.6 (c) shows the *s*-SNOM spectrum on PMMA, with phase in blue and amplitude in red. The *s*-SNOM phase shows an absorptive-like profile, with peak of 1.2 radian (60 deg). The *s*-SNOM amplitude, as ratio of scattering intensity of PMMA to the surrounding epoxy, follows a dispersive line shape.

To correlate the nanoscale *s*-SNOM spectra to the sample dielectric function, I re-plotted the same *s*-SNOM spectra with the refractive index (n and κ) of PMMA from ellipsometry measurement. Fig. 4.7 (a) shows the normalized *s*-SNOM real and imaginary spectra in red and blue dots, with solid line for ellipsometry data. After proper scaling, we see the *s*-SNOM spectrum overlaps very well with the bulk dielectric function of PMMA. To understand the spectral phase shift, I plotted *s*-SNOM phase and imaginary part together with the extinction coefficient κ after multiplying a factor of two. In Fig. 4.7 (b) we can see the imaginary part of the *s*-SNOM signal overlaps well with the extinction coefficient κ, while the peak of *s*-SNOM phase is blue shifted

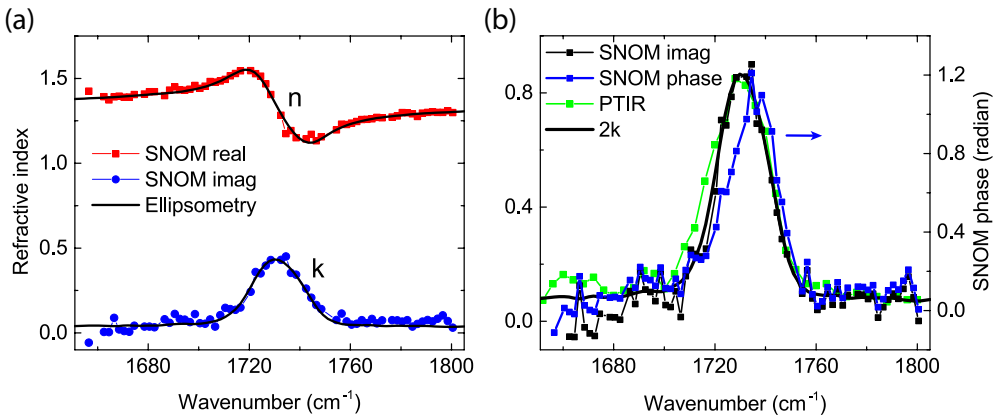

Figure 4.7: (a) Normalized *s*-SNOM real and imaginary spectra together with the complex refractive index n and κ. (b) *s*-SNOM imaginary spectrum (black dots) agrees well with 2κ (black solid), while the *s*-SNOM phase (blue dots) is blue shifted by about 10 cm^{-1}. In addition, I plotted PTIR measurement on the same sample (green dots) for comparison.

by about 10 cm^{-1}, in agreement with prediction in Fig. 4.4. A photothermal induced resonance (PTIR) spectrum of the sample sample (green curve) is plotted for comparison [45], which overlaps with the *s*-SNOM imaginary spectrum. It worths to note this is the first time a direct comparison of PTIR spectrum with *s*-SNOM spectrum in experiment has been made. From this comparison, we conclude the imaginary part of *s*-SNOM corresponds well to the extinction coefficient κ, and can be used for chemical identification.

4.4 Spectroscopic nano-imaging and applications

After explaining the principle, below I show a few representative examples of spectral imaging for different applications. All data are taken with the infrared *s*-SNOM system I built.

4.4.1 Chemical vibrational resonance

Chemical specific nanoscale imaging can be achieved in *s*-SNOM by combining with label-free vibrational spectroscopies. Here I image membrane protein bacteriorhodopsin (bR) in dried purple membrane as an example to test chemical specificity in IR *s*-SNOM [21]. The protein peptide bonds in bR has a characteristic amide I vibrational mode at around $\omega = 1667$ cm^{-1}, which can be

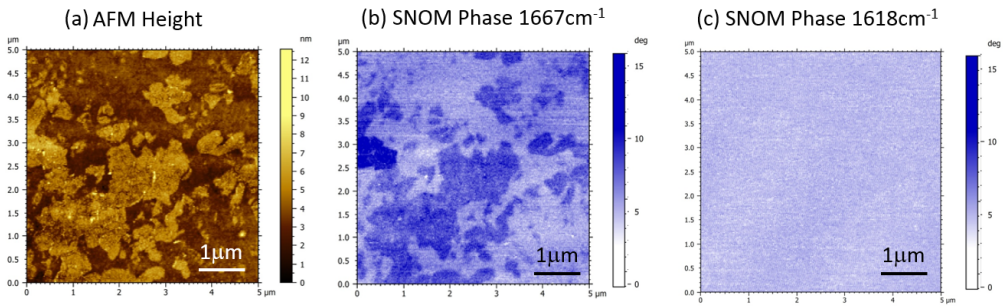

Figure 4.8: Chemical imaging of purple membrane on and off resonance of the amide I band. *s*-SNOM phase images of bacteriorhodopsin (bR) of a disordered dried purple membrane patch at amide I band reveal distribution of protein within the lipid membrane. (a) AFM height; (b) *s*-SNOM phase image with IR source tuned to the amide I absorption band; (c) *s*-SNOM phase image taken off resonance.

covered with a tunable CW QCL laser source of spectral range from $\omega = 1570$ cm^{-1} to 1750 cm^{-1}. Fig. 4.8 shows the resulting *s*-SNOM measurements of bR. When the laser is tuned to on resonance at 1667 cm^{-1}, the bR clearly shows a phase contrast (b). The contrast disappears off resonance at 1618 cm^{-1} (c). Phase image obtained at the resonance of amide I band reveals distribution of protein within the lipid membrane.

4.4.2 Surface plasmon polariton and surface phonon polariton

Another interesting application for *s*-SNOM is to study 2D materials with surface plasmon polaritons (SPP) or surface phonon polaritons (SPhP). These surface waves can be used as a sensitive probe to measure the microscopic spatial variations of the underlying optical and electronic properties of 2D materials, such as measuring carrier mobility in graphene and visualizing grain boundaries in chemical vapor deposition (CVD) grown graphene [66, 35, 65, 78].

Graphene has zero bandgap. However, with modified Fermi level (E_F) by gating or doping, graphene can have a Drude-like response at low optical frequency ($\omega < 2E_F$) due to Pauli blocking of the occupied electron states. The Drude-like response can result in propagating SPPs in graphene similar to SPPs in a metal-dielectric interface. However, low frequency plasmons are dormant in conventional infrared spectroscopy of graphene because of mismatch in momentum. In *s*-SNOM high momenta can be provided by coupling the infrared light to the tip, which enables *s*-SNOM to

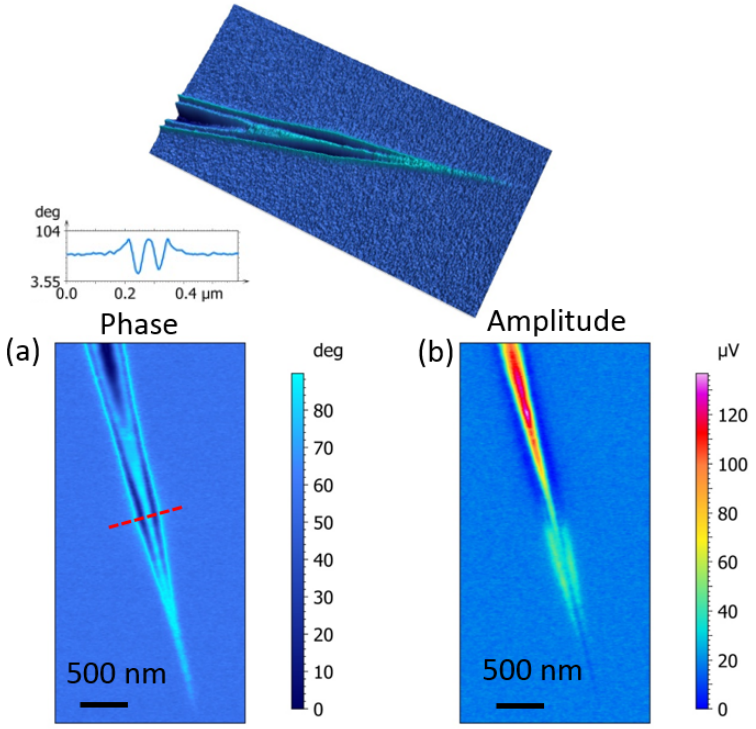

Figure 4.9: Graphene wedge shows clear SPP propagating. Phase and amplitude images of surface plasmon polariton (SPP) on a graphene wedge. *s*-SNOM phase with a line cross-section of the SPP standing wave; (b) *s*-SNOM amplitude image. Top image is a 3D view of the phase image in (a).

launch and image SPPs in graphene.

Fig. 4.9 shows *s*-SNOM measurements on exfoliated single layer graphene with a wedged shape. The measurement is done with a $^{13}CO_2$ laser at $\lambda = 10.8$ μm. The monolayer graphene sample is adhered to a SiO_2 dielectric substrate. Due to the substrate, the graphene sample is unintentionally hole doped with equivalent $E_F \approx 0.4$ eV. Launching SPPs requires large in-plane momentum, which is provided by coupling the infrared light to the sharp tip. The SPPs then propagate along the surface and reflect at the wedge boundary. The reflected surface waves interfere with the near-field at the tip, consequently scatter by the tip and are detected in the far field. In Fig. 4.9 amplitude (b) and phase (a) images reveal excited SPP standing waves pattern along the graphene edges. The line profile of the phase signal at one cross-section of the wedge shows the interference fringes, with a dramatic phase change close to 90 deg.

The SPPs in graphene can be used to characterize CVD grown graphene, where the macro-

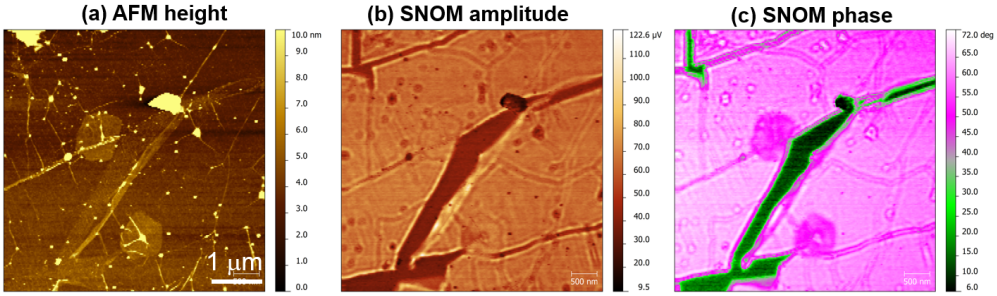

Figure 4.10: CVD graphene with grain boundary. (a) AFM height image shows cracks on the graphene sample; *s*-SNOM amplitude (b) and *s*-SNOM phase image (c) reveals internal grain boundaries together with cracks.

scopic electronic and optical properties largely depends on the characteristics of the grain boundaries. Grain boundaries are atomic dislocations of carbon atoms along a large domain boundary. The atomic dislocation is difficult to image with AFM, but it can cause disturbance to propagating surface waves. Fig. 4.10 shows *s*-SNOM measurement on CVD graphene. The 5×5 μm AFM image (a) shows cracks among the sample, with otherwise flat surface. These cracks lines as external boundary are visualized as double lines caused by interference of SPPs in the *s*-SNOM amplitude (b) and phase images (c). The *s*-SNOM amplitude and phase image also reveals internal grain boundaries in otherwise topographically flat regions.

Besides the gapless graphene, there is another class of 2D materials with band gaps. This diverse class is called layered van der Waals materials including hexagonal-Boron nitride (hBN) [43, 44]. hBN is a layered polar dielectric material with a band gap larger than 5 eV. The material has strong in- and out- of-plane longitudinal optical (LO) phonon modes at frequencies of 1380 cm^{-1} and 780 cm^{-1}, respectively [43]. Analogy to SPPs in graphene, hBN supports surface phonon polariton (SPhP) waves. In the experiment, I used a tunable QCL (Daylight) with frequency at 1580 cm^{-1} for *s*-SNOM measurements. The SPhPs being excited with nanofocused infrared light forms standing waves after reflected from the boundary of the hBN sheet. Fig. 4.11 shows the standing waves of SPhP on hBN. The oscillatory period of standing waves λ_{SPhP} is a function of the sample thickness. The AFM height image (a) shows a homogeneous flat surface of hBN, with different layers at the boundary. The SPhPs with high oscillation amplitude can be seen in both

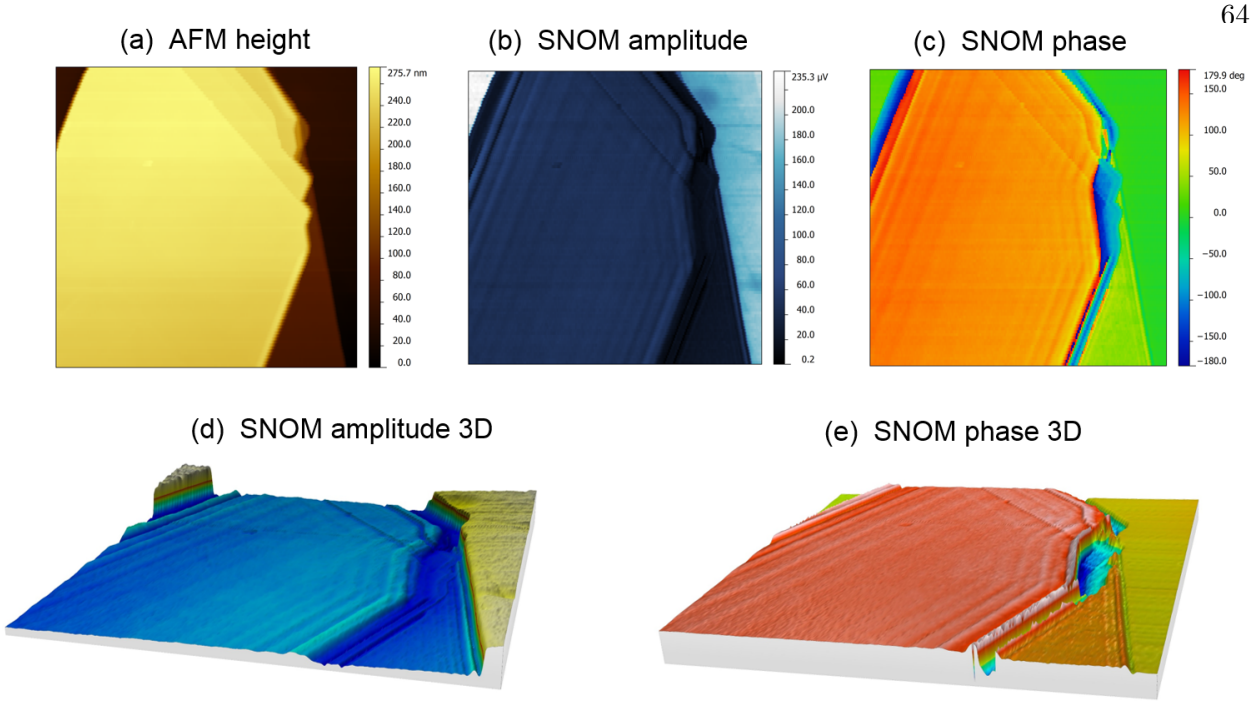

Figure 4.11: Nano imaging of surface phonon polaritons (SPhP) in hexagonal boron nitride (hBN) (5 μm $\times 5\mu$m). (a) AFM height image shows homogeneous hBN surface with different layers on Si substrate; (b) *s*-SNOM amplitude shows strong interference fringes due to propagating surface phonon polariton (SPhP) along the surface on hBN; (c) *s*-SNOM phase image shows phase changes depending on layer thickness; (d,e) are corresponding 3D displays for (b,c). From the *s*-SNOM images, we can see the wavelength of the SPhP changes with the number of layers.

s-SNOM amplitude (b) and phase (c) images. By comparing the λ_{SPhP} for different layers, we see larger λ_{SPhP} for thicker hBN layers. This real space image reveals a tunability of hBN SPhPs with layers.

4.5 Conclusion and outlook

In conclusion, infrared *s*-SNOM provides nanometer spatial resolution to infrared spectroscopy. Through theory and experiment, I have demonstrated the spectroscopy and imaging capability of infrared *s*-SNOM. My study confirms the complex near-field signal directly correlates to the dielectric function of sample material. In addition, surface polaritonic interferometry through *s*-SNOM provided by the high k-vector of tip coupling enables optical and electric characterization of 2D materials. The generalization of *s*-SNOM with ultrafast and nonlinear optics will eventu-

ally achieve the ultimate goal of femtosecond time resolution with nanometer spatial resolution. More and more exciting applications of this technique are expected with the commercialization of *s*-SNOM instruments, which I am actively involved in.

Chapter 5

Development of low temperature *s*-SNOM system

Following a general discussion on principles and applications of *scattering-type* scanning near-field optical microscopy (*s*-SNOM), this chapter describes a versatile *s*-SNOM instrument I built together with Erik Hebestreit for studying low temperature physics, including metal-insulator transition in correlated electron materials. As one of the first cryogenic *s*-SNOM instruments, I discuss the considerations in instrument designs. Its performance is demonstrated on mid-infrared Drude response by probing of the domain formation associated with the metal-insulator transitions (MIT) of VO_2 ($T_{MIT} \simeq 340$ K) and V_2O_3 ($T_{MIT} \simeq 150$ K). This *s*-SNOM instrument can operate under cryogenic and variable temperature ($\sim$ 20 - 400 K) and is compatible with high magnetic fields (up to 7 T). The instrument features independent tip and sample scanning (scan range 50 μm $\times$ 50 μm $\times$ 24 μm) and free-space light delivery with an integrated off-axis parabolic mirror for tip-illumination and signal collection with a numerical aperture of NA=0.45. The optics operates from the UV to THz range allowing for continuous wave, broadband, and ultrafast *s*-SNOM spectroscopy.

5.1 Instrument Design of low temperature *s*-SNOM

The design of a cryogenic *s*-SNOM instrument requires a set of primary considerations critical for reaching the desired optical, thermal, and magnetic field specifications. The overall geometry of the setup is determined by the need for broadband illumination, large solid angle for tip-scattered

Work in this chapter is published in Rev. Sci. Instruments 84, 023701 (2013)

light collection, compatibility with low temperatures, and large magnetic fields. This leads to several trade-offs, e.g., a compact design is desired to fit into the bore of a superconducting magnet which restricts the optical access with large numerical aperture for most efficient tip illumination and near-field scattering collection.

Given the restricted space inside the magnet bore, the incident and outgoing beams are chosen to be parallel or collinear. Furthermore, the incident beam enters the apparatus from the bottom, such that the optical axis is parallel to the magnetic flux lines and instrument axis (Fig. 5.1). This illumination scheme requires only a single-solenoid magnet, while simultaneously yielding a short and interferometrically stable beam delivery. The bottom incidence design also allows for the conventional upright AFM orientation. An off-axis parabolic mirror is positioned at the side of the sample stage with its focus at the tip location. The numerical aperture is maximized within the limits of the sample plane, tip axis, scan range, magnet geometry and maximum beam size.

The system features independent tip and sample positioning which is desirable for an optimal optical alignment procedure as discussed in section 5.1.2.

System cooling is performed by a modified Janis ST500 cryostat. It features a 25 mm diameter bottom BaF_2 window (ISP-Optics, BF-W-38-5), suitable for beam delivery from the UV to mid-IR. The cryostat was chosen to meet the temperature requirements. Turbo-molecular pump and other vacuum components were chosen or designed to maximize stability and minimize vibrations.

5.1.1 AFM

A dynamic force AFM (Attocube Systems AG) serves as the core component for the cryogenic *s*-SNOM system. It consists of two 3-axis piezo slip-stick stages (ANPxyz101) for independent tip and sample positioning. Each stage features a 5 mm coarse xyz travel range, with a step size of about 100 nm at room temperature.

An open loop 3-axis piezo scanner (ANSxyz100) is mounted on top of the sample stage. This scanner has a range of 50 μm $\times$ 50 μm $\times$ 24 μm at room temperature (30 μm $\times$ 30 μm $\times$ 15 μm at 4 K). The cantilever oscillation is tracked interferometrically by a single mode fiber placed 50 -

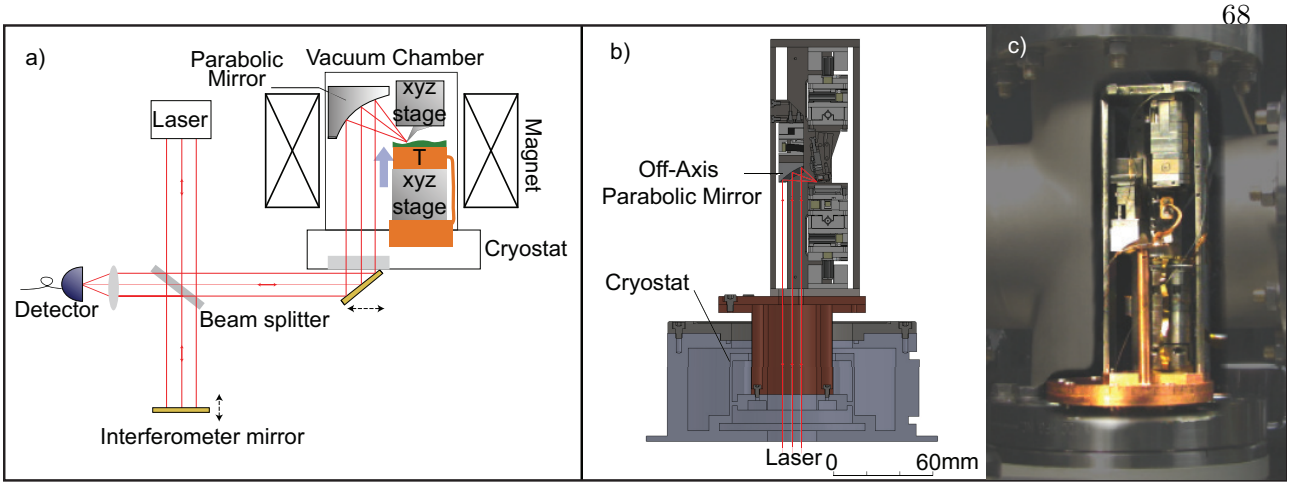

Figure 5.1: Cryogenic scattering-type scanning near-field optical microscopy (s-SNOM) system, based on a contact and dynamic force AFM with optics for tip illumination and collection of scattered near-field light. (a) s-SNOM schematic. The blue arrow in the center of the vacuum chamber indicates the magnetic field direction; the copper block marked with T is the heater and temperature sensor connected to the flow cryostat. (b) Cross-sectional view of core components. The AFM consists of two positioners for independent tip and sample spatial control. Light is focused by an off-axis parabolic mirror, mounted on a 2-axis goniometer. All components are held by a titanium housing mounted on a continuous flow cryostat, with optical access through its base for epi-illumination and detection. The dimensions are minimized such that insertion into a high-field (6.5 T) superconducting magnet (not shown) is possible. (c) Photo of the s-SNOM apparatus, with AFM inside the test chamber (cut away view).

100 μm from the backside of the cantilever [199]. The AFM allows for a variety of imaging modes, including contact, non-contact atomic force, magnetic force, and conductive microscopy.

A titanium housing for the components ensures a non-magnetic, rigid mounting with low vibration transmission. The translation stages are also made of titanium, and provide minimal absolute and relative thermal expansion. The slender design of the positioners and scanners leaves outer dimension of $\sim$ 24 mm $\times$ 24 mm. Since the superconducting magnet bore is 74 mm in diameter, this leaves enough space for optical access.

The vibration spectrum was analyzed with both an external accelerometer and a built-in AFM noise analyzer. Results indicated minimal vibrations levels, with mechanical amplitudes $\lesssim 1$ nm (RMS).

5.1.2 Optics

Free space beam delivery of the incident and scattered beams is necessary for *s*-SNOM in order to allow the wide spectral range (UV-THz) and large spectral bandwidth required for short pulse excitations. This rules out fiber delivery due to dispersion and transmission constraints.

For broadband light and ultrashort laser pulse illumination, reflective optics are superior to refractive optics since the absence of material dispersion eliminates any chromatic or other aberration for confocal applications. Parabolic mirrors are preferable to Cassegrain objectives, as they are more compact and have shorter focal lengths. However, parallelism of the incident light beam with respect to the optical axis of the off-axis parabolic mirror is crucial to avoid coma in the focus [138, 9].

A customized off-axis parabolic mirror (Nu-Tek Precision Optical Corporation) with a focal length of 11.25 mm and a numerical aperture of 0.45 is used. The surface roughness is specified to be 7 nm RMS and the form accuracy is specified to be below 0.625 μm. The mirror is mounted on a piezo-driven 2-axis goniometer (Attocube ANGt50/ANGp50) with a tilting resolution of 10^{-4} degree. With the aid of a flat face precision machined on the mirror, the mirror axis is aligned to the incident laser beam. During the initial alignment, a red HeNe laser is used to guide the beam path and focused to the tip apex by parabolic mirror. Fig. 5.2 shows the laser illuminated tip from both a side camera (a) and a camera in the beam path (b). Fine tuning of the laser focus is achieved by optimizing the tip apex scattering to be as small and symmetric as possible. After aligning the visible guide laser to the tip, other laser sources can be coupled into the system by aligning them co-linearly with the alignment laser.

5.1.3 Cryostat and Vacuum system

A number of factors are taken into account for optimal sample cooling. A thermal link made of a stack of 20 laser welded gold plated OFHC copper foils (Attocube Systems AG, ATC100), with thermal conductivity of 10 mW/K, is used to couple the sample to the cryostat.

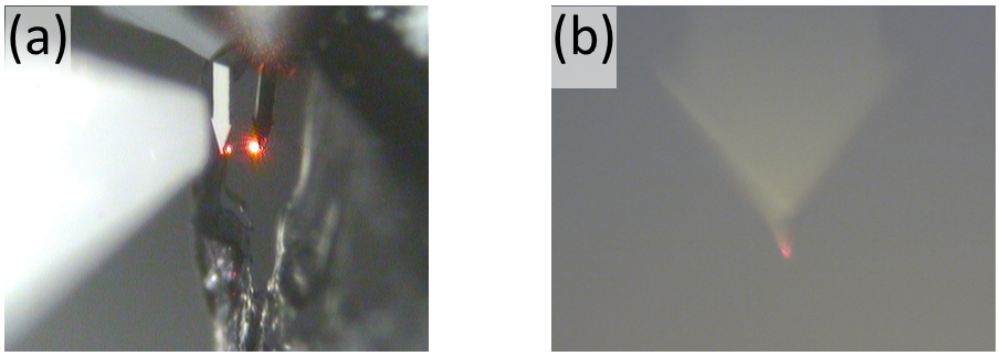

Figure 5.2: Laser illuminated tip seen from the side camera (a) and from a camera in the beam path (b). The scattered light from the tip apex can been clearly seen from both images if the optics is well aligned.

To minimize the heat conduction from the translation stage to the sample holder, a teflon thermal isolation plate sandwiched by two layers of Aluminized Mylar foil is placed underneath the sample holder. The multiple interfaces between sample holder and the translation stage reduce the heat conductance to be below 1 mW/K [62].

To minimize heating effects through heat conduction via the wires of the heater and the temperature sensor, these cables were coiled around the cryostat and pre-cooled. Finally, to keep laser heating of the sample at a minimum, the incident laser power is kept below 10 mW, which is also a typical power level for *s*-SNOM .

The heat conduction via the gas with pressure below 0.1 Pa is estimated from $\dot{q}_{\mathrm{gas}} = 0.5kpA\Delta T$, where k is an empirical coefficient of 1.2 for air, p the pressure (Pa), A the sample holder surface area (m^2), and ΔT the temperature difference between sample and the room temperature chamber wall (K) [62]. For our conditions $\dot{q}_{\mathrm{gas}}$ can be estimated to be ~ 0.7 mW, and is therefore negligible.

A significant heat load arises from radiant heat flow from the surrounding chamber walls at 300 K to the sample holder at, e.g., 80 K when cooled with liquid nitrogen. We can estimate the heat transfer using the black-body radiation expression $\dot{q}_{\mathrm{rad}} = \sigma E A(T_{\mathrm{Env}}^4 - T_{\mathrm{Samp}}^4)$, to be ~ 130 mW, with σ the Stefan-Boltzmann constant, E a factor related to the emissivities of the surfaces (taken as 0.5), A the sample holder surface area (m^2), and T_{Env} and T_{Samp} the environment and

sample temperature respectively. A thin copper radiation shield was built around the AFM and linked to the cryostat to reduce the thermal radiation. With the radiation shield at ≈ 100 K the radiation power is reduced to < 1 mW.

The sample temperature is controlled with a resistive heater and a temperature controller (Cryocon 32B), with a maximum power of 5 W, and stability within ± 0.1 K.

All materials inside the chamber are chosen to be high-vacuum compatible. With a turbo-molecular pump (Pfeiffer HiCube Eco pump station) a pressure $< 10^{-5}$ mbar is reached at room temperature.

5.1.4 Magnet

In the design, a multi-filamentary niobium-titanium superconducting magnet (Janis 6.5T-74) was used as a representative model. This superconducting magnet can produce a 6.5 Tesla vertical field, with a moderate inhomogeneity of $\pm$ 0.5 % over a 1 cm sphere. Within a typical AFM scan area of 10 μm $\times$ 10 μm, the inhomogeneity is below 10^{-3} %. The vertical center bore has a diameter of 74 mm. All the piezo motors, including goniometers, coarse positioners and scanners, are made of titanium and have demonstrated functionality under 7 Tesla magnetic fields.

5.2 Results and discussion

5.2.1 Near-field contrast of gold on silicon

To test the general system performance we have performed elastic IR *s*-SNOM with contrast resulting from the metallic Drude response. Light from a CO_2 laser (p polarized, $I = 5$ mW, $\lambda = 10.6$ μm) is focused onto a commercial Pt-Ir coated AFM tip (Nanosensors, Arrow NCPt). The optical signal is detected in the back scattered direction by a liquid nitrogen cooled HgCdTe detector (Judson, J15D14-M204-S250U-30) with a high bandwidth transimpedance preamplifier (Femto, HVA-S).

The AFM operates in dynamic force mode, with a controlled tip oscillation amplitude of

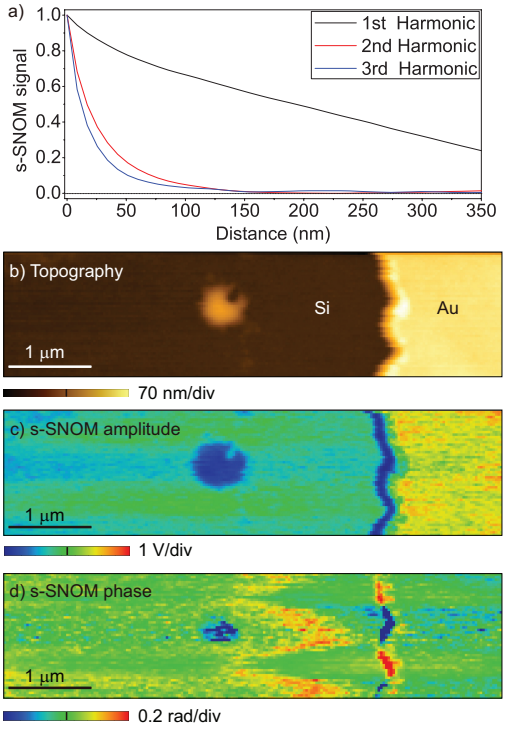

Figure 5.3: Approach curves on Au at the first three tip harmonic demodulations show a near-field localization < 30 nm (a). Panels (b, c, d) display the topography and associated *s*-SNOM optical signal measured using pseudo-heterodyne signal filtering techniques for a Au-Si interface using optical excitation from a CO_2 laser ($\lambda = 10.6$ μm). A clear correlation of the measured optical signal (c) with the substrate material is observed.

about 20 nm, and frequency $\Omega \approx 250$ KHz. The near-field contribution is selected by lock-in demodulation at harmonics of the tip oscillation frequency (Ω, 2Ω, 3Ω). The optical response during approach gives a clear indication of the near-field optical contrast [195]. Here, approach curves over a flat gold surface in Fig. 5.3a show a strong nonlinear distance dependence, confirming the near-field signal origin.

To reduce far-field background and obtain near-field phase information, pseudo-heterodyne detection is utilized. In pseudo-heterodyne the signal is amplified interferometrically, and the phase of the reference field E_r modulated at a frequency ω_r (Fig. 5.1a) [175]. The signal at the detector contains a near-field component E_s, far-field background from the tip shaft E_b and the reference field E_r, with total intensity $I \propto |E_s(\Omega) + E_b(\Omega) + E_r(\omega_r)|^2$. The near-field E_s is extracted by demodulating I at side bands of frequency $n\Omega + m\omega_r$, where n, m are integers [14]. Fig. 5.3(b,c,d)

show an *s*-SNOM scan at 2Ω across the edge of a Au film evaporated onto a silicon surface. The simultaneously acquired topography and optical maps demonstrate the clear distinction of gold and silicon in the optical amplitude with pseudo-heterodyne detection. No phase contrast is expected and the small variation of $\Delta\phi \sim 10^\circ$ observed (Fig. 5.3d) is due to residual far-field interference.

5.2.2 Imaging phase transition of VO_2 and V_2O_3

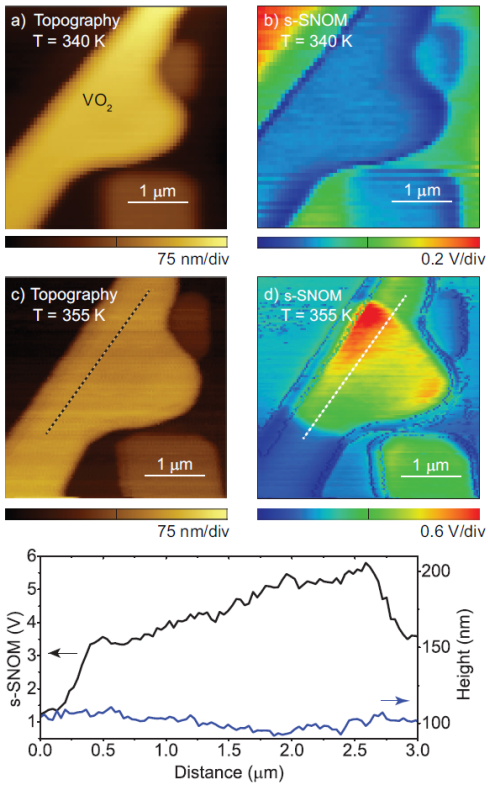

Figure 5.4: The topography (a, c) and near-field response (b, d) of a VO_2 crystal at 340 K (a, b) and 355 K (c, d). Due to the difference in conductivity of the two phases, the insulating phase appears dark and the metallic phase appears bright. (e) *s*-SNOM signal together with topography line-scan along the dashed line in (c, d).

To demonstrate the ability to probe phase transitions above and below room temperature, micrometer-sized vanadium dioxide (VO_2) single crystals on a silicon substrate were imaged. VO_2 undergoes a first-order metal-insulator transition (MIT) from a low-temperature monoclinic insu-

lating phase to a high-temperature rutile (R) metallic phase at T_{MIT}= 340 K. These substrate bounded single crystals form domains during the MIT due to external substrate-induced stress [113]. Fig. 5.4 shows the *s*-SNOM image with corresponding topography. The crystal remains insulating at 340 K (Fig. 5.4b) and becomes metallic at 355 K (Fig. 5.4d) showing increased optical signal due to increased optical conductivity of the metallic phase. *s*-SNOM line scan over a VO_2 crystal (Fig. 5.4e) shows optical contrast of metallic domains, with no alleviated topographic variation.

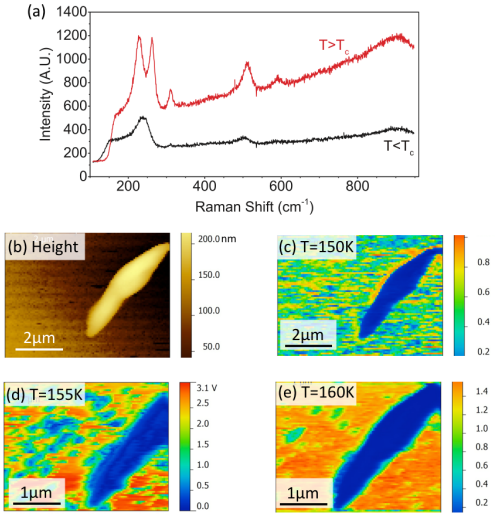

Figure 5.5: (a) Cryogenic micro-Raman spectrum shows a spectral difference below and above phase transition temperature (T_c). Mid-IR *s*-SNOM optical images of doped V_2O_3 (c-e) with corresponding topography (b). Metallic phases (red) are seen to nucleate near defects (large islands are due to dielectric surface impurity).

V_2O_3 is a paramagnetic metal at room temperature with an MIT around 150 K, accompanied by a structural change from rhombohedral to monoclinic symmetry [53], and it undergoes magnetic ordering from a paramagnetic metal to an antiferromagnetic insulator [153]. The MIT can be tuned by pressure or doping which modifies the magnetic orderings. Recently, the domain evolution across the paramagnetic insulator to paramagnetic metal phase transition on chromium doped V_2O_3: $(V_{1-x}Cr_x)_2O_3$, x=0.011 was studied using PEEM [144]. Here we use micrometer sized V_2O_3 single

crystal to check the system performance at low temperature. The sample has been studied with cryogenic Raman measurement, and the phase transition manifests itself in phonon Raman response acquired *ex-situ* at different temperatures (Fig. 5.5a). By cooling the system starting from room temperature, insulating domain begins to form around topographic defects at $\sim$ 160 K as shown in Fig. 5.5 (c-e).

5.3 Conclusion and outlook

In conclusion, I designed and built a versatile cryogenic *s*-SNOM instrument compatible with strong magnetic fields. This system, in combination with linear, nonlinear, and ultrafast spectroscopy, could provide spectroscopic access to electronic and vibrational resonances, structural symmetry, and femtosecond dynamics with few-nanometer spatial resolution. The sensitivity, specificity, and selectivity of the optical interaction allows for the systematic real space probing of multiple order parameters and phases of complex materials simultaneously. The instrument is applicable to a range of materials with related physical phenomena, including organic conductors and semiconductors which also exhibit electron correlation, charge order, and superconducting gaps.

Chapter 6

Accessing the optical magnetic near-field through Babinet's principle

Engineering the optical magnetic field with optical antennas or metamaterials extends the ways to control light-matter interaction. However, characterization of optical magnetic field in the nanoscale is challenging due to the weak magnetic interaction.

In this chapter, we developed a new method for imaging optical magnetic field with Babinet's principle. The method is demonstrated on a complementary system of a slot and rod antenna. The magnetic near-field of a rod antenna can be determined by measuring the electric near-field of a corresponding slot antenna. Using combined far-field spectroscopy, near-field imaging, and theory, we identify magnetic dipole and higher order bright and dark magnetic resonances at mid-infrared frequencies. From resonant length scaling and spatial near-field distribution, we confirm the applicability of Babinet's principle over the mid-infrared spectral region. Babinet's principle thus provides access to spatial and spectral magnetic field properties, leading to the targeted design of magnetic optical antennas.

6.1 Introduction

Controlling the optical magnetic field with optical antennas or metamaterials provides for new ways of tuning the near-field light-matter interaction [188, 63, 8, 117, 119]. Because the magnetic dipole transition probability is in general $\sim 10^4$ times smaller than the electric dipole

Work in this chapter is published in ACS Photonics 1, 894 (2014)

transition, the magnetic response at optical frequencies is typically weak [111, 80, 39]. However, in addition to the transition moment, the interaction rate highly depends on the electromagnetic local density of states (EM-LDOS), which can be modified through the local environment. Examples include the use of magnetic plasmonic structures for magnetic field enhancement over 100 times [87, 128, 67], achieving magnetic nonlinear effects with metamaterials [123], nanorod metamaterials for biosensing [116], or tailoring the magnetic dipole emission with plasmonic structures [98].

Despite the prominent role of the magnetic field in many nano-optical devices, probing magnetic resonances and local magnetic near-field properties, as desirable for design and device performance evaluation, has remained difficult [32, 178, 207, 203]. Vector-resolved electric near-field measurements at optical frequencies using scanning near-field probes can be used to derive the magnetic field through Maxwell's equations [178, 86]. Equally indirect, aperture-based near-field imaging allows one to investigate the magnetic field coupled through a fiber [32, 120, 51, 133]. However, these methods require specially fabricated nano-probes or numerical modeling for data interpretation.

Here we demonstrate experimentally and theoretically the application of Babinet's principle in the infrared (IR) as a generalized principle to gain insight into the spatio-spectral properties of magnetic resonances, specifically from the comparison of the optical rod and slot antenna as a prototypical system [74, 76, 50, 77, 233, 176, 99]. We show that electromagnetic duality can be used to access the optical magnetic field and its structural resonance of optical rod antennas as the dual to the slot antenna in both its far-field spectral and near-field spatial response. This confirms that the theoretical requirement of Babinet's principle for the structure to be infinitely thin and perfectly conducting is still fulfilled to a good approximation in the IR.

Babinet's principle for electromagnetic fields connects the scattered fields by two complementary planar screens S and S_c, which are infinitely thin and perfect conducting [106, 27]. As illustrated in Fig. 6.1, if the incident fields on the original screen S are $\mathbf{E_0}$ and $\mathbf{B_0}$, then the

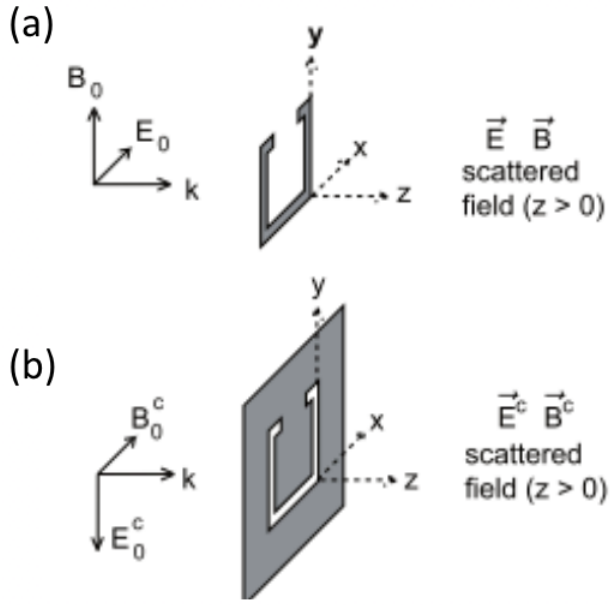

Figure 6.1: Babinet's principle relates the scattered fields $\mathbf{E}$ and $\mathbf{B}$ behind the screen S, and the scattered fields $\mathbf{E^c}$ and $\mathbf{B^c}$ behind the complement screen S_c. Figure after [24].

complement fields $\mathbf{E_0^c}$ and $\mathbf{B_0^c}$ for S_c are defined as:

$$\mathbf{E_0^c} = -c\mathbf{B_0}, \tag{6.1}$$

$$\mathbf{B_0^c} = \mathbf{E_0}/c, \tag{6.2}$$

with c the speed of light. The Babinet's principle for full vectorial electromagnetic fields states that the scattered fields $\mathbf{E}$ and $\mathbf{B}$ of the screen S, and the scattered fields $\mathbf{E^c}$ and $\mathbf{B^c}$ of the complement screen S_c must satisfy

$$\mathbf{E^c} = c\mathbf{B} + \mathbf{E_0}, \tag{6.3}$$

$$c\mathbf{B^c} = \mathbf{B_0} - \mathbf{E}. \tag{6.4}$$

For the case of a plane wave with normal incidence $(\mathbf{E_0})_z = 0$, thus in the direction normal to the plane $(\mathbf{E^c})_z = c\mathbf{B}_z$ or $\mathbf{B}_z = (\mathbf{E^c})_z/c$. This provides a way to measure the out-of-plane magnetic field of a structure through measuring the out-of-plane electric field of its complement structure. Indeed, this approach is widely used in radio-frequency (RF) antenna and THz metamaterial design [15, 64, 24]. However, the rigorous validity of Babinet's principle requires perfect conductivity, which

no longer holds in the IR with relatively high Ohmic losses in metals [232, 197]. Here, we study the validity of Babinet's principle in the IR by examining one particular dual system of a rod and its complement slot. As shown in Fig. 6.2a, a rod (structure 1) and its complement slot (structure 2) form the dual system in Babinet's principle. Thus according to Babinet's principle, the fields should be related by $\mathbf{E}_1/c = \mathbf{B}_2$ and $\mathbf{E}_2/c = -\mathbf{B}_1$. This relation is to be verified by experiments and numerical simulations.

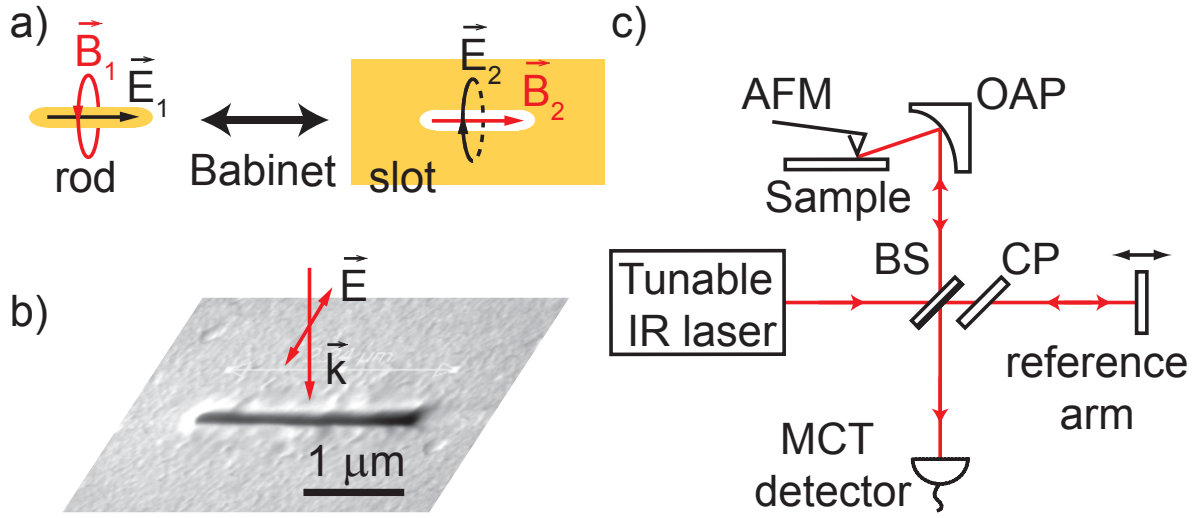

Figure 6.2: (a) The electromagnetic field of a slot antenna and its complementary linear rod antenna are related through Babinet's principle. (b) Scanning electron microscopy (SEM) image of a slot antenna, with illustration of the incident laser field polarized perpendicular to the slot direction. (c) scattering-type scanning near-field microscopy (*s*-SNOM), using tunable femtosecond OPO/DFG excitation and interferometric near-field detection.

6.2 Experiment

Slot antennas were fabricated by focused ion beam (FIB) milling into a thermally evaporated 50 nm thick Au film on KBr and on silicon (with an approximately 3 nm native SiO_2 layer). The slot lengths range from 500 nm to 2600 nm with width of 150 nm. The individual slots are separated by > 20 μm to allow for their individual far-field spectroscopic characterization. The Au thickness

of 50 nm was chosen to be greater than the optical skin depth of Au of about 20 nm throughout the IR [180].

To determine the resonant wavelength of slot antennas, the transmission spectra of the individual slot antennas on a KBr substrate were measured using an IR microscope at Beamline 1.4 at the Advanced Light Source (ALS) synchrotron at Lawrence Berkeley National Laboratory, providing bandwidth from 800–10,000 cm^{-1}. Fig. 6.3 shows a schematic setup of the IR microscope for transmission measurement. For illumination and collection two Schwarzschild type objectives were used (32×, NA=0.65), with nominal incidence angle between 18 degrees to 40 degrees at focus. Spectra were measured using a Fourier transform infrared (FTIR) spectrometer (Nexus 870, Thermo Nicolet Corp.) equipped with a HgCdTe (MCT) detector and averaged over 512 scans with a spectral resolution of 32 cm^{-1}. As illustrated in Fig. 6.2b, the polarization at the sample focus was set perpendicular to the slot axis as required for excitation of slot antenna resonances.

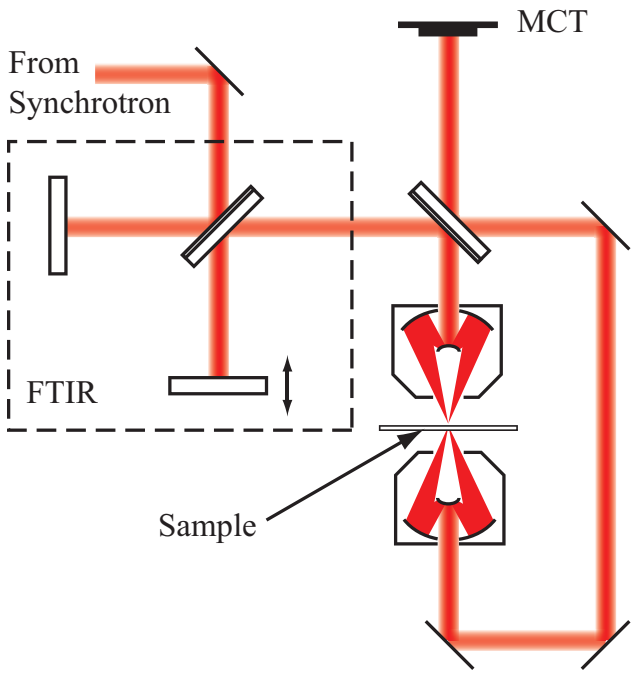

Figure 6.3: Schematic setup of the IR microscope for transmission measurement. For illumination and collection two Schwarzschild type objectives were used (32×, NA=0.65), with nominal incidence angle between 18 degrees to 40 degrees at focus. Spectra were measured using a Fourier transform infrared (FTIR) spectrometer.

Near-field measurements were performed by scattering-type scanning near-field optical microscopy (s-SNOM) based on an atomic force microscope (AFM, Innova, Bruker Corp.) in non-contact imaging mode (see Fig. 6.2c) as described previously [177, 178]. For that purpose mid-IR light was generated by difference frequency generation (DFG) in a GaSe crystal of the signal and idler beam from a fan-poled $LiNbO_3$-based optical parametric oscillator (OPO, Chameleon, Coherent Inc.) pumped by a Ti:Sapphire oscillator (Mira-HP, Coherent, Inc.). The IR radiation (~ 280 μW, full width at half-maximum bandwidth of 85 cm^{-1}, pulse duration of 220 fs, and repetition rate of 80 MHz), polarized normal to the slot orientation, is focused to a nearly diffraction-limited spot at the tip-sample region with side illumination, using a 25.4 mm working distance 90° off axis parabolic (OAP) reflector. The tip-scattered antenna near-field is collected by the same parabolic mirror in a backscattering geometry and filtered by a vertical polarizer before being directed to a MCT detector, where it is detected interferometrically. Demodulation of the signal at the 2nd or higher harmonic of the tip-dither frequency Ω_{AFM} using a lock-in amplifier suppresses the far-field background signal [177]. s-SNOM imaging provides a two-dimensional map of the z component of the electric near-field E_z, assisted by the preferential scattering of the tip-parallel field component. Homodyne interference and reference phase are adjusted such that the E_z near-field signal is symmetric with respect to the substrate non-resonant background, as is adequate for imaging resonant structures with simple 90 degree phase behavior.

6.3 Numerical simulation

For full three-dimensional field simulations of the slot and rod antennas, a commercial finite element electromagnetic simulation package is employed (COMSOL Multiphysics).

As illustrated in Fig. 6.4, the simulated geometry for a slot antenna is a stack consisting of a substrate (KBr $\epsilon = 2.36$, or Si $\epsilon = 11.7$), a 50 nm thick gold plate with a slot in the middle, and air at the top. A surrounding perfectly matched layer (PML) is added outside to minimize reflections from boundaries. PML is an artificial absorbing layer used in simulations of wave equations to truncate open boundaries. Incident plane waves point downwards under variable angles with respect to

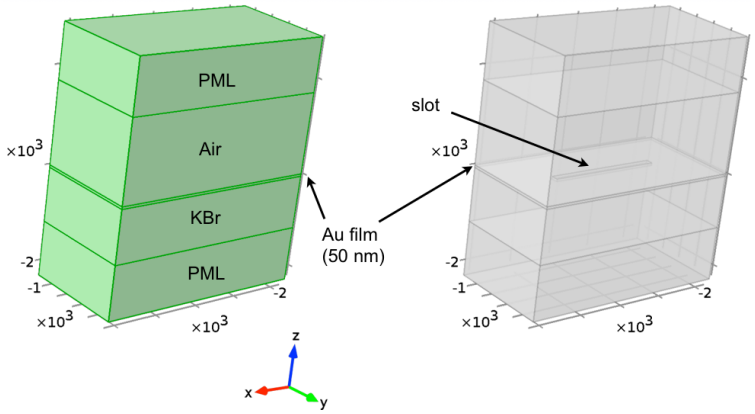

Figure 6.4: The simulated geometry for a slot antenna is a stack consisting of a substrate (KBr $\epsilon = 2.36$, or Si $\epsilon = 11.7$), a 50 nm thick gold plate, and air at the top. The slot in the middle of the gold plate can be seen in the transparent view on the right. Perfectly matched layers (PMLs) are used to truncate the open boundaries to minimize boundary reflections.

the surface normal, and are polarized normal to the slot orientation. To reduce computational complexity, mirror symmetry is employed with the mirror plane being the axial plane in Fig. 6.4. The cross-sectional view of the mirror plane is shown in Fig. 6.5a, with the gold plate highlighted. A dense mesh with element size of 5 nm or less is applied for the slot, and 25 nm or less for the gold plate. The other domains are meshed with maximum element size of $\lambda/8$, with λ being the wavelength of the incident wave.

Fig. 6.5b shows the simulation for a rod antenna. A rod made of gold is suspended in air, which is then surrounded by PMLs to truncate the open boundaries. Similar to the slot antenna simulation, incident plane waves point downwards under variable angles with respect to the surface normal, but with the polarization along the rod orientation instead of being normal. Mirror symmetry is also employed, with the mirror plane shown as the cross-sectional plane. Mesh size of 5 nm or less is used for the rod. The mesh size gradually increasing away from the rod, with maximum element size of $\lambda/8$.

The dielectric function of gold is taken from recent broadband spectroscopic ellipsometry measurements of a thermally evaporated gold sample [180]. Transmission spectra are obtained by calculating the transmission for each wavelength. The spatial near-field distribution is calculated

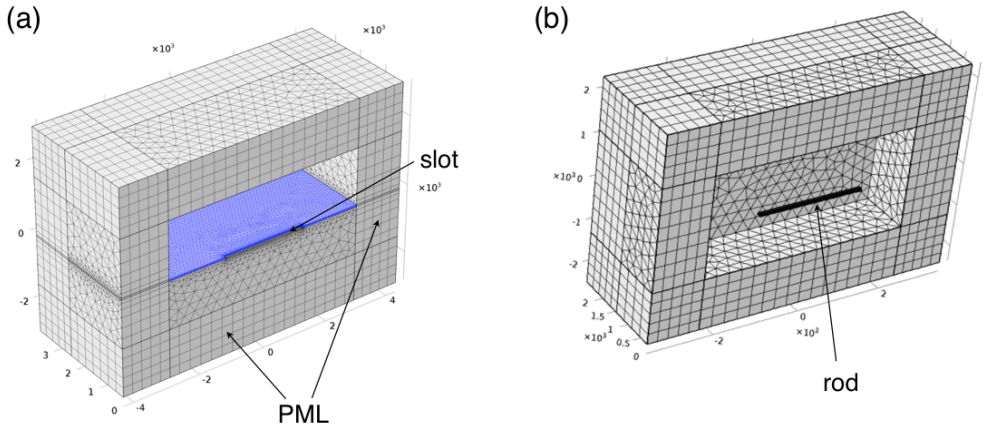

Figure 6.5: (a) Cross-sectional view along the mirror symmetry plane of the slot antenna simulation geometry. The gold plate is highlighted. PMLs are used to truncate the open boundaries. The mesh element is 5 nm or less for the slot, and 25 nm or less for the gold plate. The maximum element size is $\lambda/8$ for the air, substrate, and PML. (b) Simulation geometry of a corresponding rod antenna with a gold rod suspended in air. The air domain is truncated with PMLs. Mesh size of 5 nm or less is used for the rod, with maximum element size of $\lambda/8$ for the rest.

30 nm above the sample surface.

6.4 Results

In order to understand the resonant behavior and mode structure of a single slot antenna, we perform far-field transmission spectroscopy over a wide spectral range. Fig. 6.6 shows the measured transmission spectrum of a $L = 2.4$ μm slot on KBr (solid red line). It exhibits a pronounced fundamental dipole resonance at 1370 cm^{-1}, with a sequence of higher order modes. For comparison, the numerical simulation of an equal length slot (black dashed) is shown with 20 degree angle of incidence with respect to the surface normal with polarization perpendicular to the slot direction. The other curve is the calculated spectrum of the complementary rod antenna (blue dashed). The simulated spectra are convoluted with a Lorentzian function of 30 cm^{-1} line width to account for inhomogeneity in antenna structure and excitation focus. The difference in line width may be due to losses from surface roughness and different effective gold dielectric constant between experiment and simulation [180].

From the calculation, four modes can be assigned within the spectral range, labeled $n =$

1 . . . 4. These modes correspond to the first four lowest-order magnetic resonant eigenmodes of the slot antenna. The inset shows the corresponding schematic spatial near-field E_z distributions. The

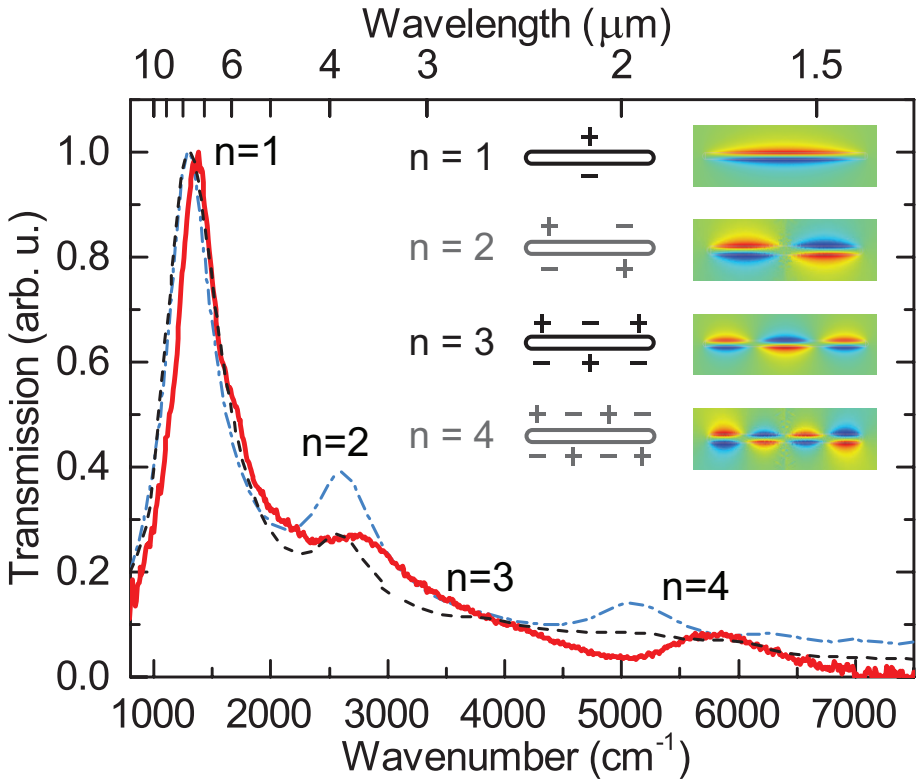

Figure 6.6: Resonant modes of a slot antenna. Experimental far-field transmission spectrum (solid red) for $L = 2.4$ μm slot compared to simulated spectrum (black dashed) and complementary rod antenna (blue dashed) with corresponding mode assignment. The four peak positions of the experimental spectrum are 1370, 2750, 4080 and 5790 cm^{-1}. Inset: Illustration of spatial near-field E_z distribution for different slot antenna modes or B_z for rod antenna, with odd (bright) and even (dark) modes.

$n = 2$ and $n = 4$ modes are dark modes and are normally forbidden for plane wave excitation at normal incidence. However, the excitation of these modes becomes allowed because of tilted incidence from the Schwarzschild type objective. The relative intensity of the four resonance peaks depends on the details of the incident field distribution. In agreement with theory, the peak of the $n = 3$ mode appears embedded in the shoulder of the $n = 2$ resonance. The small difference in peak position between experiment and theory most likely can be attributed to small differences in

geometry and dielectric function between the fabricated and simulated structures.

Fig. 6.7 shows the evolution of the measured spectral behavior for slots of varying length from $L = 0.5$ μm to 2.4 μm. The peak transmission in each spectrum is normalized with respect to the peak transmission of the $L = 2.4$ μm spectrum. For each slot length, the dominant peak corresponds to the fundamental dipolar resonance ($n = 1$) and shifts to lower frequency with increasing slot length. Higher order resonant modes shift correspondingly and decrease in amplitude with decreasing slot length.

The relation of slot length to the resonant wavelength can be derived from the transmission spectra. The antenna resonance can be explained by a Fabry-Pérot model when propagating plasmon modes form standing waves [171, 96, 209, 56, 31], given by

$$L - \frac{\delta}{2\pi}\lambda_p = n(\lambda_p/2) \tag{6.5}$$

with antenna length L, plasmon wavelength of a propagating plasmon mode λ_p, phase shift δ due to reflection of plasmon wave at the antenna end, and resonance mode number n.

For an ideal slot antenna cut from a film suspended in free space, dipole resonance occurs when the length is approximately $\lambda/2$ [127]. With the slot patterned on a dielectric half-space, together with the finite conductivity of metal at optical frequencies and low aspect ratios compared to ideal narrow slot antenna, the resonant wavelength is red-shifted.

Fig. 6.8 shows the dependence of resonant wavelengths determined from the peak positions as a function of slot length for the four modes. The length scaling can effectively be described by

$$L + \Delta L = n(\lambda_{\text{eff}}/2), \tag{6.6}$$

for $n = 1 \ldots 4$, with an apparent length increase of $\Delta L = \delta/(2\pi)\lambda_p$ due to the phase shift at the antenna end [57]. The apparent length increase ΔL is approximately the width of the antenna [171, 96, 84, 31, 209] and is negligible because of the large aspect ratio > 10 for the slots in our experiment. For $\Delta L = 0$, we obtain an effective wavelength $\lambda_{\text{eff}} = (0.64 \pm 0.05)\lambda$ from the simultaneous fit to all four modes as shown in Fig. 6.8.

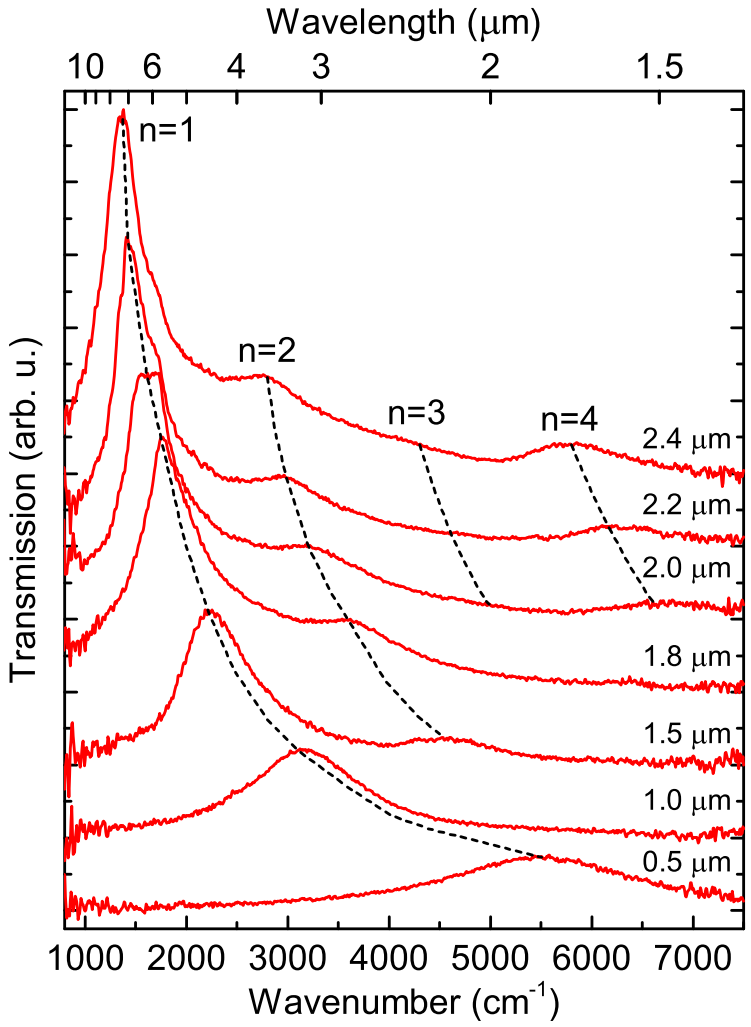

Figure 6.7: Transmission spectra of individual slot antennas on KBr substrate. For each length, the main peak corresponds to the fundamental dipolar magnetic resonance of the slot antenna $n = 1$, with higher order modes $n = 2$, $n = 3$ and $n = 4$ visible depending on length.

6.4.1 Probing the electric near-field of slot antenna

Based on the resonant characteristics determined from far-field spectroscopy, we measure the corresponding near-field spatial distribution for selected antenna modes. Fig. 6.9 shows *s*-SNOM images (b,e) of the relative E_z electric field component for two different slot lengths $L = 2.2$ μm and $L = 1.6$ μm corresponding to the $n = 1$ and $n = 3$ modes for an excitation wavelength of $\lambda = 8.7$ μm and $\lambda = 5.7$ μm respectively. The color scale reflects the regions of E_z pointing in and out of the sample plane, corresponding to an associated π phase change. Fig. 6.9(c,f) shows the

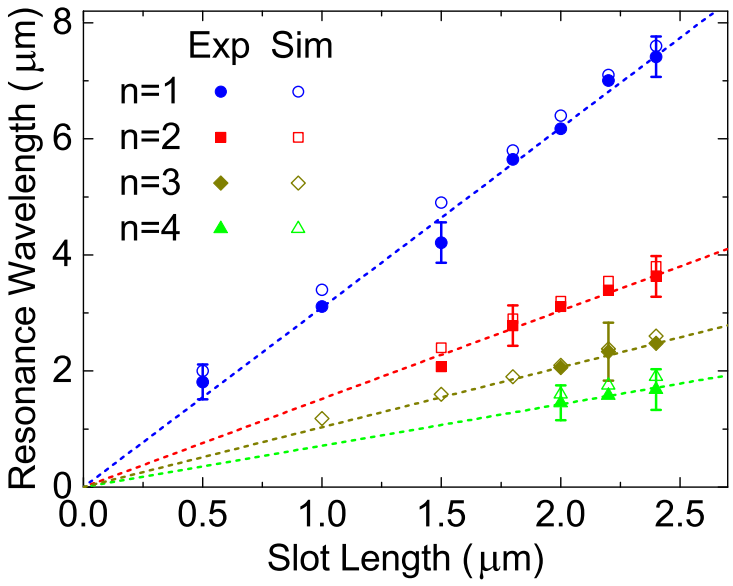

Figure 6.8: Resonant wavelength scaling of slot antennas. Resonance wavelengths from experiment (solid symbol) for $n = 1$ (blue circle), $n = 2$ (red square), $n = 3$ (dark yellow diamond) and $n = 4$ (green triangle) scale linearly with slot length, and can be described by $L = n(\lambda_{\text{eff}}/2)$ with a single $\lambda_{\text{eff}} = (0.64 \pm 0.05)\lambda$ for $n = 1 \ldots 4$ in agreement with simulation (open symbol).

result of field simulations for the given geometries and excitation wavelengths. This confirms that the experimentally observed field pattern corresponds to the pure fundamental $n = 1$ mode (b,c), and the $n = 3$ mode (e,f) which contains a slight admixture of the fundamental mode responsible for the stronger than expected center lobes.

For the fundamental $n = 1$ mode as shown in Fig. 6.9(b,c), the field distribution in three dimensions is circulating around the center axis of the slot, and decreasing in intensity in the radial direction and towards the end of the slot. This type of electric field distribution of the $n = 1$ mode thus corresponds to the electric field of a virtual oscillating magnetic dipole oriented along the slot. Correspondingly, the higher order modes can be viewed as a superposition of multiple magnetic dipoles aligned in series.

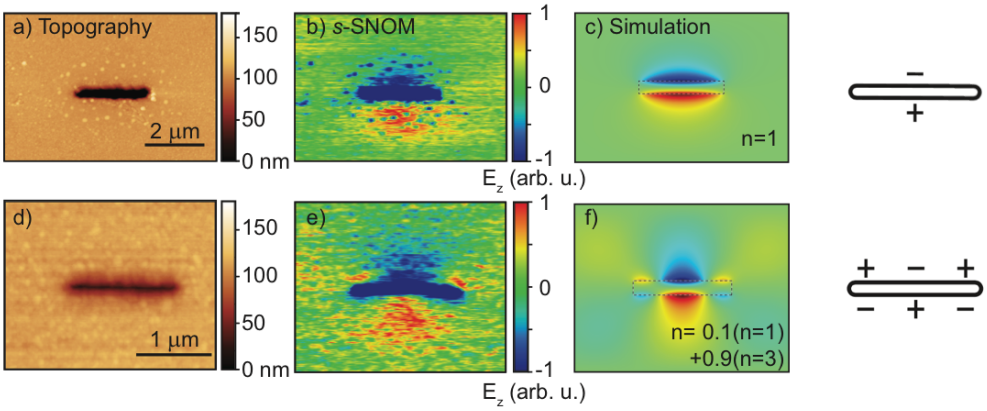

Figure 6.9: Optical near-field imaging of E_z for different resonances of slot antennas. Topography (a) and experimental near-field E_z (b) of the fundamental $n = 1$ resonance of a $L = 2.2$ μm slot antenna on Si substrate. (c) The corresponding simulation of E_z for $n = 1$ resonance shows one lobe symmetrically distributed along the slot in agreement with experiment. The E_z pointing in (- sign) and out (+ sign) of the plane is displayed in blue and red, respectively. The higher order $n = 3$ mode of a $L = 1.6$ μm slot antenna on Si substrate is excited at $\lambda = 5.7$ μm (slightly red detuned from the exact wavelength of $n = 3$ mode, limited by the laser in experiment), with topography (d) and experimental near-field E_z (e). According to the simulation, by slightly red detuning the incident laser from the exact resonance wavelength of $n = 3$ mode, a superposition of $n = 1$ and $n = 3$ resonance modes is obtained. The resulting E_z from simulation (f) shows three lobes along the slot, with a big lobe at the center and two small ones at the edges. The experimental results in general agrees with simulation, indicating a higher order resonance is being excited.

6.5 Discussion

As shown in Fig. 6.8, the effective wavelength $\lambda_{\text{eff}} = (0.64 \pm 0.05)\lambda$ obtained from experimental spectra for the slot on a KBr substrate agrees with the corresponding simulation result of $\lambda_{\text{eff}} = 0.63\lambda$. The value can be understood considering the substrate material with permittivity ϵ and the geometry of the slot with width W and length L from the relationship derived from the RF spectral region [127]:

$$\lambda_{\text{eff}} = 0.97 \frac{1}{\sqrt{\epsilon_{\text{eff}}}(1 + W/L)} \lambda, \tag{6.7}$$

where $\epsilon_{\text{eff}} = (1 + \epsilon)/2$ is the mean permittivity of substrate ϵ and air. The factor 0.97 is twice the exact scaling value associated with the fundamental dipole resonance $L = 0.485\lambda$ [179]. In this expression the inhomogeneous environment of air and substrate is approximated as an effective homogeneous medium [165]. For a slot antenna on a KBr substrate ($\epsilon = 2.36$, thus $\epsilon_{\text{eff}} = 1.68$),

Eq. (6.7) then results in $\lambda_{\text{eff}} = 0.67\lambda$, consistent with our experiment and numerical simulation. As another example, for the case of an IR slot antenna on a Si substrate ($\epsilon = 11.7$, thus $\epsilon_{\text{eff}} = 6.35$), the predicted $\lambda_{\text{eff}} = 0.35\lambda$ also agrees with the result of a full electromagnetic simulation value of $\lambda_{\text{eff}} = (0.33 \pm 0.05)\lambda$.

Eq. (6.7), although derived for RF, is also applicable in the IR with the effective medium chosen as the mean permittivity of air and substrate ϵ at the corresponding IR frequency. As shown in Fig. 6.10, the reason for its validity within the Drude regime can be understood from the planar surface plasmon dispersion relation [57], $k^2 = (\omega^2/c^2)[\epsilon_m\epsilon_s/(\epsilon_m + \epsilon_s)]$, with dielectric function of metal ϵ_m and its surrounding ϵ_s. The planar surface plasmon dispersion relation (solid line) is linear and follows the light line (dashed line) of $k = \omega/c\sqrt{\epsilon_s}$ with a difference in k-vector $< 1\%$ for wavelength $\gtrsim 2$ μm at a gold and KBr interface [201, 222, 36]. The deviation of the surface plasmon dispersion and the light line becomes significant for $\lambda > 2\mu$m, which is a cutoff wavelength shown as the red line in Fig. 6.10. The propagation loss is also small in the IR with negligible effect on the resonance peak position. Only when the wavelength scaling becomes nonlinear, Eq. (6.7) begins to fail and Babinet's principle starts to break down.

To verify Babinet's principle, we compare the slot antenna length scaling with its complementary rod antenna. The complementary Au rod antenna on KBr has been previously measured to be $\lambda_{\text{eff}} = (0.68 \pm 0.06)\lambda$ [165], which agrees well with our measured result $\lambda_{\text{eff}} = (0.64 \pm 0.05)\lambda$. For a similar rod antenna on a Si substrate the effective wavelength was measured to be $\lambda_{\text{eff}} = (0.32 \pm 0.05)\lambda$ [72, 40], consistent with that of slot antenna on Si with $\lambda_{\text{eff}} = 0.35\lambda$ from Eq. (6.7).

Beyond far-field spectra our near-field imaging on the slot antenna resolved the $n = 1$ and $n = 3$ modes. Through simulation the electric near-field and its spatial distribution of the slot E_2 is found to correspond to the magnetic distribution B_1 of the rod and is related through the duality relation $B_1 = -E_2/c$. This result quantitatively verifies that the magnetic field profile of a rod antenna can be determined by measuring the electric field distribution of a slot antenna. For example, for an incident field strength $E_0 \sim 10^6$ V/m, we achieve a maximum electric field $E_2 \sim 2 \times 10^7$ V/m at the center of slot at the fundamental resonance, corresponding to a maximum

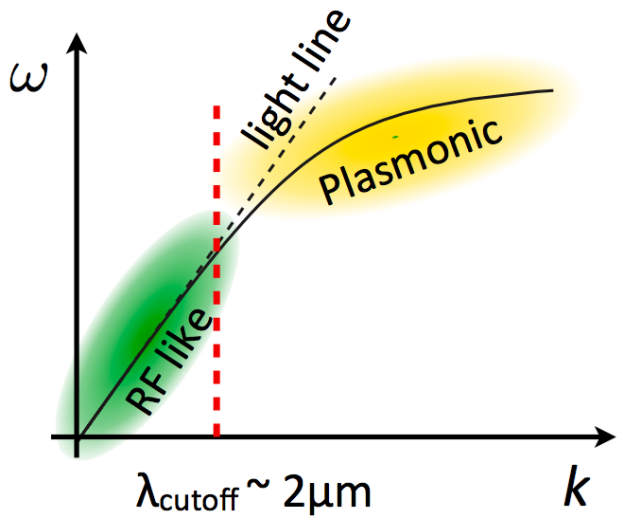

Figure 6.10: The dispersion relation of planar surface plasmon at the gold and KBr interface (solid line) is plotted together with the light line (dashed line). The planar surface plasmon dispersion relation is approximately linear and follows the light line at low frequency, but starts to deviate for wavelength > 2 μm. The linear dispersion relation indicates the gold antenna resonance scales the same as a perfectly conducting antenna. Thus gold antennas at low frequency can meet the requirements of Babinet's principle. However, the plasmon dispersion relation starts to become nonlinear for wavelength < 2 μm, when the deviation from Babinet's principle will be seen. This cutoff wavelength is marked by the vertical red line. Note: the Ohmic loss in metal causes broadening of the resonance, but does not significantly shift the resonance peak position.

magnetic field $B_1 \sim 0.06$ Tesla for the complementary rod resonance.

6.6 Conclusion

In summary, the combination of far-field spectroscopy with near-field imaging quantifies the validity of Babinet's principle for Drude metals and wavelength $\gtrsim 2$ μm. Using Babinet's principle, we demonstrate a general method of probing the optical magnetic field from the study of the electric field of a complementary structure. This method of measuring the magnetic near-field and the resonance scaling provides an improved way to characterize optical antennas and metamaterials and to understand the magnetic light-matter interaction at the nanoscale.

Chapter 7

Resonant optical gradient force for nano-imaging and -spectroscopy

The optical gradient force provides for optomechanical interactions, for particle trapping and manipulation, as well as for near-field optical imaging in scanning probe microscopy. Based on recent experiments, its extension and use for a novel form of optical nanoscale spectroscopy was proposed.

In this chapter, I provide the theoretical basis in terms of spectral behavior, resonant enhancement, and distance dependence of the optical gradient force from numerical simulations for a coupled nanoparticle model geometry. I show that the optical gradient force is dispersive for local electronic and vibrational resonances, yet can be absorptive for collective polaronic excitations. This spectral characteristics together with the distance dependence provide the key characteristics for its measurement and distinction from competing processes such as thermal expansion. Furthermore, I provide a perspective for resonant enhancement and control of optical forces in general.

7.1 Introduction

The combination of scanning probe microscopy with optics provides optical spectroscopy with nanometer spatial resolution. Under light illumination, the induced coupled optical polarization between scanning probe and sample forms the basis of scanning near-field optical microscopy (SNOM) [23, 231], with the near-field signal typically detected by far-field scattering. The coupled optical polarization is expected to also give rise to an optical gradient force between the tip and the sample as illustrated in Fig. 7.1a [52, 168].

Optically induced forces, associated with gradient, scattering, and thermal expansion, have been studied in scanning probe microscopy for topographic and near-field optical imaging with focus on the spatial dependence, as well as for particle trapping and manipulation often exploring the plasmonic resonance of metal particles [168, 166]. In scanning probe microscopy, the optically induced forces, as competing factors to the van der Waals force, have been studied in the context of topographic artifact in SNOM imaging [82, 236, 139, 89, 58, 125]. Used as the signal of interest in itself, the nanomechanical detection of the optically induced forces has also enabled an alternative to photon detection for near-field optical imaging [52, 155, 220, 2, 170]. In addition, a trapped particle as a probe was used for near-field optical or force mapping in photonic force microscopy [79, 213, 68, 157]. However, despite several theoretical studies [167, 34, 134, 10, 168, 104], these works provided limited insight into the spectral characteristics of the optical gradient force and its dependence on electronic and vibrational material resonances of the sample. While the frequency dependence of the optically induced force is often explored in optical trapping of micro/nano-particles [227, 187, 221, 38, 166, 156, 19, 94], and in optically induced mechanical response of plasmonic structures [137, 158], the extension for spectroscopic nano-imaging was not explored.

Recently, the concept of using the optical gradient force for scanning probe optical spectroscopy was proposed based on empirical experimental observations [191, 192]. However, exper-

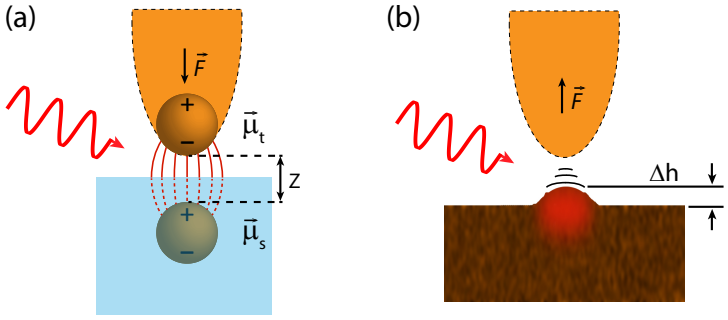

Figure 7.1: (a) Optical gradient force induced by excitation of coupled optical polarization between tip (μ_t) and sample (μ_s), with resulting force $F \propto \mu_t \mu_s$. (b) The optical excitation is accompanied by absorption, with the resulting thermal expansion Δh gives rise to a competing force reaction of the AFM tip.

imental efforts on measuring the optical near-field gradient force have not been conclusive. For example, a force image of a metal bowtie antenna on resonance at $\lambda = 1550$ nm was interpreted to result from an optical gradient force [126]. In contrast, similar force images on gold split ring resonators were attributed to thermal expansion [118]. For molecular electronic resonance spectroscopy an absorptive response was observed and attributed to the optical gradient force [191, 107], in marked contrast to the predictions in this work of a dispersive spectral response. In addition, a nearly instantaneous (few ps) response from ultrafast experiments [108] and polarization dependence in imaging plasmonic particles [102] showed characteristics of the expected optical gradient force behavior. However, both experiments lacked spectroscopic information which would be desirable for a unique assignment. The situation is equally confusing regarding theory. Most studies so far have treated both tip and sample as point dipoles [191, 107], even at close proximity where the dipole approximation fails, or only calculated the distance dependence of the force without considering its spectral response [47]. This leaves key questions open on experimental feasibility and distinguishing spectral characteristics.

Here, I numerically calculate the optical gradient force between a scanning tip and different types of sample materials across their resonances. I predict the spectral behavior of the optical gradient force based on a coupled nano-particle model geometry using Maxwell's stress tensor. The spectroscopic response of the optical gradient force is found to be dispersive for molecular electronic or vibrational and other single particle excitations, in contrast to recent experimental claims of gradient force nano-spectroscopy [191, 107]. I find that only collective polariton resonances can give rise to absorptive spectral force profile. The effect is distinct from the accompanying thermal expansion due to optical absorption (Fig. 7.1b), which results in absorptive resonance spectra in all cases [46, 45, 143]. While the optical gradient force off-resonance is below the thermal cantilever noise limit in a room temperature AFM, with resonance enhancement the force should be detectable with improved force detection or under cryogenic conditions, as established in cavity opto-mechanics [7].

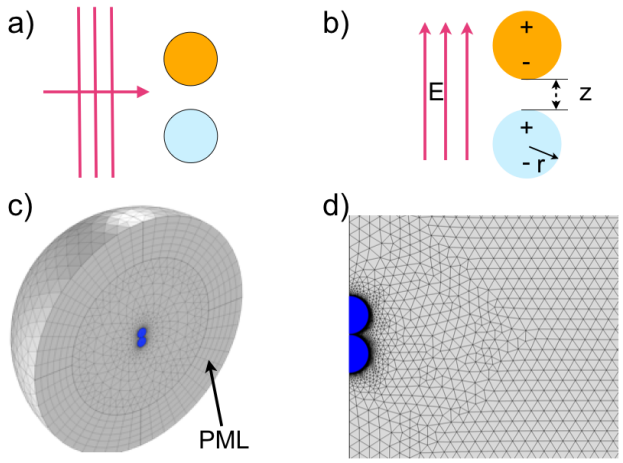

Figure 7.2: (a) The tip and sample are simulated as two finite spheres under plane wave illumination with vertical polarization. (b) The two spheres with radius r are separated by distance z. When the system size is much smaller than the wavelength $r, z \ll \lambda$, such that retardation can be neglected, the electromagnetic problem in (a) can be treated in electrostatic approximation. (c) 3D model for (a) with a cross-sectional view. The two spheres are blue colored. Plane wave at the boundary is terminated with perfectly matched layer (PML). (d) After using rotational symmetry along the axis of the two spheres, the 3D problem can be simplified to 2D problem. The figure shows the cross-section of the rotation plane. The region of the two spheres are colored.

7.2 Numerical simulation

The optical gradient force between the tip and sample can be calculated from a surface integral of the Maxwell stress tensor T_{ij} using finite element electromagnetic simulation (COMSOL Multiphysics). The force on the tip is given by

$$F_i = \sum_j \int_S T_{ij} n_j ds \tag{7.1}$$

with tip surface S, surface normal $\mathbf{n}$, and

$$T_{ij} = \epsilon_0 \left(E_i E_j - \frac{1}{2}|E|^2 \delta_{ij} \right) + \frac{1}{\mu_0} \left(B_i B_j - \frac{1}{2}|B|^2 \delta_{ij} \right). \tag{7.2}$$

The finite element method solves boundary problems (e.g., Maxwell's equations) by dividing the domain of interest into a finite number of small elements. A brief introduction to finite element method can be found in the appendix. Since the radius of tip apex $r \simeq 10$ nm is much smaller than the laser wavelength λ, the near-field tip and sample interaction under plane wave illumination can be analyzed in the quasistatic approximation by assuming the probe to be a polarizable sphere

with radius r. The resulting field distribution on the sample can be effectively reduced to an image sphere of radius r, as shown in Fig. 7.1a. As simulation in 3D is computationally intensive, I made use of several approximation/symmetry techniques to reduce the computation cost without sacrificing physical accuracy:

(1) Electrostatic approximation. As shown in Fig. 7.2 (a,b), if the dimension of the system is small compared to the wavelength ($r, z \ll \lambda$), retardation effect can be neglected, and an electrostatic configuration (b) can be used to approximate the electromagnetic wave problem (a). Since the radius of tip apex $r \approx 10$ nm is much smaller than the laser wavelength λ, this approximation is valid. Under the electrostatic approximation, Maxwell's equation with time harmonic field can be reduced to the Helmholtz equation

$$\nabla \times (\nabla \times \mathbf{E}) - k_0^2 \left(\epsilon + \frac{i\sigma}{\omega \epsilon_0} \right) \mathbf{E} = 0 \tag{7.3}$$

(2) Dimension reduction. The 3D problem is computationally intensive, especially for small gaps where a dense mesh is needed due to the highly non-uniform local electromagnetic field. For example, for sphere size $r = 10$ nm with gap size of $z = 1$ nm, mesh size of 0.2 nm or smaller is required. The 3D simulation often becomes impractical for a single computer to solve [141, 70, 228]. Considering incident polarization along the tip axis, rotational symmetry along the z-axis allows simulation in reduced dimension to decrease the computational complexity (d).

This coupled nanoparticle geometry has been used extensively and with great success predicting general behaviors accurate to within order of magnitude [166, 38, 168]. While the exact geometry of tip and sample affects both the details of magnitude and spectral response of the optical gradient force, especially for strong polaritonic resonances, the limiting case of two finite spheres provides enough general insight into the spectral variation of the force spectrum and its distance dependence.

For the field simulation, a dense mesh with element size of 0.2 nm or less is applied near the spheres, and the distant surrounding is meshed with maximum element size of 20 nm, as shown in

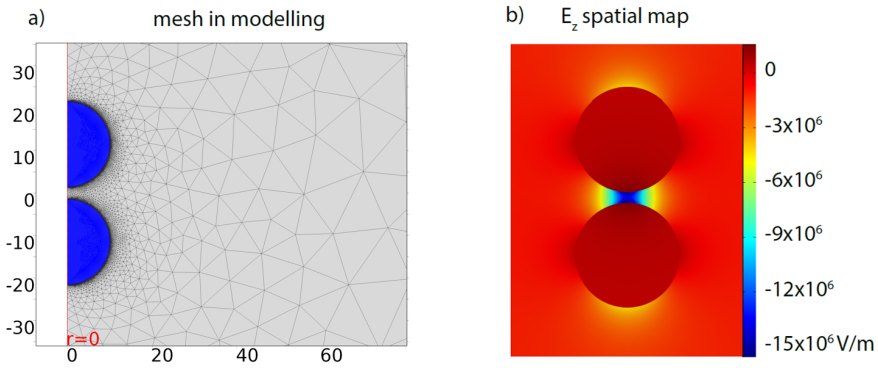

Figure 7.3: (a) Numerical model of two silver spheres under a uniform E field aligned in z direction. Rotational symmetry of the geometry has been employed to reduce the calculation into a 2-D problem. Very fine mesh size of 0.2 nm is used for the area around the two spheres. (b) Simulated electric field distribution around the two spheres, with radius $r = 10$nm and gap size of 2 nm. The background electric field is $E = 10^6$ V/m assuming a focused laser intensity of $I = 133\,\mathrm{kW/cm^2}$. The dielectric function of silver at $\lambda = 500$ nm is taken from the ellipsometry measurement in this thesis, with value $\epsilon_{\mathrm{Ag}} = -9.37 + i0.32$.

Fig. 7.3 (a). A uniform electric field $E = 10^6$ V/m along the z direction is applied. This electric field corresponds to an average laser intensity of $I_0 = 1.33$ mW/μm^2 as used under typical experiment conditions [191, 21].

We consider two types of resonant processes of the sample: i) single particle molecular electronic and vibrational resonances, and ii) collective plasmonic resonances. The results are readily generalizable to samples with other types of resonances including phonons, excitons, and related polaritons. For the case of an electronic resonance, a sample consisting of Rhodamine 6G (R6G) dye molecules is modeled as a single harmonic oscillator for its dielectric function $\epsilon(\omega) = \epsilon_1(\omega) + i\epsilon_2(\omega)$, with transition energy of 2.42 eV, and line width of 0.41 eV, as a best fit to experimental results. A tungsten tip with $r = 10$ nm is used to ensure a flat spectral response of the tip in the relevant visible spectral region. For the molecular vibrational resonance, a gold tip sphere is used to interact with a sample sphere (both with $r = 10$ nm) of poly(methyle methacrylate) (PMMA) with characteristic carbonyl resonance (C=O) at 1729 cm^{-1}. Finally, to study the case of plasmonic resonance, two silver spheres of $r = 10$ nm are modeled as the tip and sample system.

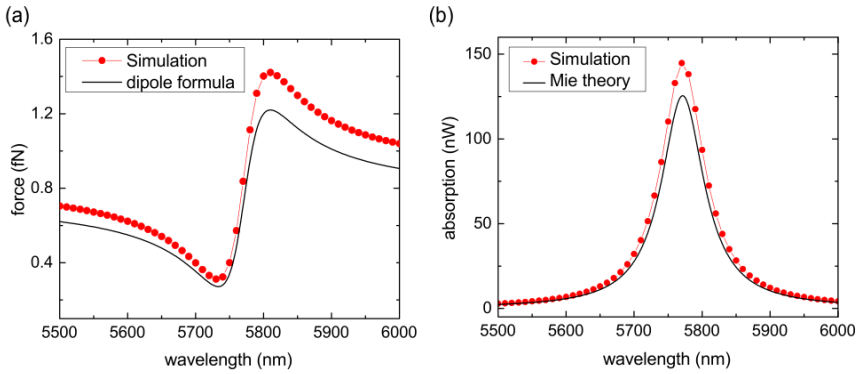

Figure 7.4: (a) Numerical calculation of force spectrum of a PMMA sphere and gold sphere (red dot), in comparison with dipole formula (black solid line). Sphere radius $r = 30$ nm, separation $z = 30$ nm, electric field $E = 10^6$ V/m. (b) Simulated absorption, in comparison with a isolated PMMA sphere calculated with Mie theory. The agreement is excellent.

7.2.1 Verification of numerical simulation

To verify the accuracy of my numerical simulation, I compare the simulation against known analytical results. For cases when the two spheres are well separated with $z > 2r$, the optical gradient force can be expressed analytically as the dipole-dipole interaction assuming two independently polarized spheres. The resulting force is proportional to the polarizability of the tip and sample spheres (α_t and α_s) [168],

$$\langle F \rangle = -\frac{1}{2}\mathbf{Re}\left[\frac{1}{4\pi\epsilon_0}\frac{6\alpha_t\alpha_s^* E^2}{z^4}\right] \propto \mathbf{Re}(\alpha_t\alpha_s^*)\frac{E^2}{z^4}. \tag{7.4}$$

Fig. 7.4a shows the comparison of the simulated spectrum (red symbol) of optical gradient force with result of the analytical expression (black solid) from Eq. 7.4 for a gold sphere and a PMMA sphere of radius $r = 30$ nm separated by $z = 30$ nm. In addition, I also compared the simulated absorption spectrum to an absorption spectrum calculated by Mie theory of an isolated PMMA sphere in (b). The good agreement of my simulations with analytical results validates the numerical accuracy.

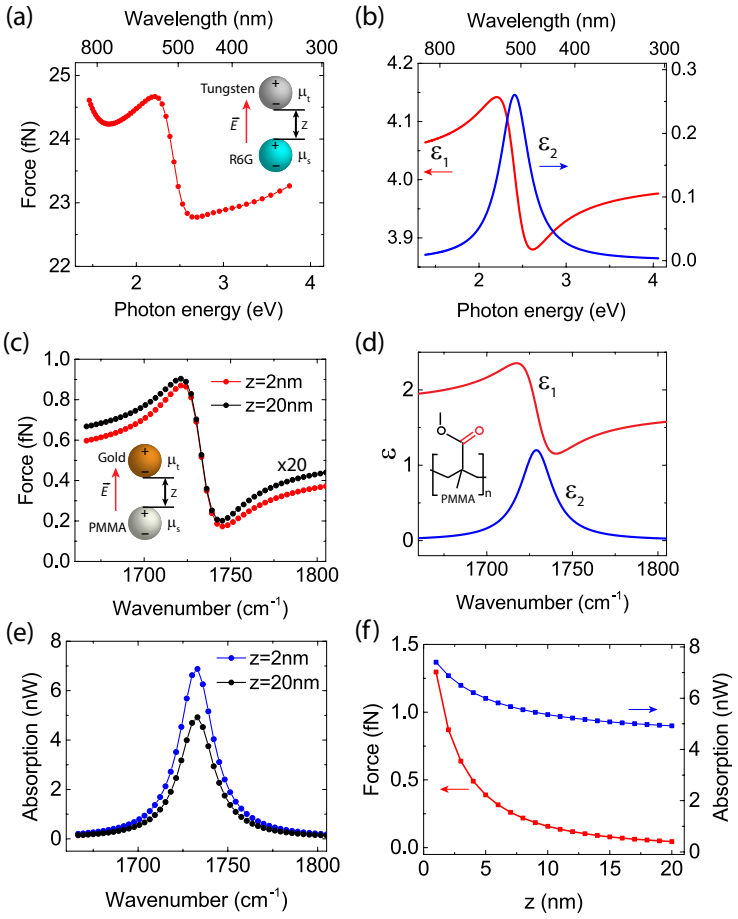

Figure 7.5: (a) Electronic resonant force spectrum between a tungsten tip and R6G sample (both of radius $r = 10$ nm) subject to an optical field $E = 10^6$ V/m, separated by $z = 2$ nm. (b) Dielectric function of R6G $\epsilon(\omega) = \epsilon_1(\omega) + i\epsilon_2(\omega)$ modeled as a single harmonic oscillator. (c) Corresponding force spectra between a gold sphere and PMMA sample of radii $r = 10$ nm. Dispersive force spectrum at separation distance $z = 20$ nm (multiplied by 20, black) compared to force spectrum at $z = 2$ nm (red). (d) Dielectric function of PMMA $\epsilon(\omega) = \epsilon_1(\omega) + i\epsilon_2(\omega)$ around the carbonyl resonance at 1729 cm^{-1}. (e) Simulated PMMA absorption at distances $z = 20$ nm (black) and $z = 2$ nm (blue). (f) The distance dependence of the optical force (red) on resonance shows a complex distance scaling, neither following simple dipole-dipole power law nor exponential scaling. The slight increase of optical absorption (blue) is due to local field enhancement in the gap region.

7.3 Results

Fig. 7.5a shows the resulting force spectrum between the tungsten tip and R6G sample at a distance of $z = 2$ nm. The force spectrum is dispersive, and follows the trend of the real part of the dielectric function $\epsilon_1(\omega)$ shown in Fig. 7.5b. The relatively small force variation between 23 fN

to 25 fN across the resonance is due to the large broadband offset as a result of $\epsilon_1 \gg \epsilon_2$, which is a characteristic property of the dielectric function for molecular electronic resonances.

Correspondingly, Fig. 7.5c shows the force spectrum of the Au sphere interacting with the carbonyl vibrational resonance of PMMA at separation of $z = 20$ nm (black). The force increases by 20 times in magnitude to a peak value of $F \approx 1$ fN when decreasing the distance to $z = 2$ nm (red). Due to the smaller vibrational dipole moment compared to the electronic counter part, the force is much weaker than in the case of R6G but exhibits a larger relative spectral variation across the resonance from 0.2 fN to 1 fN (for $z = 2$ nm). Irrespective of distance, and similar to the electronic resonance case, the force spectra are dispersive and follow the real part of the dielectric function of PMMA $\epsilon_1(\omega)$ (Fig. 7.5d). For comparison, Fig. 7.5e shows the absorption spectra at $z = 20$ nm and $z = 2$ nm in black and blue, respectively. In contrast to the force spectra, the absorption spectra show the well known symmetric resonance behavior corresponding to the imaginary part of the dielectric function $\epsilon_2(\omega)$. Except for a change in magnitude, peak position and line shape of both optical gradient force and absorption spectra are invariant with respect to tip-sample distance. The distance dependence of the optical force on resonance (red) is shown in Fig. 7.5f. Due to increasing multipole contributions with decreasing distance, the distance scaling follows neither simple exponential nor power law, and is far more shallow than what one would expect based on a simple dipole-dipole interaction ($\propto z^{-4}$). The magnitude of absorption (blue) only increases slightly due to local field enhancement with decreasing distance.

Fig. 7.6a shows the force spectrum of two silver spheres ($r = 10$ nm) separated by $z = 20$ nm for an applied optical field of $E = 10^6$ V/m. The slight asymmetric plasmonic resonant force spectrum peaks at 3.5 eV with $F_{\max} \simeq 30$ fN. For comparison, Fig. 7.6b shows the absorption spectrum for the two silver spheres. The normalized complex polarizability of a silver sphere $\bar{\alpha} = (\epsilon_{\mathrm{Ag}} - 1)/(\epsilon_{\mathrm{Ag}} + 2)$ is shown in the inset. As can be seen, both optical gradient force and absorption spectra follow the imaginary part of polarizability $\mathbf{Im}(\bar{\alpha})(\omega)$.

Fig. 7.7a shows the spectral evolution of the force as a function of distance. When the separation of the two spheres decreases from $z = 20$ nm to $z = 1$ nm, the optical gradient force

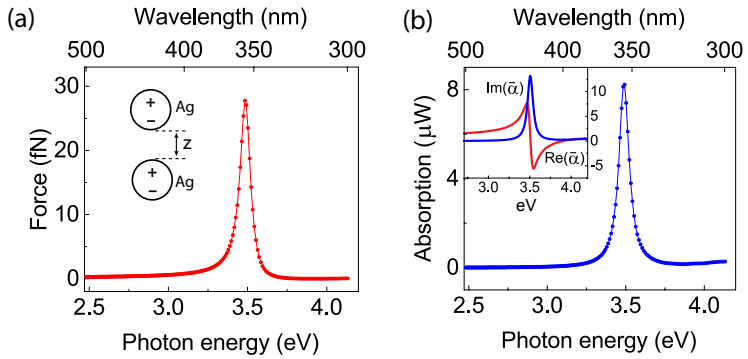

Figure 7.6: (a) Optical gradient force spectrum of two silver spheres with radius $r = 10$ nm separated by $z = 20$ nm subject to external optical field $E = 10^6$ V/m. (b) Absorption spectrum of the two spheres with symmetric resonance at 3.5 eV. Inset: real and imaginary part of the normalized polarizability $\bar{\alpha} = (\epsilon_{\rm Ag} - 1)/(\epsilon_{\rm Ag} + 2)$ for a silver sphere. Force and absorption spectra follow the imaginary part of $\bar{\alpha}(\omega)$.

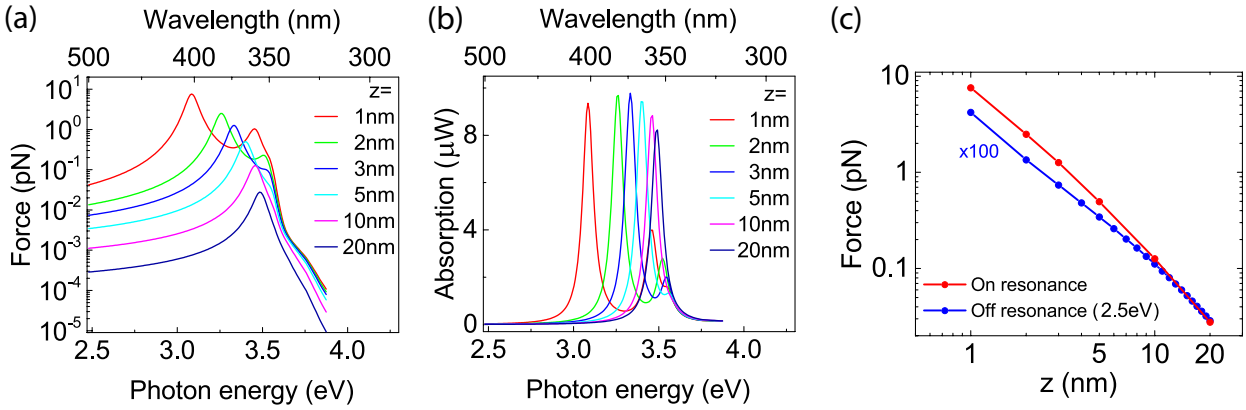

Figure 7.7: Simulated optical gradient force (a) and absorption (b) spectra for two silver spheres of $r = 10$ nm at different separations. The peak magnitude of optical force on resonance increases by a factor $\sim 10^3$ from $z = 20$ nm to $z = 1$ nm. Meanwhile the resonance of the force spectrum red shifts due to plasmonic coupling. In comparison, the magnitude of the corresponding absorption spectra has no significant distance dependence. (c) The optical gradient force, both on-resonance (red) and off-resonance (blue), follows a power law distance dependence on z.

increases by a factor of $\sim 10^3$ reaching $F \approx 10$ pN. Correspondingly, the resonance frequency of the force spectrum red-shifts due to the plasmonic coupling between the two spheres [198]. In contrast, the magnitude of optical absorption does not change significantly with separations as shown in Fig. 7.7b. The distance dependence of the optical gradient force on- (red) and off-resonance (blue) is plotted in Fig. 7.7c. Both increase with decreasing distance approximately following a power law $\propto z^n$, with $n \approx -2$, i.e., again less steep than the point dipole z^{-4} dependence.

7.4 Discussion

The different spectral behaviors of the optical gradient force can be rationalized based on the dipole-dipole interaction assuming two independently polarized spheres when $z > 2r$, with resulting force proportional to the polarizability [168], $\langle F \rangle \propto \mathbf{Re}(\alpha_t \alpha_s^*)$. For a non-resonant tip, the force simplifies to $F \propto \mathbf{Re}(\alpha_s)$, describing the dispersive force spectra for a tungsten tip and a R6G sample in the visible, and a gold tip and a PMMA sample in the infrared. In general, a dispersive line shape is spectrally broader than an absorptive line shape, thus making the optical gradient force spectra extending more outside of resonance than corresponding absorption spectra. It is interesting to note that the optical gradient force can in principle also become repulsive for $\mathbf{Re}(\alpha_s)$ crossing zero. When tip and sample consist of the same material (e.g., silver), the force spectrum is proportional to the square of the polarization, i.e., $F \propto \mathbf{Re}(\alpha_t \alpha_s^*) \propto |\alpha_{\mathrm{Ag}}|^2$, and is absorptive when $\mathbf{Re}(\alpha_{\mathrm{Ag}})$ crosses zero as for the case for the two plasmonic silver spheres.

As shown above in Fig. 7.7c, the optical gradient force based on a collective plasmonic resonance can reach few pN. The force based on a single particle excitation in the form of a molecular resonance is weaker by three orders of magnitude (few fN) under similar tip-sample geometric conditions. In the following we address the question of AFM sensitivity for its possible detection and distinction from thermal expansion. The sensitivity of force detection in AFM is limited by thermal fluctuations of the cantilever [148, 81]. The smallest detectable force is when the cantilever oscillation amplitude equals that induced by thermal noise given by

$$F_{\mathrm{min}} = \left[\frac{4k_B T k B}{\omega Q}\right]^{1/2}, \tag{7.5}$$

with Boltzmann constant k_B, temperature T, spring constant k, detection bandwidth B, and Q factor of the cantilever. The minimal detectable force gradient due to a change in sample-tip interaction operating in non-contact mode can also be derived as [148, 81]

$$F'_{\mathrm{min}} = \frac{1}{A_0}\sqrt{\frac{27k_B T k B}{\omega Q}}, \tag{7.6}$$

with cantilever oscillation amplitude A_0. Using typical values from force detection experiments

[191, 126, 192, 142, 143], we get $F_{\min} \approx 0.3$ pN ($T = 300$ K, $k = 3$ N/m, $B = 10$ Hz, $\omega \approx 500$ kHz, $Q \approx 100$) and $F'_{\min} \approx 0.03$ pN/nm ($A_0 = 10$ nm, $T = 300$ K, $k = 3$ N/m, $B = 10$ Hz, $\omega \approx 500$ kHz, $Q \approx 100$). This makes collective particle excitation induced force detectable under typical laser intensities below the sample damage threshold. In contrast force detection due to molecular electronic and vibrational resonance is two orders of magnitude below the detection limit of conventional room temperature AFM. We can also compare the optical gradient force to the van der Waals force, which has a $1/z^7$ distance dependence in comparison to the $1/z^4$ of optical gradient force. The optical gradient force is typically weaker than the van der Waals force at short distances, however, under plasmonic resonances the optical gradient force can exceed the van der Waals force [94, 38].

The effect due to thermal expansion Δh can be estimated based on $\Delta h = \alpha_T \Delta T$ [143]. Assuming a sample thickness of 10 nm, typical thermal expansion coefficients $\alpha_T = 10^{-4} - 10^{-5}$/K, and a sample temperature increase of a few K after laser illumination [58, 143], we get a thermal expansion value of $\Delta h = 0.1$ – 100 pm. When this expansion of the sample is modulated at a resonance frequency of the cantilever, the corresponding force becomes $F_{\text{thermal}} = k\Delta h \times Q$, where k is the cantilever spring constant of typically 3 N/m, and Q =100 – 200. The resulting force is in the range of $F_{\text{thermal}} = 10$ pN – 1 nN. Thus the thermal expansion effect can readily be measured with AFM as shown experimentally even down to monolayer sensitivity with a single chemical bond expansion of few pm [143].

In previous attempts to detect the optical gradient force, a large force magnitude of $F \sim 2$ pN and an excellent agreement of the force spectrum with the far-field molecular absorption spectrum [191, 107] strongly suggest that the observed experimental results were in fact due to thermal expansion and not due to the optical gradient force as claimed. Optical gradient force detection has also been assigned to the force contrast on bowtie antennas reaching few pN on resonance [126]. This assignment is feasible in principle according to our predictions. However, a force due to thermal expansion of similar magnitude is expected, leaving the underlying mechanism of the imaging contrast unclear.

In practice, the differences both in distance dependence and spectral frequency dependence of the optical gradient force and thermal expansion can be used to differentiate the two mechanisms. Notably, the optical gradient force is a longer range effect, determined by the spatial extent of the near-field of the tip apex, and thus follows a continuous change with distance as determined by the tip radius (Fig. 7.5f and Fig. 7.7c). In contrast, the force exerted on the tip through sample expansion requires a direct physical tip-sample contact, and should decay on even sub-nm distances above the sample, independent of tip radius.

A way to differentiate the two mechanisms in imaging plasmonic optical antennas is to map the spatial force distribution. The optical force is proportional to the local optical electric field, while the thermal expansion/absorption is due to resistive heating associated with electric currents. Thus distinct spatial maps result for the two different mechanisms since the current distribution peaks at the positions of minima in the electric field in optical antennas [178].

Fundamentally, the optical gradient force due to optical polarization and thermal expansion due to energy dissipation are two dynamic processes occurring on different time scales. This provides an additional opportunity for their distinction. Optical polarization with coherent excitation is induced nearly instantaneously in the fs to ps range, as determined by the spectral line width. In contrast, thermalization of an optical excitation underlying optical absorption leads to thermal expansion on ns time scales.

7.5 Conclusion and outlook

In summary, the dispersive line shape in probing electronic and vibrational materials resonances as related to the real part of the dielectric function of the sample can serve as a distinguishing attribute in optical gradient force spectroscopy. Albeit weak with forces in the fN to pN range, their detection with advanced atomic force microscopy techniques can provide a novel form of optical scanning probe nano-imaging and -spectroscopy. The magnitude of the force can be increased by exploring the resonance enhancement with sharp gradient on resonance, such as slow light and electromagnetically induced transparency. The gradient force spectroscopy can also be expanded

to nonlinear and coherent interaction with multiple light fields.

Compatible with a wide range of spectroscopies, including coherent and ultrafast techniques, the optical gradient force spectroscopy can complement related all-optical scattering scanning near-field optical microscopy (s-SNOM). Our calculation provides a guidance of the key parameters of strength, distance dependence, and spectral behavior for a simplified tip geometry, yet can readily be extended to specific tip geometries and other optical processes, including inelastic, *e.g.*, Raman, as well as nonlinear excitations.

Chapter 8

Conclusion and outlook

In this thesis I explored fundamental properties of light-matter interactions in the near-field. The first two chapters cover the concepts of near-field optics and the theoretical background.

In chapter 3, the optical dielectric functions of one of the most common plasmonic materials – silver is measured with ellipsometry, and analyzed with the Drude model over a broad spectral range from visible to mid-infrared. This work was motivated by the need for accurate values for a wide range of applications of silver in plasmonics, optical antennas, and metamaterials. This measurement provides a reference for dielectric functions of silver.

Chapter 4 and 5 describe the infrared *s*-SNOM instruments I developed for spectroscopic nano-imaging at both room temperature and low temperature. As one of the first cryogenic *s*-SNOM instruments, the novel design concept and key specifications are discussed. Initial low-temperature and high-temperature performances of the instrument are examined by imaging of optical conductivity of vanadium oxides (VO_2 and V_2O_3) across their phase transitions. The spectroscopic imaging capability is demonstrated on chemical vibrational resonances of Poly(methyl methacrylate) (PMMA) and other samples.

Chapter 6 explores imaging of optical magnetic fields. As a proof-of-principle, the magnetic near-field response of a linear rod antenna is studied with Babinet's principle. Babinet's principle connects the magnetic field of a structure to the electric field of its complement structure. Using combined far- and near-field spectroscopy, imaging, and theory, I identify magnetic dipole and higher order bright and dark magnetic resonances at mid-infrared frequencies. From resonant

length scaling and spatial field distributions, I confirm that the theoretical requirement of Babinet's principle for a structure to be infinitely thin and perfectly conducting is still fulfilled to a good approximation in the mid-infrared. Thus Babinet's principle provides access to spatial and spectral magnetic field properties, leading to targeted design and control of magnetic optical antennas.

Lastly in chapter 7, a novel form of nanoscale optical spectroscopy based on mechanical detection of optical gradient force is explored. It is to measure the optical gradient force between induced dipole moments of a sample and an atomic force microscope (AFM) tip. My study provides the theoretical basis in terms of spectral behavior, resonant enhancement, and distance dependence of the optical gradient force from numerical simulations for a coupled nanoparticle model geometry. I show that the optical gradient force is dispersive for local electronic and vibrational resonances, yet can be absorptive for collective polaronic excitations. This spectral behavior together with the distance dependence scaling provides the key characteristics for its measurement and distinction from competing processes such as thermal expansion. Furthermore, I provide a perspective for resonant enhancement and control of optical forces in general.

The results presented in this thesis improve the understanding of light-matter interaction in the near-field as well as provide new optical spectroscopy methods for *in situ* material characterizations. *s*-SNOM and its alternative with force detection opens the opportunity towards optical spectroscopy with single molecule sensitivity. With the development of new light sources, tip engineering, and optical coherent control methods, it is possible to push the near-field optics towards the ultimate limit of femtosecond dynamics with nanometer spatial resolution.

Bibliography

[1] E. Abbe. On the Estimation of Aperture in the Microscope. Journal of the Royal Microscopical Society, 1:388–423, 1881.

[2] M. Abe, Y. Sugawara, K. Sawada, Y. Andoh, and S. Morita. Optical Near-Field Imaging Using the Kelvin Probe Technique. Japanese Journal of Applied Physics, 37:L1074–L1077, 1998.

[3] J. Aizpurua, T. Taubner, F. J. García de Abajo, M. Brehm, and R. Hillenbrand. Substrate-enhanced infrared near-field spectroscopy. Optics Express, 16:1529–45, 2008.

[4] J. W. Allen and J. C. Mikkelsen. Optical properties of CrSb, MnSb, NiSb, and NiAs. Physical Review B, 15:2952–2960, 1977.

[5] P. Allen. Electron-Phonon Effects in the Infrared Properties of Metals. Physical Review B, 3:305–320, 1971.

[6] A. Anderson, K. S. Deryckx, X. G. Xu, G. Steinmeyer, and M. B. Raschke. Few-femtosecond plasmon dephasing of a single metallic nanostructure from optical response function reconstruction by interferometric frequency resolved optical gating. Nano Letters, 10:2519–24, 2010.

[7] G. Anetsberger, O. Arcizet, E. Gavartin, Q. P. Unterreithmeier, E. M. Weig, J. P. Kotthaus, and T. J. Kippenberg. Near-field cavity optomechanics with nanomechanical oscillators. Nature Physics, 5:909–914, 2009.

[8] H. Aouani, O. Mahboub, N. Bonod, E. Devaux, E. Popov, H. Rigneault, T. W. Ebbesen, and J. Wenger. Bright unidirectional fluorescence emission of molecules in a nanoaperture with plasmonic corrugations. Nano Letters, 11:637–44, 2011.

[9] A. April, P. Bilodeau, and M. Piché. Focusing a TM(01) beam with a slightly tilted parabolic mirror. Optics Express, 19:9201–12, 2011.

[10] J. R. Arias-González, M. Nieto-Vesperinas, and M. Lester. Modeling photonic force microscopy with metallic particles under plasmon eigenmode excitation. Physical Review B, 65:115402, 2002.

[11] N. P. Armitage. Electrodynamics of correlated electron systems : Lecture Notes 2008 Boulder summer school on condensed matter physics. arXiv:0908.1126, pages 1–35, 2008.

[12] E. A. Ash and G. Nicholls. Super-resolution aperture scanning microscope. Nature, 237:510–512, 1972.

[13] N. W. Ashcroft and N. D. Mermin. Solid State Physics. Cengage Learning; 1 edition, 1976.

[14] J. M. Atkin, S. Berweger, A. C. Jones, and M. B. Raschke. Nano-optical imaging and spectroscopy of order, phases, and domains in complex solids. Advances in Physics, 61:745–842, 2012.

[15] C. A. Balanis. Antenna Theory: Analysis and Design. John Wiley & Sons, Inc., 1997.

[16] N. Behr and M. B. Raschke. Optical antenna properties of scanning probe tips: Plasmonic light scattering, tip-sample coupling, and near-field enhancement. Journal of Physical Chemistry C, 112:3766–3773, 2008.

[17] H. E. Bennett. Formation and Growth of Tarnish on Evaporated Silver Films. Journal of Applied Physics, 40:3351, 1969.

[18] H. E. Bennett and J. M. Bennett. Optical Properties and Electronic Structure of Metals and Alloys. North-Holland, Amsterdam; Wiley, New York, 1966.

[19] J. Berthelot, S. S. Aćimović, M. L. Juan, M. P. Kreuzer, J. Renger, and R. Quidant. Three-dimensional manipulation with scanning near-field optical nanotweezers. Nature Nanotechnology, 9:295–9, 2014.

[20] S. Berweger. Plasmonic Antennas for Optical Nanocrystallography and Femtosecond Spatio-Temporal Control. PhD thesis, University of Washington, 2011.

[21] S. Berweger, D. M. Nguyen, E. A. Muller, H. A. Bechtel, T. T. Perkins, and M. B. Raschke. Nano-chemical infrared imaging of membrane proteins in lipid bilayers. Journal of the American Chemical Society, 135:18292–5, 2013.

[22] E. Betzig, G. H. Patterson, R. Sougrat, O. W. Lindwasser, S. Olenych, J. S. Bonifacino, M. W. Davidson, J. Lippincott-Schwartz, and H. F. Hess. Imaging intracellular fluorescent proteins at nanometer resolution. Science, 313:1642–5, 2006.

[23] E. Betzig, J. K. Trautman, T. D. Harris, J. S. Weiner, and R. L. Kostelak. Breaking the diffraction barrier: optical microscopy on a nanometric scale. Science, 251:1468–1470, 1991.

[24] A. Bitzer, A. Ortner, H. Merbold, T. Feurer, and M. Walther. Terahertz near-field microscopy of complementary planar metamaterials: Babinet's principle. Optics Express, 19:2537–45, 2011.

[25] M. G. Blaber, A. Henry, J. M. Bingham, G. C. Schatz, and R. P. Van Duyne. LSPR Imaging of Silver Triangular Nanoprisms: Correlating Scattering with Structure Using Electrodynamics for Plasmon Lifetime Analysis. The Journal of Physical Chemistry C, 116:393–403, 2012.

[26] C. F. Bohren and D. R. Huffman. Absorption and Scattering of Light by Small Particles. Wiley-VCH Verlag GmbH, Weinheim, Germany, April 1998.

[27] H. G. Booker. Slot aerials and their relation to complementary wire aerials (Babinet's principle). Journal of the Institution of Electrical Engineers - Part IIIA: Radiolocation, 93:620–626, 1946.

[28] M. Bosman, E. Ye, S. Tan, C. A. Nijhuis, J. K. W. Yang, R. Marty, A. Mlayah, A. Arbouet, C. Girard, and M. Han. Surface plasmon damping quantified with an electron nanoprobe. Scientific Reports, 3:1312, 2013.

[29] R. W. Boyd. Nonlinear Optics. Elsevier, 2010.

[30] G. Brändli and A. J. Sievers. Absolute measurement of the far-infrared surface resistance of Pb. Physical Review B, 5:3550–3557, 1972.

[31] G. W. Bryant, F. J. García de Abajo, and J. Aizpurua. Mapping the plasmon resonances of metallic nanoantennas. Nano Letters, 8:631–6, 2008.

[32] M. Burresi, D. van Oosten, T. Kampfrath, H. Schoenmaker, R. Heideman, A. Leinse, and L. Kuipers. Probing the magnetic field of light at optical frequencies. Science, 326:550–3, 2009.

[33] M. Cazalilla, J. Dolado, A. Rubio, and P. Echenique. Plasmonic excitations in noble metals: The case of Ag. Physical Review B, 61:8033–8042, 2000.

[34] P. C. Chaumet and M. Nieto-Vesperinas. Time-averaged total force on a dipolar sphere in an electromagnetic field. Optics Letters, 25:1065–1067, 2000.

[35] J. Chen, M. Badioli, P. Alonso-González, S. Thongrattanasiri, F. Huth, J. Osmond, M. Spasenović, A. Centeno, A. Pesquera, P. Godignon, A. Zurutuza Elorza, N. Camara, F. J. García de Abajo, R. Hillenbrand, and F. Koppens. Optical nano-imaging of gate-tunable graphene plasmons. Nature, 487:77–81, 2012.

[36] Y. Chen, Z. Song, Y. Li, M. Hu, Q. Xing, Z. Zhang, L. Chai, and C. Wang. Effective surface plasmon polaritons on the metal wire with arrays of subwavelength grooves. Optics Express, 14:13021, 2006.

[37] N. E. Christensen. The Band Structure of Silver and Optical Interband Transitions. Physica Status Solidi (b), 54:551–563, 1972.

[38] P. Chu and D. L. Mills. Laser-induced forces in metallic nanosystems: The role of plasmon resonances. Physical Review Letters, 99:127401, 2007.

[39] R. D. Cowan. The Theory of Atomic Structure and Spectra. University of California Press, 1981.

[40] K. B. Crozier, A. Sundaramurthy, G. S. Kino, and C. F. Quate. Optical antennas: Resonators for local field enhancement. Journal of Applied Physics, 94:4632, 2003.

[41] X. Cui, C. Wang, A. Argondizzo, S. Garrett-Roe, B. Gumhalter, and H. Petek. Transient excitons at metal surfaces. Nature Physics, 10:505–509, 2014.

[42] A. Cvitkovic, N. Ocelic, and R. Hillenbrand. Analytical model for quantitative prediction of material contrasts in scattering-type near-field optical microscopy. Optics Express, 15:8550–65, 2007.

[43] S. Dai, Z. Fei, Q. Ma, A. S. Rodin, M. Wagner, A. S. McLeod, M. Liu, W. Gannett, W. Regan, K. Watanabe, T. Taniguchi, M. Thiemens, G. Dominguez, A. H. Castro Neto, A. Zettl, F. Keilmann, P. Jarillo-Herrero, M. M. Fogler, and D. N. Basov. Tunable phonon polaritons in atomically thin van der Waals crystals of boron nitride. Science, 343:1125–9, 2014.

[44] S. Dai, Q. Ma, T. Andersen, A. S. Mcleod, Z. Fei, M. Liu, M. Wagner, K. Watanabe, T. Taniguchi, M. Thiemens, F. Keilmann, P. Jarillo-Herrero, M. M. Fogler, and D. N. Basov. Subdiffractional focusing and guiding of polaritonic rays in a natural hyperbolic material. Nature Communications, 6:6963, 2015.

[45] A. Dazzi, C. B. Prater, Q. Hu, D. B. Chase, J. F. Rabolt, and C. Marcott. AFM-IR: Combining Atomic Force Microscopy and Infrared Spectroscopy for Nanoscale Chemical Characterization. Applied Spectroscopy, 66 N62:1365–1384, 2012.

[46] A. Dazzi, R. Prazeres, F. Glotin, and J. M. Ortega. Local infrared microspectroscopy with subwavelength spatial resolution with an atomic force microscope tip used as a photothermal sensor. Optics Letters, 30:2388–2390, 2005.

[47] F. De Angelis, R. P. Zaccaria, and E. Di Fabrizio. Mapping the local dielectric response at the nanoscale by means of plasmonic force spectroscopy. Optics Express, 20:29626–33, 2012.

[48] R. de L. Kronig. The Quantum Theory of Dispersion in Metallic Conductors. Proceedings of the Royal Society A: Mathematical, Physical and Engineering Sciences, 124:409–422, 1929.

[49] R. de L. Kronig. The Quantum Theory of Dispersion in Metallic Conductors. II. Proceedings of the Royal Society A: Mathematical, Physical and Engineering Sciences, 133:255–265, 1931.

[50] A. Degiron, H. J. Lezec, N. Yamamoto, and T. W. Ebbesen. Optical transmission properties of a single subwavelength aperture in a real metal. Optics Communications, 239:61–66, 2004.

[51] D. Denkova, N. Verellen, A. V. Silhanek, V. K. Valev, P. Van Dorpe, and V. V. Moshchalkov. Mapping magnetic near-field distributions of plasmonic nanoantennas. ACS nano, 7:3168–76, 2013.

[52] F. Depasse and D. Courjon. Inductive forces generated by evanescent light fields: application to local probe microscopy. Optics Communications, 87:79–83, 1992.

[53] P. Dernier and M. Marezio. Crystal Structure of the Low-Temperature Antiferromagnetic Phase of V_2O_3. Physical Review B, 2:3771–3776, 1970.

[54] B. Deutsch, R. Hillenbrand, and L. Novotny. Near-field amplitude and phase recovery using phase-shifting interferometry. Optics Express, 16:494–501, 2008.

[55] B. Dold and R. Mecke. Optische Eigenschaften von Edelmetallen, Übergangsmetallen und deren Legierungen im Infrarot. Optik, 22:435, 1965.

[56] J. Dorfmüller, R. Vogelgesang, W. Khunsin, C. Rockstuhl, C. Etrich, and K. Kern. Plasmonic nanowire antennas: experiment, simulation, and theory. Nano Letters, 10:3596–603, 2010.

[57] J. Dorfmüller, R. Vogelgesang, R. T. Weitz, C. Rockstuhl, C. Etrich, T. Pertsch, F. Lederer, and K. Kern. Fabry-Pérot resonances in one-dimensional plasmonic nanostructures. Nano Letters, 9:2372–7, 2009.

[58] A. Downes, D. Salter, and A. Elfick. Heating effects in tip-enhanced optical microscopy. Optics Express, 14:5216–5222, 2006.

[59] M. Dressel and G. Gruner. Electrodynamics of solids. Cambridge University Press, 2002.

[60] M. Dujardin and M. Thèye. Investigation of the optical properties of Ag by means of thin semi-transparent films. Journal of Physics and Chemistry of Solids, 32:2033–IN1, 1971.

[61] H. Ehrenreich and H. Philipp. Optical Properties of Ag and Cu. Physical Review, 128:1622–1629, 1962.

[62] J. W. Ekin. Experimental Techniques for Low-Temperature Measurements: Cryostat Design, Material Properties, and Superconductor Critical-Current Testing. Oxford University Press, 2006.

[63] C. Enkrich, M. Wegener, S. Linden, S. Burger, L. Zschiedrich, F. Schmidt, J. Zhou, T. Koschny, and C. Soukoulis. Magnetic Metamaterials at Telecommunication and Visible Frequencies. Physical Review Letters, 95:203901, 2005.

[64] F. Falcone, T. Lopetegi, M. Laso, J. Baena, J. Bonache, M. Beruete, R. Marqués, F. Martín, and M. Sorolla. Babinet Principle Applied to the Design of Metasurfaces and Metamaterials. Physical Review Letters, 93:197401, 2004.

[65] Z. Fei, A. S. Rodin, G. O. Andreev, W. Bao, A. S. McLeod, M. Wagner, L. M. Zhang, Z. Zhao, M. Thiemens, G. Dominguez, M. M. Fogler, A. H. Castro Neto, C. N. Lau, F. Keilmann, and D. N. Basov. Gate-tuning of graphene plasmons revealed by infrared nano-imaging. Nature, 487:8285, 2012.

[66] Z. Fei, A. S. Rodin, W. Gannett, S. Dai, W. Regan, M. Wagner, M. Liu, A. S. McLeod, G. Dominguez, M. Thiemens, A. H. Castro Neto, F. Keilmann, A. Zettl, R. Hillenbrand, M. M. Fogler, and D. N. Basov. Electronic and plasmonic phenomena at graphene grain boundaries. Nature Nanotechnology, 8:821–5, 2013.

[67] T. Feng, Y. Zhou, D. Liu, and J. Li. Controlling magnetic dipole transition with magnetic plasmonic structures. Optics Letters, 36:2369–71, 2011.

[68] E. Florin, A. Pralle, J. K. Heinrich Hörber, and E. Stelzer. Photonic Force Microscope Based on Optical Tweezers and Two-Photon Excitation for Biological Applications. Journal of Structural Biology, 119:202–211, 1997.

[69] C. L. Foiles. Metals: Electronic Transport Phenomena, volume 15b of Landolt-Börnstein - Group III Condensed Matter. Springer-Verlag, Berlin/Heidelberg, 1985.

[70] K. T. Fountaine, W. S. Whitney, and H. A. Atwater. Resonant absorption in semiconductor nanowires and nanowire arrays: Relating leaky waveguide modes to Bloch photonic crystal modes. Journal of Applied Physics, 116:153106, 2014.

[71] M. Fox. Optical properties of Solids. Oxford University press, 2010.

[72] C. Fumeaux, M. A. Gritz, I. Codreanu, W. L. Schaich, F. J. González, and G. D. Boreman. Measurement of the resonant lengths of infrared dipole antennas. Infrared Physics & Technology, 41:271–281, 2000.

[73] G. Fuster, J. Tyler, N. Brener, J. Callaway, and D. Bagayoko. Electronic structure and related properties of silver. Physical Review B, 42:7322–7329, 1990.

[74] F. J. García de Abajo. Colloquium: Light scattering by particle and hole arrays. Reviews of Modern Physics, 79:1267–1290, 2007.

[75] A. Garcia-Lekue, J. M. Pitarke, E. V. Chulkov, A. Liebsch, and P. M. Echenique. Role of occupied d bands in the dynamics of excited electrons and holes in Ag. Physical Review B, 68:9, 2003.

[76] F. García-Vidal, L. Martin-Moreno, T. W. Ebbesen, and L. Kuipers. Light passing through subwavelength apertures. Reviews of Modern Physics, 82:729–787, 2010.

[77] F. García-Vidal, E. Moreno, J. Porto, and L. Martín-Moreno. Transmission of Light through a Single Rectangular Hole. Physical Review Letters, 95:103901, 2005.

[78] J. A. Gerber, S. Berweger, B. T. O'Callahan, and M. B. Raschke. Phase-Resolved Surface Plasmon Interferometry of Graphene. Physical Review Letters, 113:055502, 2014.

[79] L. P. Ghislain and W. Webb. Scanning-force microscope based on an optical trap. Optics Letters, 18:1678–1680, 1993.

[80] H. Giessen and R. Vogelgesang. Glimpsing the weak magnetic field of light. Science, 326:529–30, 2009.

[81] F. J. Giessibl. Advances in atomic force microscopy. Reviews of Modern Physics, 75:949–983, 2003.

[82] C. Girard, A. Dereux, and O. Martin. Theoretical analysis of light-inductive forces in scanning probe microscopy. Physical Review B, 49:13872–13881, 1994.

[83] G. Giuliani and G. Vignale. Quantum theory of the electron liquid. Cambridge University Press, 2005.

[84] R. Gordon. Reflection of cylindrical surface waves. Optics Express, 17:18621–18629, 2009.

[85] A. Govyadinov, I. Amenabar, F. Huth, P. S. Carney, and R. Hillenbrand. Quantitative Measurement of Local Infrared Absorption and Dielectric Function with Tip-Enhanced Near-Field Microscopy. The Journal of Physical Chemistry Letters, 4:1526–1531, 2013.

[86] T. Grosjean, I. A. Ibrahim, M. A. Suarez, G. W. Burr, M. Mivelle, and D. Charraut. Full vectorial imaging of electromagnetic light at subwavelength scale. Optics Express, 18:5809–5824, 2010.

[87] T. Grosjean, M. Mivelle, F. Baida, G. W. Burr, and U. C. Fischer. Diabolo nanoantenna for enhancing and confining the magnetic optical field. Nano Letters, 11:1009–13, 2011.

[88] S. Grothe, S. Johnston, S. Chi, P. Dosanjh, S. Burke, and Y. Pennec. Quantifying Many-Body Effects by High-Resolution Fourier Transform Scanning Tunneling Spectroscopy. Physical Review Letters, 111:246804, 2013.

[89] P. G. Gucciardi, M. Colocci, M. Labardi, and M. Allegrini. Thermal-expansion effects in near-field optical microscopy fiber probes induced by laser light absorption. Applied Physics Letters, 75:3408, 1999.

[90] J. Güdde, M. Rohleder, T. Meier, S. W. Koch, and U. Höfer. Time-resolved investigation of coherently controlled electric currents at a metal surface. Science, 318:1287–91, 2007.

[91] H. Gugger, M. Jurich, J. D. Swalen, and A. J. Sievers. Reply to "Comment on 'Observation of an index-of-refraction-induced change in the Drude parameters of Ag Films' ". Physical Review B, 34:1322–1324, 1986.

[92] B. Gumhalter, P. Lazić, and N. Došlić. Excitonic precursor states in ultrafast pump-probe spectroscopies of surface bands. Physica Status Solidi (B), 247:1907–1919, 2010.

[93] H. J. Hagemann, W. Gudat, and C. Kunz. Optical constants from the far infrared to the x-ray region: Mg, Al, Cu, Ag, Au, Bi, C, and Al_2O_3. Journal of the Optical Society of America, 65:742, 1975.

[94] A. J. Hallock, P. L. Redmond, and L. E. Brus. Optical forces between metallic particles. Proceedings of the National Academy of Sciences of the United States of America, 102:1280–4, 2005.

[95] G. V. Hartland. Optical studies of dynamics in noble metal nanostructures. Chemical Reviews, 111:3858–87, 2011.

[96] S. Hasan, R. Filter, A. Ahmed, R. Vogelgesang, R. Gordon, C. Rockstuhl, and F. Lederer. Relating localized nanoparticle resonances to an associated antenna problem. Physical Review B, 84:195405, 2011.

[97] B. Hauer, A. Engelhardt, and T. Taubner. Quasi-analytical model for scattering infrared near-field microscopy on layered systems. Optics Express, 20:1387–1392, 2012.

[98] S. M. Hein and H. Giessen. Tailoring Magnetic Dipole Emission with Plasmonic Split-Ring Resonators. Physical Review Letters, 111:026803, 2013.

[99] M. Hentschel, T. Weiss, S. Bagheri, and H. Giessen. Babinet to the half: coupling of solid and inverse plasmonic structures. Nano Letters, 13:4428–33, 2013.

[100] T. Holstein. Theory of transport phenomena in an electron-phonon gas. Annals of Physics, 29:410–535, 1964.

[101] M. Hu, C. Novo, A. Funston, H. Wang, H. Staleva, S. Zou, P. Mulvaney, Y. Xia, and G. V. Hartland. Dark-field microscopy studies of single metal nanoparticles: understanding the factors that influence the linewidth of the localized surface plasmon resonance. Journal of Materials Chemistry, 18:1949–1960, 2008.

[102] F. Huang, V. Tamma, Z. Mardy, J. Burdett, and H. K. Wickramasinghe. Imaging Nanoscale Electromagnetic Near-Field Distributions Using Optical Forces. Scientific Reports, 5:10610, 2015.

[103] F. Huth, A. Govyadinov, S. Amarie, W. Nuansing, F. Keilmann, and R. Hillenbrand. Nano-FTIR absorption spectroscopy of molecular fingerprints at 20 nm spatial resolution. Nano Letters, 12:3973–8, 2012.

[104] T. Iida and H. Ishihara. Theoretical study of resonant-light-induced force microscopy. Nanotechnology, 18:084018, 2007.

[105] Y. Inouye and S. Kawata. Near-field scanning optical microscope with a metallic probe tip. Optics Letters, 19:159, 1994.

[106] J. D. Jackson. Classical Electrodynamics. Wiley; 3 edition, 1998.

[107] J. Jahng, J. Brocious, D. A. Fishman, F. Huang, X. Li, V. Tamma, H. K. Wickramasinghe, and E. Potma. Gradient and scattering forces in photoinduced force microscopy. Physical Review B, 90:155417, 2014.

[108] J. Jahng, J. Brocious, D. A. Fishman, S. Yampolsky, D. Nowak, F. Huang, V. A. Apkarian, H. K. Wickramasinghe, and E. Potma. Ultrafast pump-probe force microscopy with nanoscale resolution. Applied Physics Letters, 106:083113, 2015.

[109] Y. Jiang, S. Pillai, and M. Green. Re-evaluation of literature values of silver optical constants. Optics Express, 23:2133, 2015.

[110] J. Jin. The Finite Element Method in Electromagnetics. Wiley, 2002.

[111] O. Jitrik. Transition Probabilities for Hydrogen-Like Atoms. Journal of Physical and Chemical Reference Data, 33:1059, 2004.

[112] P. B. Johnson and R. W. Christy. Optical Constants of the Noble Metals. Physical Review B, 6:4370–4379, 1972.

[113] A. C. Jones, S. Berweger, J. Wei, D. Cobden, and M. B. Raschke. Nano-optical investigations of the metal-insulator phase behavior of individual VO_2 microcrystals. Nano Letters, 10:1574–81, 2010.

[114] K. Joulain, J. Mulet, F. Marquier, R. Carminati, and J. Greffet. Surface electromagnetic waves thermally excited: Radiative heat transfer, coherence properties and Casimir forces revisited in the near field. Surface Science Reports, 57:59–112, 2005.

[115] R. R. Joyce and P. L. Richards. Phonon contribution to the far-infrared absorptivity of superconducting and normal lead. Physical Review Letters, 24:1007–1011, 1970.

[116] V. Kabashin, P. Evans, S. Pastkovsky, W. Hendren, G. Wurtz, R. Atkinson, R. Pollard, V. A. Podolskiy, and V. Zayats. Plasmonic nanorod metamaterials for biosensing. Nature materials, 8:867–71, 2009.

[117] S. Karaveli and R. Zia. Spectral Tuning by Selective Enhancement of Electric and Magnetic Dipole Emission. Physical Review Letters, 106:193004, 2011.

[118] A. M. Katzenmeyer, J. Chae, R. Kasica, G. Holland, B. Lahiri, and A. Centrone. Nanoscale Imaging and Spectroscopy of Plasmonic Modes with the PTIR Technique. Advanced Optical Materials, 2:718–722, 2014.

[119] H. Kihm, S. Koo, Q. Kim, K. Bao, J. Kihm, W. Bak, S. Eah, C. Lienau, H. Kim, P. Nordlander, N. J. Halas, N. Park, and D. Kim. Bethe-hole polarization analyser for the magnetic vector of light. Nature communications, 2:451, 2011.

[120] H. Woo Kihm, J. Kim, S. Koo, J. Ahn, K. Ahn, K. Lee, N. Park, and D. Kim. Optical magnetic field mapping using a subwavelength aperture. Optics Express, 21:5625–33, 2013.

[121] S. Kirkpatrick, C. D. Gelatt, and M. P. Vecchi. Optimization by simulated annealing. Science, 220:671–80, 1983.

[122] T. A. Klar, S. Jakobs, M. Dyba, A. Egner, and S. W. Hell. Fluorescence microscopy with diffraction resolution barrier broken by stimulated emission. Proceedings of the National Academy of Sciences of the United States of America, 97:8206–8210, 2000.

[123] M. Klein, C. Enkrich, M. Wegener, and S. Linden. Second-harmonic generation from magnetic metamaterials. Science, 313:502–4, 2006.

[124] B. Knoll and F. Keilmann. Enhanced dielectric contrast in scattering-type scanning near-field optical microscopy. Optics Communications, 182:321–328, 2000.

[125] D. Kohlgraf-Owens, L. Greusard, S. Sukhov, Y. De Wilde, and A. Dogariu. Multi-frequency near-field scanning optical microscopy. Nanotechnology, 25:035203, 2014.

[126] J. Kohoutek, D. Dey, A. Bonakdar, R. Gelfand, A. Sklar, O. Gokalp Memis, and H. Mohseni. Opto-mechanical force mapping of deep subwavelength plasmonic modes. Nano Letters, 11:3378–82, 2011.

[127] M. Kominami, D. Pozar, and D. Schaubert. Dipole and slot elements and arrays on semi-infinite substrates. IEEE Transactions on Antennas and Propagation, 33:600–607, 1985.

[128] S. Koo, M. Kumar, J. Shin, D. Kim, and N. Park. Extraordinary Magnetic Field Enhancement with Metallic Nanowire: Role of Surface Impedance in Babinets Principle for Sub-Skin-Depth Regime. Physical Review Letters, 103:263901, 2009.

[129] E. E. Krasovskii, W. Schattke, L. Christoph, and P. Hrvoje. Electromagnetic Interactions with Solids. In Uwe Bovensiepen, Hrvoje Petek, Martin Wolf, editor, Dynamics at Solid State Surfaces and Interfaces: Volume 2: Fundamentals. Wiley-VCH Verlag GmbH, 2012.

[130] H. Kuzmany. Solid-State Spectroscopy. Springer, 2009.

[131] W. Lawrence. Electron-electron scattering in the low-temperature resistivity of the noble metals. Physical Review B, 13:5316–5319, 1976.

[132] W. E. Lawrence and J. W. Wilkins. Electron-electron scattering in the transport coefficients of simple metals. Physical Review B, 7:2317–2332, 1973.

[133] B. le Feber, N. Rotenberg, D. M. Beggs, and L. Kuipers. Simultaneous measurement of nanoscale electric and magnetic optical fields. Nature Photonics, 8:43–46, 2013.

[134] M. Lester, J. Arias-González, and M. Nieto-Vesperinas. Fundamentals and model of photonic-force microscopy. Optics Letters, 26:707–9, 2001.

[135] G. Leveque, C. Olson, and D. Lynch. Reflectance spectra and dielectric functions for Ag in the region of interband transitions. Physical Review B, 27:4654–4660, 1983.

[136] P. Lewis and P. Lee. Band Structure and Electronic Properties of Silver. Physical Review, 175:795–804, 1968.

[137] M. Li, W. Pernice, C. Xiong, T. Baehr-Jones, M. Hochberg, and H. Tang. Harnessing optical forces in integrated photonic circuits. Nature, 456:480–484, 2008.

[138] M. Lieb and A. Meixner. A high numerical aperture parabolic mirror as imaging device for confocal microscopy. Optics Express, 8:458–74, 2001.

[139] C. Lienau, A. Richter, and T. Elsaesser. Light-induced expansion of fiber tips in near-field scanning optical microscopy. Applied Physics Letters, 69:325, 1996.

[140] M. Liu, M. Pelton, and P. Guyot-Sionnest. Reduced damping of surface plasmons at low temperatures. Physical Review B, 79:035418, 2009.

[141] P. Lovhaugen. Optical Forces, Waveguides and Micro Raman Spectroscopy. PhD thesis, University of Tromso, 2012.

[142] F. Lu and M. A. Belkin. Infrared absorption nano-spectroscopy using sample photoexpansion induced by tunable quantum cascade lasers. Optics Express, 19:19942–7, 2011.

[143] F. Lu, M. Jin, and M. A. Belkin. Tip-enhanced infrared nanospectroscopy via molecular expansion force detection. Nature Photonics, 8:307–312, 2014.

[144] S. Lupi, L. Baldassarre, B. Mansart, A. Perucchi, A. Barinov, P. Dudin, E. Papalazarou, F. Rodolakis, J. P. Rueff, J. P. Itié, S. Ravy, D. Nicoletti, P. Postorino, P. Hansmann, N. Parragh, A. Toschi, T. Saha-Dasgupta, O. Andersen, G. Sangiovanni, K. Held, and M. Marsi. A Microscopic View on the Mott transition in Chromium-doped V_2O_3. Nature communications, 1:105, 2010.

[145] D. W. Lynch and W. R. Hunter. Comments on the optical constants of metals and an introduction to the data for several metals. In Edward D. Palik, editor, Handbook of Optical Constants of Solids, pages 275 – 367. Academic Press, Burlington, 1997.

[146] A. Marini and R. Del Sole. Dynamical excitonic effects in metals and semiconductors. Physical Review Letters, 91:176402, 2003.

[147] A. Marini, R. Del Sole, and G. Onida. First-principles calculation of the plasmon resonance and of the reflectance spectrum of silver in the GW approximation. Physical Review B, 66:115101, 2002.

[148] Y. Martin, C. C. Williams, and H. K. Wickramasinghe. Atomic force microscope force mapping and profiling on a sub 100-A scale. Journal of Applied Physics, 61:4723, 1987.

[149] Y. C. Martin, H. F. Hamann, and H. K. Wickramasinghe. Strength of the electric field in apertureless near-field optical microscopy. Journal of Applied Physics, 89:5774, 2001.

[150] S. Mastel, A. Govyadinov, T. Oliveira, I. Amenabar, and R. Hillenbrand. Nanoscale-resolved chemical identification of thin organic films using infrared near-field spectroscopy and standard Fourier transform infrared references. Applied Physics Letters, 106:023113, 2015.

[151] R. A. Matula. Electrical resistivity of copper, gold, palladium, and silver. Journal of Physical and Chemical Reference Data, 8:1147, 1979.

[152] A. S. McLeod, P. Kelly, M. D. Goldflam, Z. Gainsforth, A. J. Westphal, G. Dominguez, M. H. Thiemens, M. M. Fogler, and D. N. Basov. Model for quantitative tip-enhanced spectroscopy and the extraction of nanoscale-resolved optical constants. Physical Review B, 90:085136, 2014.

[153] D. McWhan, A. Jayaraman, J. Remeika, and T. Rice. Metal-Insulator Transition in $(V_{1-x}Cr_x)_2O_3$. Physical Review Letters, 34:547–550, 1975.

[154] A. O. Melikyan and B. V. Kryzhanovsky. Modeling of the optical properties of silver with use of six fitting parameters. Optical Memory and Neural Networks, 23(1):1–5, March 2014.

[155] J. Mertz, M. Hipp, J. Mlynek, and O. Marti. Optical near-field imaging with a semiconductor probe tip. Applied Physics Letters, 64:2338–2340, 1994.

[156] V. D. Miljković, T. Pakizeh, B. Sepulveda, P. Johansson, and M. Käll. Optical forces in plasmonic nanoparticle dimers. Journal of Physical Chemistry C, 114:7472–7479, 2010.

[157] F. Mor, A. Sienkiewicz, L. Forró, and S. Jeney. Upconversion Particle as a Local Luminescent Brownian Probe: A Photonic Force Microscopy Study. ACS Photonics, 1:1251–1257, 2014.

[158] S. Mousavi, P. T. Rakich, and Z. Wang. Strong THz and Infrared Optical Forces on a Suspended Single-Layer Graphene Sheet. ACS Photonics, 1:1107–1115, 2014.

[159] R. Muiño, D. Sánchez-Portal, V. Silkin, E. Chulkov, and P. Echenique. Surface chemistry special feature: Time-dependent electron phenomena at surfaces. Proceedings of the National Academy of Sciences, 108:971–976, 2011.

[160] E. A. Muller, B. Pollard, and M. B. Raschke. Infrared Chemical Nano-Imaging: Accessing Structure, Coupling, and Dynamics on Molecular Length Scales. The Journal of Physical Chemistry Letters, 6:1275–1284, 2015.

[161] K. Munechika, J.M. Smith, Y. Chen, and D.S. Ginger. Plasmon Line Widths of Single Silver Nanoprisms as a Function of Particle Size and Plasmon Peak Position. Journal of Physical Chemistry C, 111:18906–18911, 2007.

[162] P. Nagpal, N. C. Lindquist, S. Oh, and D. J. Norris. Ultrasmooth patterned metals for plasmonics and metamaterials. Science, 325:594–7, 2009.

[163] D. J. Nash and J. R. Sambles. Surface plasmon-polariton study of the optical dielectric function of silver. Journal of Modern Optics, 43:81–91, 1996.

[164] C. C. Neacsu, G. A. Steudle, and M. B. Raschke. Plasmonic light scattering from nanoscopic metal tips. Applied Physics B, 80:295–300, 2005.

[165] F. Neubrech, T. Kolb, R. Lovrincic, G. Fahsold, A. Pucci, J. Aizpurua, T. W. Cornelius, M. E. Toimil-Molares, R. Neumann, and S. Karim. Resonances of individual metal nanowires in the infrared. Applied Physics Letters, 89:253104, 2006.

[166] J. Ng, R. Tang, and C. T. Chan. Electrodynamics study of plasmonic bonding and antibonding forces in a bisphere. Physical Review B, 77:195407, 2008.

[167] M. Nieto-Vesperinas and J. Arias-Gonzalez. Theory of Forces Induced by Evanescent Fields. arXiv:1102.1613, 2011.

[168] M. Nieto-Vesperinas, P. C Chaumet, and A. Rahmani. Near-field photonic forces. Philosophical transactions. Series A, 362:719–737, 2004.

[169] Nobel Prize Committee. Super-resolved fluorescence microscopy. The Nobel Prize in Chemistry 2014, 2014.

[170] M. Nonnenmacher and H. K. Wickramasinghe. Optical absorption spectroscopy by scanning force microscopy. Ultramicroscopy, 42:351, 1992.

[171] L. Novotny. Effective Wavelength Scaling for Optical Antennas. Physical Review Letters, 98:266802, 2007.

[172] L. Novotny. The History of Near-field Optics. In E Wolf, editor, Progress in Optics 50, chapter 5, pages 137– 184. Elsevier, Amsterdam, The Netherlands, 2007.

[173] L. Novotny. From near-field optics to optical antennas. Physics Today, July:47–52, 2011.

[174] T. Oates, H. Wormeester, and H. Arwin. Characterization of plasmonic effects in thin films and metamaterials using spectroscopic ellipsometry. Progress in Surface Science, 86:328–376, 2011.

[175] N. Ocelic, A. Huber, and R. Hillenbrand. Pseudoheterodyne detection for background-free near-field spectroscopy. Applied Physics Letters, 89:101124, 2006.

[176] B. Ögüt, R. Vogelgesang, W. Sigle, N. Talebi, C. Koch, and P. van Aken. Hybridized metal slit eigenmodes as an illustration of Babinet's principle. ACS nano, 5:6701–6, 2011.

[177] R. L. Olmon, P. M. Krenz, A. C. Jones, G. D. Boreman, and M. B. Raschke. Near-field imaging of optical antenna modes in the mid-infrared. Optics Express, 16(25):20295–305, December 2008.

[178] R. L. Olmon, M. Rang, P. M. Krenz, B. A. Lail, L. V. Saraf, G. D. Boreman, and M. B. Raschke. Determination of Electric-Field, Magnetic-Field, and Electric-Current Distributions of Infrared Optical Antennas: A Near-Field Optical Vector Network Analyzer. Physical Review Letters, 105:167403, 2010.

[179] R. L. Olmon and M. B. Raschke. Antenna-load interactions at optical frequencies: impedance matching to quantum systems. Nanotechnology, 23:444001, 2012.

[180] R. L. Olmon, B. Slovick, T. W. Johnson, D. Shelton, S. Oh, G. D. Boreman, and M. B. Raschke. Optical dielectric function of gold. Physical Review B, 86:235147, 2012.

[181] M. Ordal, L. Long, R. Bell, S. Bell, R. Bell, R. Alexander, and C. Ward. Optical properties of the metals Al, Co, Cu, Au, Fe, Pb, Ni, Pd, Pt, Ag, Ti, and W in the infrared and far infrared. Applied Optics, 22:1099–20, 1983.

[182] G. Panaccione, G. Cautero, M. Cautero, A. Fondacaro, M. Grioni, P. Lacovig, G. Monaco, F. Offi, G. Paolicelli, M. Sacchi, N. Stojić, G. Stefani, R. Tommasini, and P. Torelli. High-energy photoemission in silver: resolving d and sp contributions in valence band spectra. Journal of Physics: Condensed Matter, 17:2671–2679, 2005.

[183] J. Park, P. Ambwani, M. Manno, N. C Lindquist, P. Nagpal, S. Oh, C. Leighton, and D. J. Norris. Single-crystalline silver films for plasmonics. Advanced Materials, 24:3988–92, 2012.

[184] J. Park, P. Nagpal, S. Oh, and D. J. Norris. Improved dielectric functions in metallic films obtained via template stripping. Applied Physics Letters, 100:081105, 2012.

[185] G. Parkins, W. Lawrence, and R. Christy. Intraband optical conductivity $\sigma(\omega,T)$ of Cu, Ag, and Au: Contribution from electron-electron scattering. Physical Review B, 23:6408–6416, 1981.

[186] F. Pawlek and D. Rogalla. The electrical resistivity of silver, copper, aluminium, and zinc as a function of purity in the range 4298 K. Cryogenics, 6:14–20, 1966.

[187] M. Pelton, M. Liu, H. Kim, G. Smith, P. Guyot-Sionnest, and N. Scherer. Optical trapping and alignment of single gold nanorods by using plasmon resonances. Optics Letters, 31(13):2075–7, July 2006.

[188] J. B. Pendry, A. J. Holden, D. J. Robbins, and W. J. Stewart. Magnetism from conductors and enhanced nonlinear phenomena. IEEE Transactions on Microwave Theory and Techniques, 47:2075–2084, 1999.

[189] D. W. Pohl, W. Denk, and M. Lanz. Optical stethoscopy: Image recording with resolution $\lambda/20$. Applied Physics Letters, 44:651, 1984.

[190] M. Quinten. Optical constants of gold and silver clusters in the spectral range between 1.5 eV and 4.5 eV. Zeitschrift für Physik B Condensed Matter, 101:211–217, 1996.

[191] I. Rajapaksa, K. Uenal, and H. K. Wickramasinghe. Image force microscopy of molecular resonance: A microscope principle. Applied Physics Letters, 97:2010–2012, 2010.

[192] I. Rajapaksa and H. K. Wickramasinghe. Raman spectroscopy and microscopy based on mechanical force detection. Applied Physics Letters, 99:161103–1611033, 2011.

[193] A. D. Rakic, A. B. Djurisic, J. M. Elazar, and M. L. Majewski. Optical properties of metallic films for vertical-cavity optoelectronic devices. Applied Optics, 37:5271–83, 1998.

[194] M. B. Raschke, S. Berweger, and J. M. Atkin. Plasmonics: Theory and Applications. Springer, 2013.

[195] M. B. Raschke and C. Lienau. Apertureless near-field optical microscopy: Tipsample coupling in elastic light scattering. Applied Physics Letters, 83:5089, 2003.

[196] D. J. Roaf. The Fermi Surfaces of Copper, Silver and Gold II. Calculation of the Fermi Surfaces. Philosophical Transactions for the Royal Society of London. Series A, 255:135–152, 1962.

[197] C. Rockstuhl, T. Zentgraf, T. Meyrath, H. Giessen, and F. Lederer. Resonances in complementary metamaterials and nanoapertures. Optics Express, 16:2080–90, 2008.

[198] I. Romero, J. Aizpurua, G. Bryant, and F. J. García De Abajo. Plasmons in nearly touching metallic nanoparticles: singular response in the limit of touching dimers. Optics Express, 14:9988–9999, 2006.

[199] D. Rugar, H. J. Mamin, and P. Guethner. Improved fiber-optic interferometer for atomic force microscopy. Applied Physics Letters, 55:2588, 1989.

[200] H. Scher. Far-infrared absorptivity of normal lead. Physical Review Letters, 25:759–763, 1970.

[201] G. Schider, J. Krenn, A. Hohenau, H. Ditlbacher, A. Leitner, F. Aussenegg, W. Schaich, I. Puscasu, B. Monacelli, and G. Boreman. Plasmon dispersion relation of Au and Ag nanowires. Physical Review B, 68:155427, 2003.

[202] M. Schnell, P. S. Carney, and R. Hillenbrand. Synthetic optical holography for rapid nanoimaging. Nature communications, 5:3499, 2014.

[203] M. Schnell, A. Garcia-Etxarri, J. Alkorta, J. Aizpurua, and R. Hillenbrand. Phase-resolved mapping of the near-field vector and polarization state in nanoscale antenna gaps. Nano Letters, 10:3524–8, 2010.

[204] L. G. Schulz. An Interferometric Method for the Determination of the Absorption Coefficients of Metals, with Results for Silver and Alutminum. Journal of the Optical Society of America, 41:1047, 1951.

[205] L. G. Schulz. An Experimental Confirmation of the Drude Free Electron Theory of the Optical Properties of Metals for Silver, Gold, and Copper in the Near Infrared. Journal of the Optical Society of America, 44(7):540, July 1954.

[206] L. G. Schulz and F. R. Tangherlini. Optical Constants of Silver, Gold, Copper, and Aluminum II The Index of Refraction n. Journal of the Optical Society of America, 44:362, 1954.

[207] M. Seo, A. Adam, J. Kang, J. Lee, S. Jeoung, Q. Park, P. Planken, and D. Kim. Fourier-transform terahertz near-field imaging of one-dimensional slit arrays: mapping of electric-field-, magnetic-field-, and Poynting vectors. Optics Express, 15:11781–11789, 2007.

[208] N. Smith. Classical generalization of the Drude formula for the optical conductivity. Physical Review B, 64(15):155106, September 2001.

[209] T. Søndergaard, J. Beermann, A. Boltasseva, and S. I. Bozhevolnyi. Slow-plasmon resonant-nanostrip antennas: Analysis and demonstration. Physical Review B, 77:115420, 2008.

[210] C. Sönnichsen, T. Franzl, T. Wilk, G. von Plessen, and J. Feldmann. Plasmon resonances in large noble-metal clusters. New Journal of Physics, 4:93–93, 2002.

[211] M. Specht, J. Pedarnig, W. Heckl, and T. Hänsch. Scanning plasmon near-field microscope. Physical Review Letters, 68:476–479, 1992.

[212] K. Stahrenberg, T. Herrmann, K. Wilmers, N. Esser, W. Richter, and M. Lee. Optical properties of copper and silver in the energy range 2.59.0 eV. Physical Review B, 64:115111, 2001.

[213] A. L. Stout and W. W. Webb. Chapter 6 Optical Force Microscopy. In Methods in cell biology, pages 99–116. 1997.

[214] E. Taft and H. Philipp. Optical Constants of Silver. Physical Review, 121:1100–1103, 1961.

[215] D. Tanner and D. Larson. Electrical Resistivity of Silver Films. Physical Review, 166:652–655, 1968.

[216] M. Thèye. Investigation of the Optical Properties of Au by Means of Thin Semitransparent Films. Physical Review B, 2:3060–3078, 1970.

[217] S. Thomas, G. Wachter, C. Lemell, J. Burgdörfer, and P. Hommelhoff. Large optical field enhancement for nanotips with large opening angles. New Journal of Physics, 17:063010, 2015.

[218] H. G. Tompkins and E. A. Irene. Handbook of ellipsometry. Springer, 2005.

[219] J. Trollmann and A. Pucci. Infrared Dielectric Function of Gold Films in Relation to Their Morphology. The Journal of Physical Chemistry C, 118:15011–15018, 2014.

[220] M. Vilfan, I. Muševič, and M. Čopič. AFM observation of force on a dielectric sphere in the evanescent field of totally reflected light. Europhysics Letters (EPL), 43:41–46, 1998.

[221] G. Volpe, R. Quidant, G. Badenes, and D. Petrov. Surface Plasmon Radiation Forces. Physical Review Letters, 96:238101, 2006.

[222] K. Wang and D. Mittleman. Dispersion of Surface Plasmon Polaritons on Metal Wires in the Terahertz Frequency Range. Physical Review Letters, 96:157401, 2006.

[223] J. Weaver. Optical properties of metals (Physik Daten). Fachinformationszentrum Energie, Physik, Mathematik, 1981.

[224] E. Weiss, G. Kaufman, J. Kriebel, Z. Li, R. Schalek, and G. Whitesides. Si/SiO_2-templated formation of ultraflat metal surfaces on glass, polymer, and solder supports: their use as substrates for self-assembled monolayers. Langmuir : the ACS journal of surfaces and colloids, 23:9686–94, 2007.

[225] P. Winsemius, F. van Kampen, H. Lengkeek, and C. van Went. Temperature dependence of the optical properties of Au, Ag and Cu. Journal of Physics F: Metal Physics, 6:1583–1606, 1976.

[226] Y. Wu, C. Zhang, N. Estakhri, Y. Zhao, J. Kim, M. Zhang, X. Liu, G. K. Pribil, A. Alù, C. Shih, and X. Li. Intrinsic optical properties and enhanced plasmonic response of epitaxial silver. Advanced Materials, 26:6106–6110, 2014.

[227] H. Xu and M. Käll. Surface-Plasmon-Enhanced Optical Forces in Silver Nanoaggregates. Physical Review Letters, 89:246802, 2002.

[228] A. Yang and D. Erickson. Stability analysis of optofluidic transport on solid-core waveguiding structures. Nanotechnology, 19:045704, 2008.

[229] S. J. Youn, T. H. Rho, B. I. Min, and K. S. Kim. Extended Drude model analysis of noble metals. Physica Status Solidi (B), 244:1354–1362, 2007.

[230] F. Zenhausern, M. Boyle, and H. K. Wickramasinghe. Apertureless near-field optical microscope. Applied Physics Letters, 65:1623, 1994.

[231] F. Zenhausern, Y. Martin, and H. K. Wickramasinghe. Scanning interferometric apertureless microscopy: optical imaging at 10 angstrom resolution. Science, 269:1083–1085, 1995.

[232] T. Zentgraf, T. Meyrath, A. Seidel, S. Kaiser, H. Giessen, C. Rockstuhl, and F. Lederer. Babinet's principle for optical frequency metamaterials and nanoantennas. Physical Review B, 76:033407, 2007.

[233] J. Zhang, K. F. MacDonald, and N. Zheludev. Optical gecko toe: Optically controlled attractive near-field forces between plasmonic metamaterials and dielectric or metal surfaces. Physical Review B, 85:1–5, 2012.

[234] L. Zhang, G. Andreev, Z. Fei, A. S. McLeod, G. Dominguez, M. Thiemens, A. Castro-Neto, D. Basov, and M. Fogler. Near-field spectroscopy of silicon dioxide thin films. Physical Review B, 85:1–8, 2012.

[235] L. Zhang, A. Kubo, L. Wang, H. Petek, and T. Seideman. Imaging of surface plasmon polariton fields excited at a nanometer-scale slit. Physical Review B, 84:245442, 2011.

[236] X. Zhu, G. Huang, H. Zhou, X. Yang, Z. Wang, Y. Ling, Y. Dai, and Z. Gan. Ultrasonic resonance regulated near-field scanning optical microscope and laser induced near-field optical-force interaction. Optical Review, 4:A236–A239, 1997.

Appendix A

Finite Element Method

The finite element method is a widely used numerical technique to solve complicated boundary-value problems with approximation [110]. The boundary-value problems in a domain Ω with boundary condition Γ can be written in a general form:

$$\mathcal{L}\psi = f, \tag{A.1}$$

where $\mathcal{L}$ is a differential operator, f is a given function and ψ is the unknown function to be found. In electromagnetics most practical problems do not have analytical solutions, and therefore require approximation methods. To illustrate the ideas of the finite element technique, we need to start from two general approximation methods: The Ritz and Galerkin's methods. The Ritz method is a variational method to find the approximate solution by minimizing an associated functional:

$$F(\tilde{\psi}) = \frac{1}{2}\langle \mathcal{L}\tilde{\psi}, \tilde{\psi}\rangle - \frac{1}{2}\langle \tilde{\psi}, f\rangle - \frac{1}{2}\langle f, \tilde{\psi}\rangle, \tag{A.2}$$

with respect to $\tilde{\psi}$, where $\tilde{\psi}$ is the trial function, the angular brackets denote inner products:

$$\langle \psi, \phi\rangle = \int_{\Omega} \psi\phi^* d\Omega, \tag{A.3}$$

and the operator $\mathcal{L}$ is self-adjoint and positive definite. The Galerkin's method is a weighted residual method that obtains approximation solutions by minimizing the weighted residual of the differential equation $r = \mathcal{L}\tilde{\psi} - f$ at all points of Ω, which also means minimizing the total residual over the domain Ω:

$$R = \int_{\Omega} \omega \cdot r d\Omega \tag{A.4}$$

where ω is the weighted function.

The two classical methods both require a trial function $\tilde{\psi}$ defined over the whole domain that could at least approximately represent the true solution. In complicated electromagnetic systems, especially in two or three dimensions with irregular boundary conditions, it is very difficult, if not impossible, to find such an entire-domain trial function. This is where the finite element method steps in: If the whole domain is decomposed into a number of subdomains (which is also called 'element'), and the trial function becomes a combination of local unknown functions defined over subdomains, then on each small subdomain the local unknown function could have quite simple forms. In other words, the entire-domain unknown function ψ is approximated by a finite number of simple interpolation functions over subdomains. Then the unknown coefficients of the interpolations functions can be found by applying the Ritz or Galerkin's methods.

In brief words the finite element methods have four steps:

(1) Domain discretization. In the commercial FEM software COMSOL that is used in this thesis, this step is also called 'Meshing'. The shape of the elements are usually line segments for one-dimensional domain, triangles or rectangles for two-dimensional domain, and tetrahedra, triangle prisms or rectangle bricks for three-dimensional domain. The element's size could also vary depending on the gradient of the fields, i.e., smaller in the region where the fields vary fast and larger elsewhere. The discretization manner could affect the performance in terms of storage space, computation efficiency and accuracy.

(2) Selection of interpolation functions. The interpolation function should be selected to approximate the solution within an element. It usually comes in a polynomial form with various orders. For element e

$$\tilde{\psi}^e = \sum_{j=1}^{n} N_j^e \psi_j^e, \tag{A.5}$$

where the sum runs over the nodes in element e, ψ_j^e is the value of the unknown function ψ at node j and N_j^e is the interpolation function for node j. The choice of the polynomial order depends the trading off between efficiency (low order) and accuracy (high order).

The linear form is widely used due to its simplicity.

(3) Formulation of equations. After the domain is discretized and interpolation function is selected, we can formulate the system of equations either with Ritz or Galerkin's method. Since the COMSOL software uses Galerkin's method, here we will only briefly describe the procedure via Galerkin's method. The weighted residual for element e can be obtained by substituting Eq. A.5 into Eq. A.4:

$$R_i^e = \int_{\Omega^e} N_i^e \mathcal{L}\{\mathbf{N}^e\} d\Omega \{\psi^e\} - \int_{\Omega^e} f N_i^e d\Omega, \tag{A.6}$$

where $i = 1, ..., n$ and n is the number of nodes in element e. The above equation can be rewritten in matrix form as

$$\mathbf{R}^e = \mathbf{K}^e \psi^e - \mathbf{b}^e, \tag{A.7}$$

where

$$\mathbf{R}^e = [R_1^e, R_2^e, ..., R_n^e]^T, \tag{A.8}$$

$$K_{ij}^e = \int_{\Omega^e} N_i^e \mathcal{L} N_j^e d\Omega, \tag{A.9}$$

$$b_i^e = \int_{\Omega^e} f N_i^e d\Omega. \tag{A.10}$$

(4) Solution of equations. The final step is to solve the systems of equations of the general form:

$$\mathbf{K}\psi = \mathbf{b}. \tag{A.11}$$

The non-vanishing $\mathbf{b}$ corresponds to the existence of a source or excitation, while a vanishing $\mathbf{b}$ corresponds to source-free problems. After solving the system of equations, parameters of interests can be computed easily.

Appendix B

The optical dielectric function of silver: supplement

In this work three template stripped (TS) silver samples are measured with spectroscopic ellipsometry. The resulting dielectric data are corrected for Kramers-Kronig consistency and are shown in the main text. The dielectric data of silver before correction for Kramers-Kronig consistency are directly inverted from the ellipsometry measurements, and retain the instrumental errors. Here, we show the dielectric data of silver both before and after the correction. For consistency check with our previous work [180] and for comparison with silver, we also measured the dielectric function of three TS gold samples as described in the main text. A comparison with gold shows a larger variation of the dielectric function among silver samples possibly due to oxidation. Finally, we show measurements of the dielectric function of silver over a period of time. A trend of sample degrading is observed with a decreasing relaxation time τ.

B.1 Ellipsometry data of silver before and after correction

Fig. B.1 shows the direct inverted dielectric data from ellipsometry measurements and the Kramers-Kronig consistent fit with good agreement. Photon energy in linear scale (a), and in logarithmic scale (b) are plotted to emphasize the Vis/UV and IR spectral range, respectively. Due to residual instrumental errors the direct inverted dielectric data are not perfectly Kramers-Kronig consistent. We therefore fit the dielectric data of silver with an analytic formula consisting a Drude and three Gaussian functions, a procedure commonly used for metals [193, 154].

As noted in the main text, the deviation of the direct inverted dielectric function ϵ_2 from the

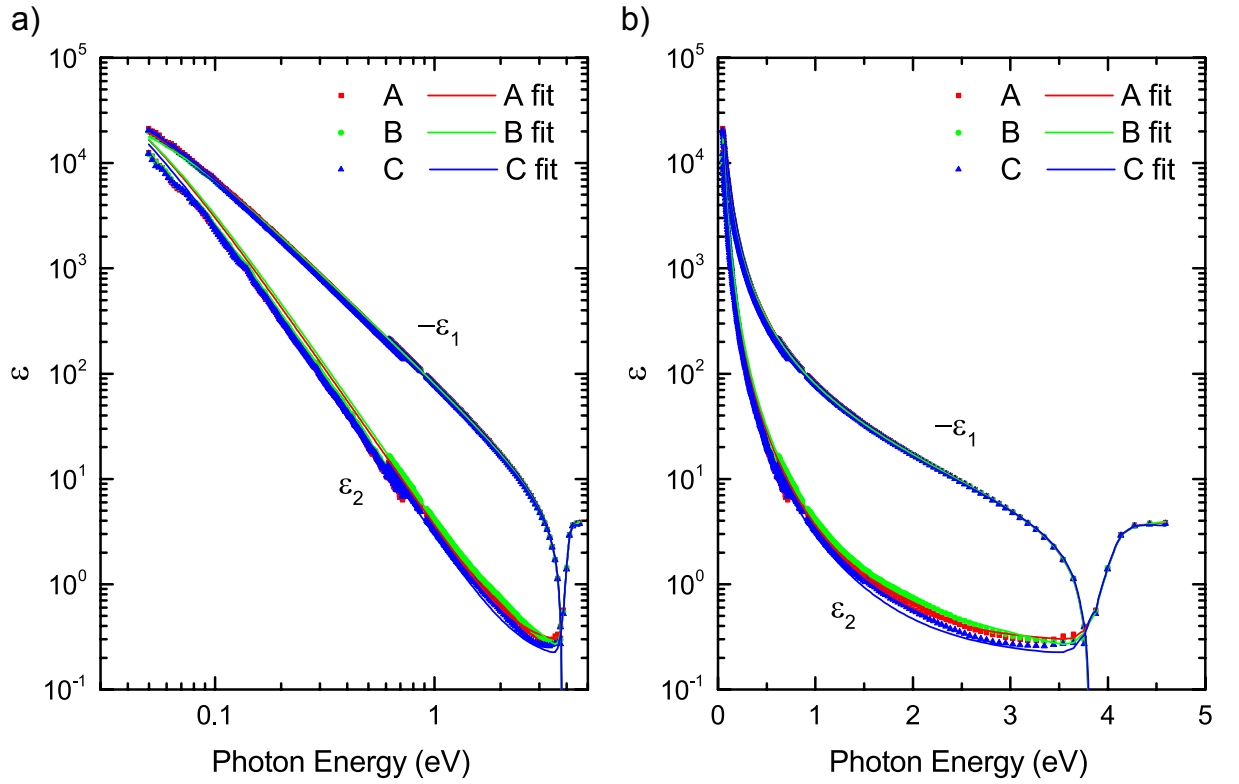

Figure B.1: Dielectric function of silver from direct inverted ellipsometry measurement (dot), and a Kramers-Kronig consistent fit (line). The three samples are shown in red, green, and blue. Photon energy in linear scale (a), and in logarithmic scale (b) are plotted to emphasize the Vis/UV and IR spectral range, respectively.

Drude fit at energies below 0.1 eV is the cause of a frequency dependent $\tau(\omega)$.

B.2 Dielectric function of gold

Fig. B.2 shows the direct inverted dielectric data of TS gold measured in this work in comparison with fitted dielectric function presented in our previous paper [180]. The relative differences in measured dielectric data between the three TS gold samples are less than the differences between the three TS silver samples.

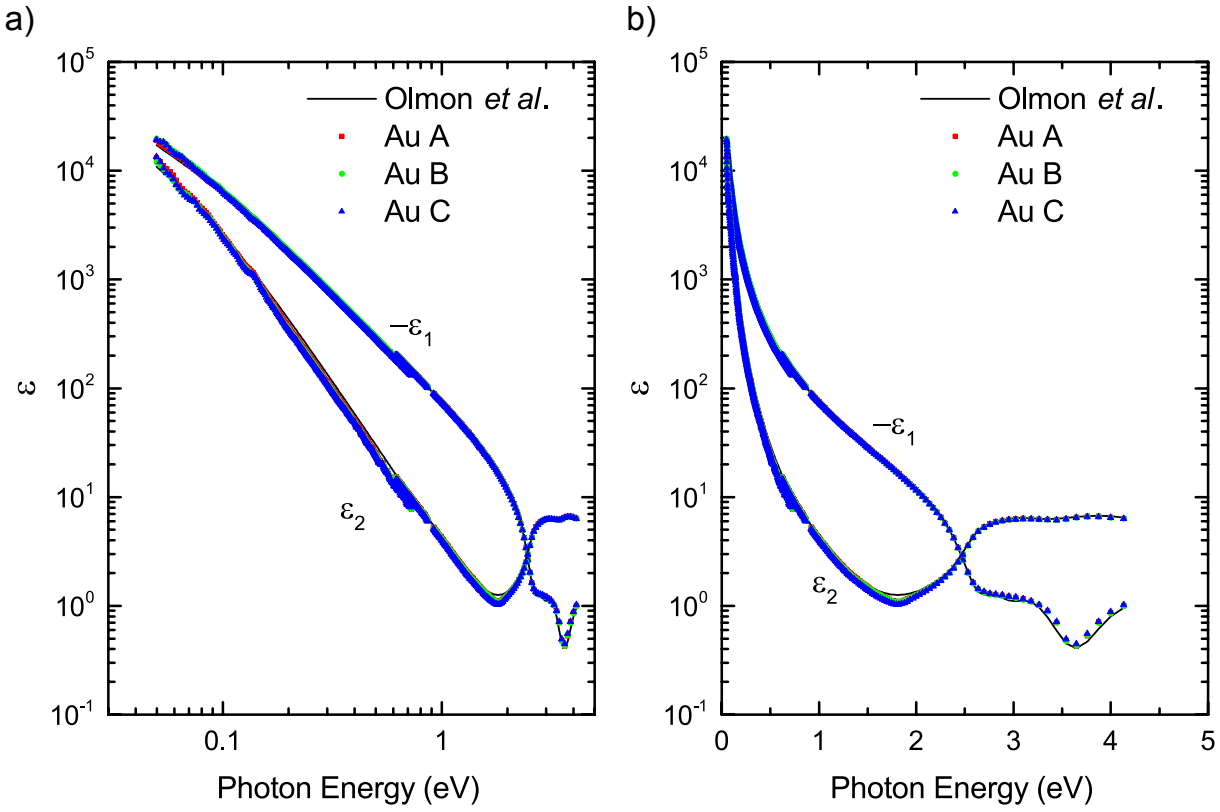

Figure B.2: Dielectric function of three TS gold samples from direct inverted ellipsometry measurement (red, green, and blue), in comparison with the fitted dielectric function presented in our previous paper (black) [180]. Plots with phonon energy in linear (a) and in logarithmic scale (b).

B.3 Instrument error vs sample difference

As shown in Fig. B.1 and B.2, in the overlapped spectral range of the two instruments of 0.62 – 0.73 eV (1.7 – 2 μm), the measured dielectric functions between the two instruments have an offset. This offset is fundamentally limited by the instruments, and is likely due to different light sources, difference in illumination spot sizes, and signal detection methods. The offset imposes an systematic error on our data. As the difference between the dielectric function of the three samples is less than this offset, we can conclude our data is dominated by the instrumental error.

B.4 Sample degrading over time

Comparing the measurements to gold, we see larger variations from sample to sample in silver. Existence of large variations even among nominally identical samples indicates silver is very sensitive to environmental conditions, such as surface oxidation, impurity, and crystallite size. These variations also affect the electron relaxation time τ.

To test the influence of surface oxidation, we measured the three samples a day later for comparison. Fig. B.3 shows the comparison of dielectric function for fresh samples (line) and the same samples one day later (dot). ϵ_1 of three samples only vary slightly. However, ϵ_2 of samples measured one day later are consistently smaller than fresh samples, indicating sample degrading. As the relaxation time τ can serve as a characteristic parameter for sample quality, we apply extended Drude model analysis to extract $\tau(\omega)$. The resulting $\tau(\omega)$ is shown in Fig. B.4, with decreased relaxation time τ after one day for the same samples. We also measured the same samples after 3 days and 7 days, but these results do not have a consistent trend for τ. This could be due to oxidation/contamination of the samples in an uncontrolled fashion over time when stored in ambient conditions.

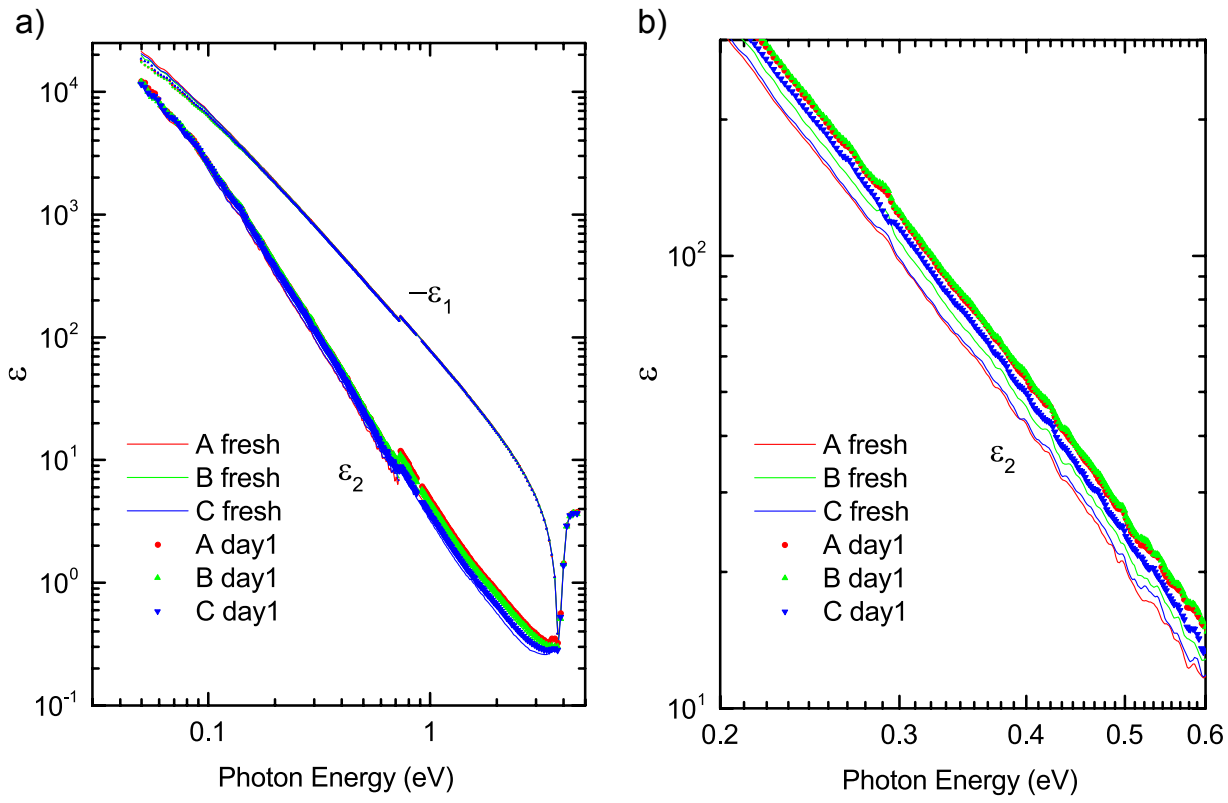

Figure B.3: (a) $-\epsilon_1$ and ϵ_2 for fresh silver samples (line) and one day later (dot) of sample A – C in red, green, and blue. (b) Zoom-in of ϵ_2 in (a) to show the increase in ϵ_2 of samples measured one day later compared to fresh samples. ϵ_2 of samples measured one day later are consistently larger than fresh samples, indicating sample degrading. ϵ_1 only vary slightly.

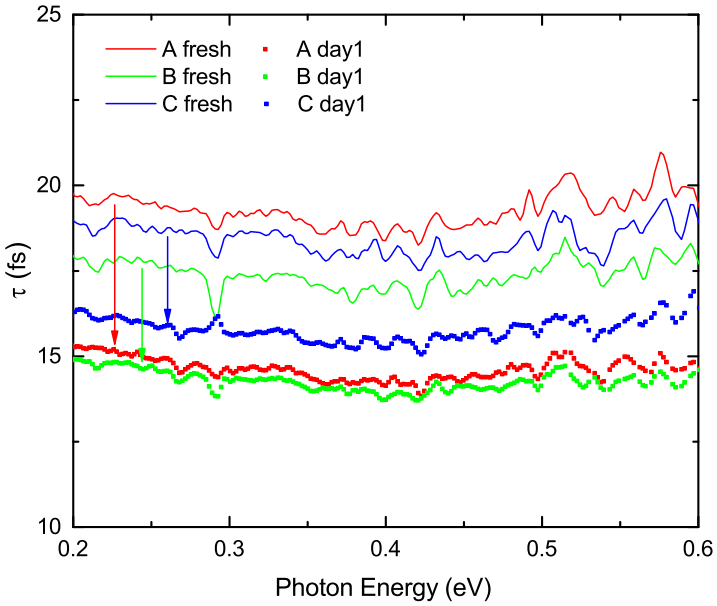

Figure B.4: Extracted relaxation time τ from extended Drude analysis. Fresh samples have a larger $\tau(\omega)$ compared to samples measured one day later, indicating sample degrading over time.

Appendix C

List of publications for PhD work

(1) **H. Yang**, E. Hebestreit, E. Josberger, and M.B. Raschke, "A cryogenic scattering-type scanning near-field optical microscope", Rev. Sci. Instruments 84, 023701 (2013)

(2) **H. Yang**, R. Olmon, K. Deryckx, X. Xu, H. Bechtel, Y. Xu, B. Lail, and M.B. Raschke, "Accessing the optical magnetic near-field through Babinet's principle", ACS Photonics 1, 894 (2014)

(3) **H. Yang**, J. Archangel, M. Sundheimer, E. Tucker, G. Boreman, and M.B. Raschke, "Optical dielectric function of silver", Physical Review B 91, 235137 (2015)

(4) A.C. Jones, B. O'Callahan, **H. Yang**, M.B. Raschke, "The thermal near-field: Coherence, spectroscopy, heat-transfer, and optical forces", Progress in Surface Science 88, 349 (2013)

(5) K. Kjoller, C. Marcott, C. Prater, **H. Yang**, M. Belkin, F. Lu, M. Jin, "Resonance-enhanced nanoscale IR spectroscopy of ultrathin films and monolayers on metals", FTIR Technology for Todays Spectroscopists 29, 18 (2014)

(6) **H. Yang**, S. Berweger, K. Kjoller, C. Prater, "Method and Apparatus for Infrared Scattering Scanning Near-Field Optical Microscopy with High Speed Point Spectroscopy", patent pending

(7) **H. Yang**, M.B. Raschke, "Resonant optical gradient force nano-imaging and -spectroscopy", Submitted.